

Electronic Thesis and Dissertation Repository

7-25-2016 12:00 AM

OMCVD Gold Nanoparticles Covalently Attached to Polystyrene for Biosensing Applications

Sivayini Kandeepan
The University of Western Ontario

Supervisor
Prof. Silvia Mittler
The University of Western Ontario

Graduate Program in Physics
A thesis submitted in partial fulfillment of the requirements for the degree in Master of Science
© Sivayini Kandeepan 2016

Follow this and additional works at: <https://ir.lib.uwo.ca/etd>

 Part of the [Condensed Matter Physics Commons](#)

Recommended Citation

Kandeepan, Sivayini, "OMCVD Gold Nanoparticles Covalently Attached to Polystyrene for Biosensing Applications" (2016). *Electronic Thesis and Dissertation Repository*. 4032.
<https://ir.lib.uwo.ca/etd/4032>

This Dissertation/Thesis is brought to you for free and open access by Scholarship@Western. It has been accepted for inclusion in Electronic Thesis and Dissertation Repository by an authorized administrator of Scholarship@Western. For more information, please contact wlsadmin@uwo.ca.

Abstract

Remarkable developments and successes were witnessed in the fabrication and implementation of optical sensors based on localized surface plasmon resonance (LSPR) for the investigation of chemical and biological material quantities and to detect lethal diseases such as cancer in early stages. Gold nanoparticles (AuNPs) are ideal candidate for sensing purposes due to their chemical stability, ease of surface functionalization and strong LSPR in the visible range. Although there are several designs of sensors published, most of them are still limited to small scale research laboratory use partly due to their high cost of fabrication and waste management, in particular critical for solution based LSPR sensors. Sensors implementing immobilized AuNPs show decreased impact in waste management as they are strongly attached to the surface by covalent bonding. In addition, sensors made from polymers are less expensive, mass producible and easier to handle in comparison to brittle glass sensors. We report on the reproducible fabrication of chemically stable surface immobilized AuNPs grown via organometallic chemical vapor deposition (OMCVD) on polystyrene (PS). Oxygen plasma and UV ozone treated PS samples produce enhanced amounts of polar -OH groups allowing for nucleation and growth of AuNPs. The optimum plasma treatment conditions, the largest shifts in the LSPR curves and the bulk sensitivity of the OMCVD grown AuNPs are discussed. It was found that the bio-sensing limit of detection of the grown AuNPs for streptavidin binding to biotin was ~ 10 ng/ml. In order to make this sensor applicable for clinical purposes, the sensitivity needs to be enhanced by building a polymer channel waveguide carrying AuNPs and increasing the interaction between the sample and the probing beam in future.

Keywords: OMCVD, AuNPs, plasmonics, polymer substrates, sensing

Acknowledgements

I would like to express my greatest gratitude to my supervisor Prof. Silvia Mittler for her continuous guidance and tireless explanation throughout the project. I am indebted to her for helping me in defining the problem, providing insights to the solution and ultimately guiding me to make my research a success.

My gratitude also goes to my advisory committee members, Prof. Lyudmila Goncharova and Prof. Mahi Singh for spending their time to evaluate my work and provide thoughtful discussions.

Also I wish to thank Joseph A. Paquette for synthesizing the gold precursor and his supervisor Prof. Joe Gilroy for his support. I am really thankful to Dr. Erden Ertorer for training me on the OMCVD process to start my project and for always being available to provide advice, besides his busy schedule.

I wish to thank the staff members of the nanofabrication facility for allowing me to use the equipment, materials, lab facilities and Mark Biesinger from Surface Science Western for performing the XPS analysis for my samples.

My special thanks go to my group members Rony Sharon, Dr. Bernd Grohe, Karina Jasinski, Spencer Cook for their valuable tips. Also my heartfelt thanks are extended to all my colleagues who stood beside me during this journey.

Moreover, I would like to extend my appreciation to my family members for their moral support, love and encouragement they gave me to persuade my interest in this research although they are thousand miles apart. Finally, I am really thankful to my husband Kandeepan for his continuous support, unlimited love, patience and understanding.

Contents

Abstract.....	ii
Acknowledgements.....	iii
Contents.....	iv
List of Figures.....	viii
List of Tables.....	xi
List of Abbreviation.....	xii
1.0 Introduction.....	1
1.1 Background.....	1
1.2 Aim of the Thesis.....	3
1.3 Thesis Outline.....	5
2.0 Theoretical Background.....	6
2.1 Overview.....	6
2.2 LSPR Based Sensing.....	6
2.2.1 LSPR.....	6
2.2.2 Evanescent Field.....	8
2.2.3 Sensing.....	8
2.2.4 Specific Binding.....	10
2.2.5 Advantages.....	12
2.3 Self-assembly.....	13
2.3.1 Introduction.....	13
2.3.2 Formation of SAMs.....	14
2.3.3 Applications of SAMs.....	14
2.4 OMCVD.....	15
2.4.1 Introduction.....	15
2.4.2 Principle and Reactions involved in OMCVD.....	16
2.4.3 Advantages of OMCVD.....	19

2.5	AuNP functionalized Channel Waveguide.....	20
2.5.1	Propagation of Light through Waveguide.....	20
2.5.2	Types of Channel Waveguides.....	22
2.5.3	Channel Waveguide Coupled LSPR Sensor.....	23
3.0	Materials and Methods.....	25
3.1	Overview.....	25
3.2	Materials.....	25
3.2.1	Gold Precursor (trimethylphospinegoldmethyl).....	25
3.2.2	Trogamid ®.....	26
3.2.3	Nylon 6, 10.....	26
3.2.4	Polyacrylamide.....	27
3.2.5	Polystyrene (PS).....	28
3.2.6	Octadecyltrichlorosilane (OTS).....	28
3.2.7	Biotinylated Thiol.....	29
3.2.8	-OH Terminated Thiol (11-mercaptoundecanol).....	29
3.2.9	Solvents.....	30
3.3	Methods.....	31
3.3.1	Attempt to Grow AuNPs on Amine-Bearing Polymers Directly using OMCVD.....	31
3.3.2	AuNP Decorated PS Films.....	32
3.3.2.1	Cleaning the Glass Substrates.....	33
3.3.2.2	Spin Coating.....	33
3.3.2.3	Creating –OH Groups on Polystyrene.....	35
3.3.2.4	Contact Angle Measurements.....	38
3.3.2.5	Octadecyltrichlorosilane (OTS) Silanization of the Chamber.....	40
3.3.2.6	OMCVD Process.....	43
4.0	Characterization.....	44
4.1	Overview.....	44
4.2	X-Ray Photoelectron Spectroscopy (XPS).....	44

4.2.1	Principles.....	44
4.2.2	Instrumentation.....	46
4.2.3	Data Analysis.....	47
4.3	UV-Visible Spectrometer.....	48
4.3.1	Principles.....	48
4.3.2	Instrumentation.....	48
4.3.3	Data Analysis.....	50
4.4	Scanning Electron Microscope (SEM).....	51
4.4.1	Introduction.....	51
4.4.2	Instrumentation.....	51
4.4.3	Imaging.....	53
4.5	Sensing Experiments.....	53
4.5.1	Bulk-Sensing.....	54
4.5.2	Bio-Sensing.....	54
5.0	Experimental Results and Discussion.....	57
5.1	Overview.....	57
5.2	OMCVD Directly on Amine-Bearing Polymers.....	57
5.2.1	Trogamid ®.....	58
5.2.2	Nylon 6, 10.....	59
5.2.3	Polyacrylamide.....	60
5.3	OMCVD on Oxygen Plasma Treated Plain Glass.....	61
5.4	AuNP Decorated PS Films.....	63
5.4.1	LSPR Spectra of AuNPs.....	63
5.4.2	Scanning Electron Microscopy (SEM).....	66
5.4.3	Contact angle measurements.....	67
5.4.4	Image of Oxygen Plasma Treated PS Spin Coated Samples.....	68
5.4.5	XPS-Results: Oxygen Concentration on Polystyrene Surface.....	69
5.4.6	Bulk Sensing and Figure of Merit.....	75
5.4.7	Bio Sensing.....	77

6.0	Conclusion and Future Work.....	82
6.1	Conclusion.....	82
6.2	Future Work.....	83
6.2.1	Fabricate Immobilized AuNPs on Alternative Transparent Polymers using OMCVD and Test the Bulk Sensing Ability.....	84
6.2.2	Fabricate a Polymer Channel Waveguide with the Aid of a Mask	84
6.2.2.1	Design a Photo Mask.....	85
6.2.2.2	Fabricating a Channel Waveguide using PS and PMMA.....	86
6.2.3	Characterizing the Fabricated Channel Waveguide.....	87
6.2.4	Fabricate Immobilized AuNPs on Polymer Channel Waveguides using OMCVD and Test the Bulk Sensing Ability.....	89
6.2.5	Investigate the Real-Life Biosensing Capabilities using Cancer Surface Marker Protein Epidermal Growth Factor Receptor (EGFR).....	90
	References.....	93
	Appendices	
	Appendix A: Copyright Permission for Fig. 3.15.....	106
	Appendix B: Copyright Permission for Chapter 5.....	108
	Curriculum Vitae.....	110

List of Figures

2.1	Localised surface plasmon resonance induced by a polarized electric field.....	7
2.2	Evanescent field around a nanoparticle during LSPR.....	8
2.3	Binding of target analyte to a recognition site and the corresponding red-shift of the LSPR peak.....	12
2.4	Self-assembled monolayer.....	14
2.5	Illustration of steps involved in OMCVD process.....	17
2.6	Schematic of total internal reflection at the interface between two media having indices of refractions n_1 and n_2 ($n_1 > n_2$).....	20
2.7	Mode profiles in a waveguide.....	21
2.8	Channel waveguide types a) buried b) ridge c) strip-loaded.....	22
2.9	Waveguide coupled LSPR sensor.....	24
3.1	Chemical structure of trimethylphospinegoldmethyl ($[(CH_3)_3P]AuCH_3$).....	26
3.2	Molecular structure of Trogamid®.....	26
3.3	Molecular structure of nylon 6, 10.....	27
3.4	Molecular structure of polyacrylamide.....	27
3.5	Molecular structure of polystyrene.....	28
3.6	Molecular structure of octadecyltrichlorosilane (OTS).....	28
3.7	Molecular structure of biotinylated thiol.....	29
3.8	Molecular structure of –OH terminated thiol.....	29
3.9	Scheme of spin coating technique.....	35
3.10	Schematic diagram of reactive ion etch system.....	37
3.11	Illustration of contact angles of a) hydrophilic and b) hydrophobic surface.....	39
3.12	Schematic of an experimental setup capturing the image of the drop.....	40
3.13	Silanization of silicon substrates with octadecyltrichlorosilane (OTS).....	41
3.14	Scheme of the OMCVD setup (Erden et.al, Chem. Vap. Deposition 2013, 19, 338 – 346).....	42
4.1	Scheme of photoemission process at a sample surface in XPS surface analysis..	45
4.2	Schematic of double beam UV- visible spectrophotometer.....	49
4.3	Schematic of scanning electron microscope.....	52

4.4	Scheme of the final assembly of streptavidin on a biotinylated SAM.....	56
5.1	Absorption spectra of Trogamid®: a) as spin coated and b) after OMCVD (17 min, 77 °C, 6 Pa)	58
5.2	Absorption spectra of nylon 6, 10: a) as spin coated, and b) after OMCVD (17 min, 77 °C, 6 Pa).....	59
5.3	Absorption spectra of polyacrylamide: a) as spin coated, and b) after OMCVD (17 min, 77 °C, 6 Pa).....	60
5.4	Absorption spectra of a) plain glass, and b) after OMCVD (17 min, 77 °C, 6 Pa) on OH functionalized glass.....	62
5.5	UV-Vis absorption spectra of ethanol-rinsed AuNPs fabricated via 20 min OMCVD (77 °C, 6 Pa) on PS treated over various oxygen plasma times.....	63
5.6	UV-Vis absorption peak position (λ_{\max}) of AuNPs on PS versus oxygen plasma treatment time.....	64
5.7	FWHM of LSPR peaks of rinsed and non-rinsed AuNPs on PS versus oxygen plasma time.....	65
5.8	SEM image of AuNPs OMCVD grown on PS (2 min UV ozone).....	67
5.9	Images of PS spin-coated samples treated with increasing oxygen plasma time against a black background. From left to right: 0, 5, 10, 30, 45 min.....	68
5.10	XPS survey spectra of PS spin-coated films; a) untreated, and b) treated at 2 min oxygen plasma.....	70
5.11	O 1s peak height versus oxygen and UV ozone plasma time. The inset shows the first 60 s for the UV ozone treatment.....	71
5.12	High resolution XPS C 1s spectrum of PS a) before and b) after 2 min exposure to oxygen plasma treatment.....	72
5.13	High resolution XPS O 1s spectrum of PS after 2 min exposure to oxygen plasma treatment.....	74
5.14	UV-Vis absorption spectra of AuNPs on PS (oxygen plasma time: 2 min) immersed in various solvents exhibiting different refractive indices.....	75
5.15	LSPR peak spectral position versus refractive index of the solvents. The slope delivers the FOM for bulk sensing.....	77

5.16	LSPR peak position versus streptavidin concentration on a biotinylated OMCVD AuNP on PS. The black line represents the base line and red line the base line plus three times the detection uncertainty.....	79
6.1	Molecular structure of PMMA.....	83
6.2	Possible mask design.....	85
6.3	Fabrication of channel waveguide using PS and PMMA.....	86
6.4	Top view of the fabricated channel waveguide.....	87
6.5	Waveguide characterization setup: a) prism coupling setup b) mode spectrum...	89
6.6	Side view of the proposed sensor device.....	90
6.7	Illustration of antibody fragment and selective recognition of EGFR cancer surface marker (antigen) on its specific antibody, functionalized on gold surface: a) structure of the antibody b) EGFR binding mechanism.....	91

List of Tables

3.1	Solvents necessary to grow and characterize AuNPs.....	30
-----	--	----

List of Abbreviation

Au	Gold
AuNPs	Gold nanoparticles
CVD	Chemical vapor deposition
DI	Deionized
EGFR	Epidermal growth factor receptor
HMDS	Hexamethyldisilazane
LOD	Limit of detection
LSPR	Localised surface plasmon resonance
NPs	Nanoparticles
OMCVD	Organo-metallic chemical vapour deposition
OTS	Octadecyltrichlorosilane
PS	Polystyrene
PVD	Physical vapor deposition
RIE	Reactive ion etching
SA	Streptavidin
SAMs	Self assembled monolayers
SEM	Scanning electron microscopy
UVO	Ultraviolet ozone cleaner
UV-Vis	Ultraviolet – Visible
XPS	X-ray photoelectron spectroscopy

Chapter 1

1.0 Introduction

1.1 Background

The enormous potential of nanotechnology was first introduced in 1959 by renowned physicist Richard Feynman in his talk “There's Plenty of Room at the Bottom”, in which he described a number of interesting paths to manipulate matter on an atomic scale [1]. Nanotechnology can be defined as the manufacturing and use of materials, which in one or more dimensions is less than 100 nm in size [2]. Today this field has become a rapidly growing field. Nanostructured materials constitute a new generation of advanced materials that are expected to exhibit unusual chemical and physical properties different from those of either the bulk materials or single atoms [3]. The unique properties such as increased surface to volume ratio and nanoscale phenomenon may provide advantages over bulk materials due to their atomic scale structures. These nanostructured materials are of vital interest because of their broad impact to the emerging field of disciplines in nanoengineering, nanoelectronics and nanobioelectronics [4].

Presently diagnostic test for cancer are insufficient in the sense that by the time cancer is detected it becomes too late for meaningful treatment. Early detection is important because when abnormal tissue or cancer is found early, it may be easier to treat. Also the detection is mostly done by expensive equipment such as MRI (magnetic

resonance imaging), CT (X – ray computed tomography) and PET (positron emission tomography) scan etc. Now, researchers worldwide are testing simpler methods to spot the subtle signs of cancer. Nanotechnology has led to the advancement of many nanoscale biosensors that have exquisite sensitivity and versatility. The ultimate goal of nanobiosensors is to detect any biochemical and biophysical signal associated with a specific disease at the level of a single molecule or cell. They can be integrated into other technologies such as lab-on-a-chip to facilitate molecular diagnostics. Nanotechnology, with its enhanced sensitivity and reduced instrumentation size, will rapidly improve our current biodiagnostic capacity with respect to specificity, speed, and cost. Reduction in sensor size provides great versatility for incorporation into multiplexed, transportable, wearable, and even implantable medical devices [5].

Label-free biosensors such as localized surface plasmon resonance (LSPR)-based biosensors, with the potential of high-throughput and real-time analysis could make significant improvements in clinical diagnostics [6]. LSPR is a coherent, collective spatial oscillation of the conduction electrons in a metallic nanoparticle (NP), which is excited by electromagnetic radiation [7]. The wavelengths at which LSPR occurs depends on the NP's material, size and shape and as well is very dependent on the refractive index of the surrounding medium. Noble metal NPs, especially AuNPs are mainly used in LSPR sensors due to their chemical stability and ease of fabrication [8]. Binding of biomolecules to the surface of AuNPs result in a change in the refractive index that can be detected spectrophotometrically by monitoring the shift in the absorption peak intrinsic to AuNPs [9]. When functionalized with the corresponding recognition molecule, AuNPs can be utilized to detect the presence and concentration of a predetermined analyte.

Modifying the AuNPs with ligands specifically targeting to biomarkers on cancer cells allows molecular-specific imaging and detection of cancer [10]. Therefore, by functionalizing the AuNPs with an antibody specific to a cancer marker, a particular cancer marker can be detected specifically.

The stability and the attachment of the AuNPs on the surface is crucial to optimize the performance of the sensor and to reduce the potential health risks of exposure to nanomaterials. Gold nanostructures can be grown on a substrate by a method called OMCVD, in which an organo-metallic precursor is used. This process has many advantages over the colloidal methods of immobilizing AuNPs onto surfaces, such as the OMCVD process does not need any stabilizing agent to control aggregation of NPs and the particles can be grown on selected growth areas [11]. Further, the OMCVD process does not require any expensive equipment such as electron beam lithography, which is used in nanofabrication technique to pattern AuNPs on a substrate [12].

Therefore, with the current rapid development in the nanofield, it is most likely that the number of biosensors employing NPs will increase dramatically in the near future.

1.2 Aim of the Thesis

Most of the LSPR biosensor systems, which are published, are either solution based or fabricated on glass chips, which are brittle and therefore easy to break [13]. In addition, they are limited to the research based level due to the high cost of fabrication. This drawback can be overcome by using sensor chips fabricated on transparent polymers [14].

Because of their broad range of properties such as good mechanical and easily adjustable properties, both synthetic and natural polymers play an essential role in everyday life. They are now being used in almost every industry such as packaging, automotive components and medical implants [15]. Increasingly polymers offer a lot of advantages for medical and biosensor technologies due to the relatively low cost materials, simple fabrication techniques, transparency, chemical stability, deposition on various types of substrates using methods compatible with all microelectronic and micro fabrication technologies, as well as the wide choice of their molecular structure for functionalization. Specifically, the significant cost efficiency, with polymer materials costing a fraction of those made from glass or silicon makes them a vital material in sensor technology [16]. Although in a laboratory research level, the cost difference can be unimportant, however during high volume production the end savings can be economically significant. Further, since most of the polymeric materials are flexible, they can be easily incorporated into lab on a chip technology. In addition, since they are low weight, the sensors made out of polymers are easy to handle, and can be used for one time use only.

Our goal is to fabricate immobilized AuNPs on a transparent polymer using the OMCVD process for biosensing purposes. Therefore, by the combination of polymer material with a low cost fabrication method for AuNPs, in future it will allow an inexpensive mass fabrication of AuNP carrying polymer samples; from solid substrates to flexible foils implementing integrated optics.

1.3 Thesis Outline

This thesis contains six chapters organized as follows. The first chapter gives a general introduction incorporating the rationale for the research. In the second chapter, we will present the theoretical background necessary for the understanding of the thesis. It will describe the details of LSPR sensing using AuNPs, evanescent fields, self-assembled monolayers, specific recognition, OMCVD process and channel waveguide based sensors. The third chapter will provide information on the materials and methods used to grow immobilized AuNPs on polystyrene (PS), the polymer chosen in this thesis. In the fourth chapter, characterization techniques such as XPS, UV-Vis spectroscopy and SEM imaging are discussed. It will be followed by some sensing experiments with the fabricated AuNPs. Furthermore, the results obtained in our research are discussed in chapter 5. Finally, the last chapter will contain the conclusions of the work followed by suggestions for future work.

Chapter 2

2.0 Theoretical Background

2.1 Overview

This chapter intends to provide some background information of the terminologies used in the research. At the beginning the definition of LSPR and the formation of the evanescent field are explained. It will be followed by the principles of LSPR based biosensor, which involves the specific binding as well. Then self-assembled monolayers (SAMs) and its applications will be discussed. Next, a detailed description of the OMCVD process is given which is used to fabricate immobilized AuNPs on PS. Here the principles behind OMCVD process and advantages of this process over the other fabrication methods are discussed. In the final section, types of channel waveguides and propagation of light through them along with the use of channel waveguides with AuNPs in enhancing the sensitivity of the sensor are explained.

2.2 LSPR Based Sensing

2.2.1 LSPR

Over the last decade, LSPR sensing has been demonstrated to be an exceedingly powerful and quantitative probe in biomedical applications [17]. In the presence of the oscillating electromagnetic field of the light, the free electrons of the metallic nanoparticles undergo

an oscillation with respect to the metal lattice. When the frequency of the incident light matches the natural frequency of the oscillating surface electrons, this process is resonant and is termed the LSPR [18]. When nanoparticles are exposed to the alternating electric field of the incident light, the conduction electrons in the metal will become slightly displaced relative to their nuclei at the frequency of the incident light. Due to the Coulombic attraction between the electrons and nuclei, the restoring force will bring back the electrons to equilibrium and thus continues to produce oscillation of the electrons. In small particles, i.e. when the diameter (d) is much smaller than the wavelength (λ) of the incident light ($d \ll \lambda$), the electrons oscillate collectively in the nanoparticle as a standing wave motion, referred to as LSPR as shown in Fig. 2.1. In this limit, that is when ($d \ll \lambda$), the magnitude of the electric field appears static around the nanoparticle and therefore near field coupling is valid. For particles that are placed at a distance $d \gg \lambda$, radiative coupling dominates. The LSPR is very sensitive to changes of the dielectric properties of the surrounding medium, size and shape of the nanoparticle and will result in differences in the LSPR response.

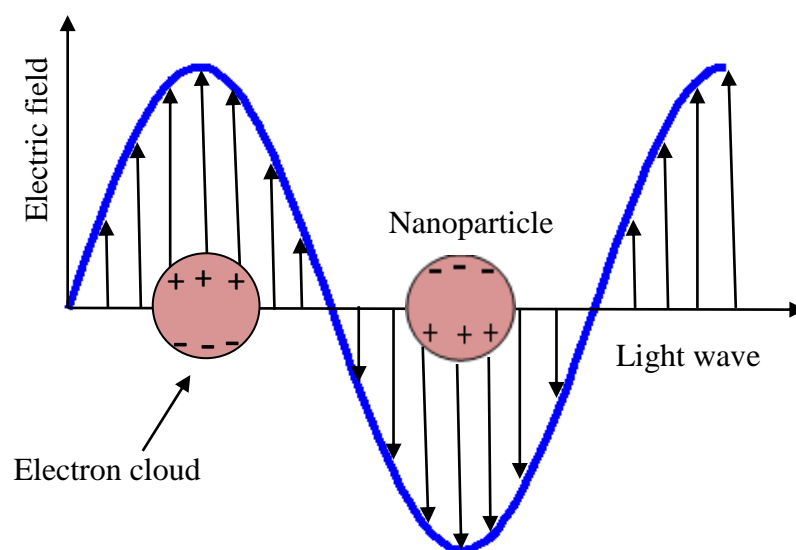


Fig. 2.1 Localised surface plasmon resonance induced by a polarized electric field [18]

2.2.2 Evanescent Field

During the LSPR resonance condition, a maximum absorption of the incident light occurs and a field enhancement happens around the particle. This field is highly localized at the nanoparticle's surface and decays rapidly away from the nanoparticle/dielectric interface exponentially which is called the evanescent field (Fig. 2.2) [19]. Since at resonance, particles absorb a large amount of energy which will be converted into heat, a peak will be obtained in the absorption spectrum at a wavelength called peak wavelength (λ_{max}).

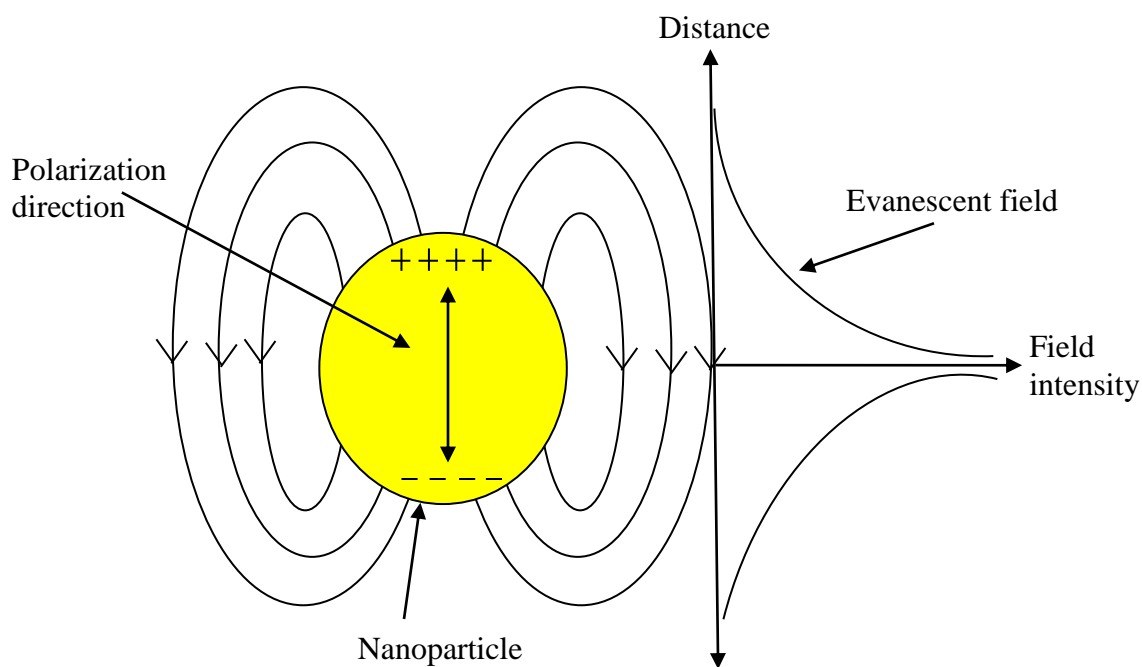


Fig. 2.2 Evanescent field around a nanoparticle during LSPR [19]

2.2.3 Sensing

A biosensor is a device that converts the presence and the concentration of a specific biomolecule to a physically measurable signal. It contains mainly two parts; a bioreceptor

and a transducer. The bioreceptor is a biological component that recognizes the target analyte (biomarker) and the transducer is a physiochemical detector component that converts the chemical recognition event into a physical signal that can be measured and quantified [20]. The sensitivity to refractive index changes makes nanoparticles very useful for the biosensing purposes, provided that they are enabled to specifically interact with the analyte of interest. In surface-sensitive LSPR biosensors, one of the interacting biomolecule is immobilized on the NP surface and its interaction with its biospecific partner is observed through the shift in the resonance position or by monitoring the appearance of a cross-talk peak [21]. Only alterations in the refractive index near the NP surface are sensed as the LSPR is only sensitive to the medium within roughly one wavelength (that of the LSPR) distance from the surface [22]. For visible light, only changes in refractive index occurring at distances within ~ 200 nm of the particle surface cause sufficient changes in the optical properties of the nanoparticles [23, 24].

The excitation of the LSPR of NPs only occurs with NP-materials which have a complex dielectric constant of real part which has a negative value and its magnitude larger than the positive imaginary part of the dielectric constant [25]. However, for noble metals, the LSPR peak wavelength depends only on the real part of the dielectric function and the width of the resonance peak depends only on the imaginary part of the dielectric function. Noble metal particles such as gold and silver exhibit these properties and also have a strong optical extinction at visible and near-infrared (NIR) wavelengths. Therefore, these are the most commonly used elements for LSPR-based biosensing. Although silver exhibits many advantages over gold, such as higher extinction coefficients, sharper extinction (LSPR) bands and extremely high field enhancements

[26], AuNPs are the most extensively used NPs due to their unique tunable optical properties, low toxicity, chemical stability, biocompatibility and their amenability of synthesis and functionalization [27]. AuNPs with sizes up to a few 10s of nm show a LSPR in the visible; UV–Vis spectroscopy can therefore assist in the detection of the spectral position of the LSPR and its shift.

2.2.4 Specific Binding

The interaction between two species that has a particularly high and exclusive affinity for one another is called specific binding. It is often depicted as a simple geometric match, with one molecule possessing a "binding pocket" shaped perfectly for its ligand (recognition site). It can be simply described as a “lock and key” mechanism in which only one unique key fits into the lock [28]. Similarly, only molecules with the correct shape and size can fit into the recognition site.

AuNPs modified with specific antibodies (recognition molecules of antigens) can recognize their antigens via immune-reaction, causing local environment changes of the nanoparticles and resulting in a peak shift in the LSPR spectrum. If the antigen (analyte) binds specifically to an antibody attached to the nanoparticles, this will induce a change, usually an increase, in the refractive index (n) which is linked to the dielectric ($\epsilon_d = n^2$) in the vicinity of the nanoparticles. This causes the position of the plasmon peak in the extinction spectra normally to shift to longer wavelengths (because less energy is required to excite the electrons) as demonstrated in Fig. 2.3. It can be seen in the equation for the plasmon resonance frequency as given in Eq. 2.1 [29]:

$$\omega_{LSP} = \frac{\omega_p}{\sqrt{1 + 2\varepsilon_d}} \quad (2.1)$$

where, ω_{LSP} is the plasmon resonance frequency, ω_p the plasma oscillation frequency of the free electron gas relative to the ion cores and ε_d the dielectric function of the dielectric surrounding.

From this equation, it is easy to see that if ε_d increases, this will result in a lower LSPR frequency leading to a red shift (shifting towards longer wavelengths). The spectral shift that occurs upon a change in the refractive index is typically in the range of a few nanometers and hence, not visible to the naked eye, but easily detectable by a UV-vis spectrophotometer [30]. When a molecule is attached to the AuNP, it changes the evanescent field around the particle and changes the resonance condition of the particle. Therefore, a different peak wavelength for resonance will be obtained and a shift can be observed in the absorption spectrum of the nanoparticle. Therefore, in order to detect a particular cancerous biomarker, initially its specific antibody should be immobilized to the AuNP and then the solution containing the biomarker should be introduced, and the specific binding of the biomarker to the antibody can be viewed through the shift in the absorption spectrum of the spectrometer. The shift should be made as high as possible so that we can easily detect the cancerous biomarkers in a patient.

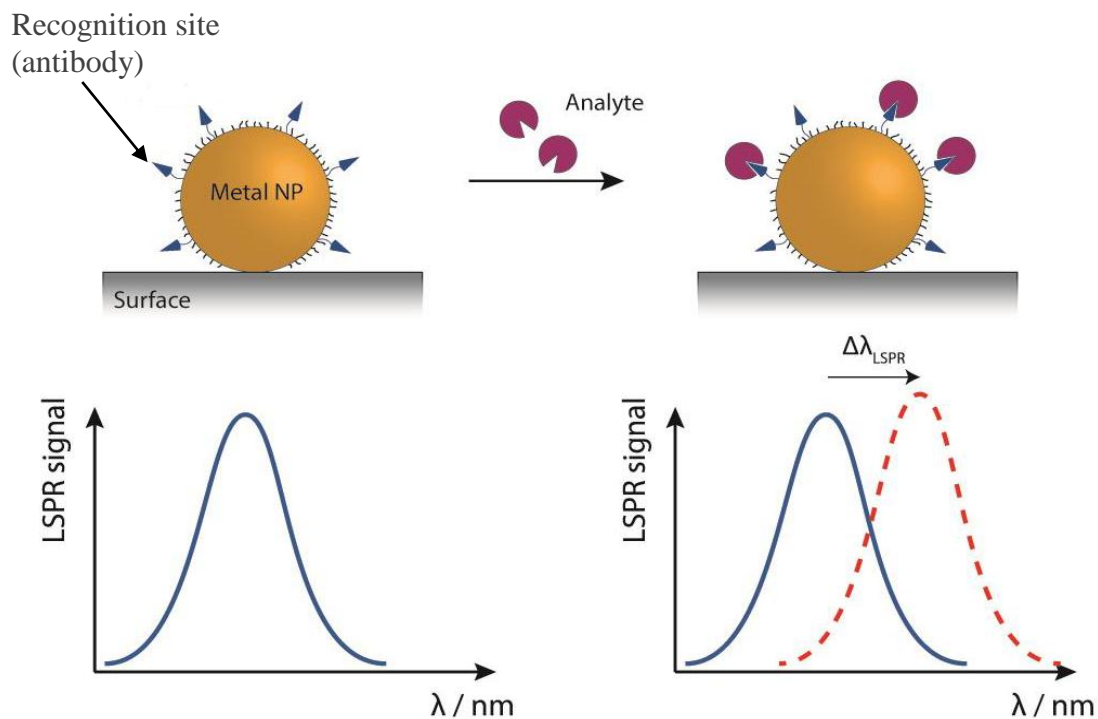


Fig. 2.3 Binding of target analyte to a recognition site and the corresponding red-shift of the LSPR peak [30]

2.2.5 Advantages

LSPR sensors are a type of surface-sensitive refractometer that is often used in label-free biosensing for direct detection of molecular adsorption that occurs within the immediate vicinity of a sensor surface. Therefore, the main advantage of these sensors is that they do not require additional chemical modification steps, such as labeling the desired antibody or antigen with enzymes, radioactive isotopes or electroluminescent tags, as in fluorescence labeling [31]. This makes the LSPR sensor a less complicated and easy instrumental setup and refrain from false signals from the labels. Also these sensors exhibit high sensitivity via detection of refractive index changes and are relatively cost-

effective, as it does not rely on expensive equipment. Further, these sensors show good reproducibility using nanoparticle substrates and provide real-time assay accessibility using microfluidic systems [6]. These advantages demonstrate that nanobiosensors can be applied in a wide range of fields, such as medical, food safety, environmental monitoring, and drug screening.

2.3 Self-assembly

2.3.1 Introduction

Nanomaterials and nanostructures can, in principle, be fabricated using both top-down and bottom-up techniques [32]. A bottom-up process uses techniques of molecular synthesis, colloid chemistry, polymer science, and related areas to make structures with nanometer dimensions which are formed atom by atom, molecule by molecule or cluster by cluster. The top-down approach uses various methods of lithography to pattern macroscopic materials to nanoscale building blocks. Self-assembly bridges these two techniques and allows materials to be designed with hierarchical order and complexity, exploiting the molecular interactions such as van der Waals forces, chemisorptive bonding, electrostatic interactions etc. [33]. Self-assembly of nanostructured materials holds promise as a low-cost, high-yield technique with a wide range of scientific and technological applications including the development of sensors [34].

2.3.2 Formation of SAMs

SAMs are organic assemblies formed by the adsorption of molecular constituents from solution or the gas phase onto the surface of solids or in regular arrays on the surface of liquids [35]. The molecules that form SAMs have a chemical functionality, or “headgroup”, with a specific affinity for a substrate. Initially the SAMs are created by quick chemisorptions of the “head groups” onto the substrate followed by a slow organization of “tail groups” as depicted in Fig. 2.4 [36].

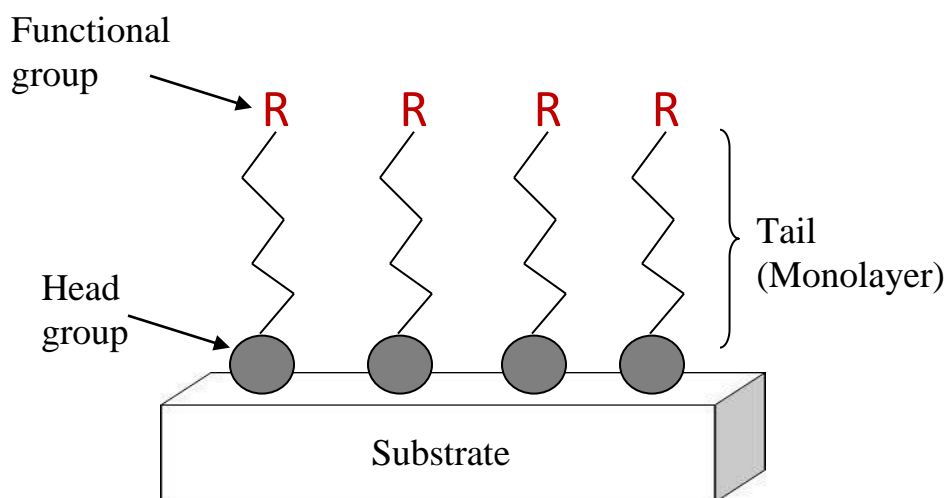


Fig. 2.4 Self-assembled monolayer

2.3.3 Applications of SAMs

There are a number of headgroups that bind to specific metals, metal oxides, and semiconductors. The most extensively studied class of SAMs is derived from the adsorption of thiols (-SH) on gold, which makes it possible to generate well-defined organic surfaces with useful and highly alterable chemical functionalities displayed at the

exposed interface [33]. We used this high affinity between the gold and thiols to immobilize biotinylated thiol molecules to the OMCVD grown AuNPs for biosensing purposes, which will be discussed in Chapter 4. Also, we grew SAMs of octadecyltrichlorosilane, to make the inner surface of the reaction chamber, where the OMCVD process occurs, a non-growth surface for AuNPs so that the AuNPs are efficiently formed only on the functionalized substrates. The details of this process will be described in Chapter 3.

2.4 OMCVD

2.4.1 Introduction

OMCVD is a versatile process in which organo-metallic gas-phase molecules are decomposed to reactive species, leading to thin films and nanostructures of metals on functionalized surfaces [37]. It's an alternative method to physical vapour deposition (PVD) for deposition of thin solid chemical material in the gas phase by a chemical reaction and has attracted increasing interest in recent years. The main advantages of OMCVD over physical vapor deposition (PVD) techniques, such as sputtering or evaporation, are the ability to controllably create films of widely varying stoichiometry and to uniformly deposit materials selectively on so-called growth areas with reactive functional groups [23].

Palgrave et al. had used hydrogen tetrachloroaurate ($\text{HAuCl}_4 \cdot 3\text{H}_2\text{O}$) and tetraoctylammonium bromide as aerosol assisted CVD precursors to form films of

metallic AuNPs with narrow size distributions [38]. Wu et al. demonstrated a high-throughput chemical vapour deposition growth of carbon or graphene shells encapsulating AuNPs using a xylene CVD process [39]. Binions et al. deposited thermochromic fluorine doped thin films of vanadium dioxide from the aerosol assisted CVD reaction of vanadyl acetylacetonate, ethanol and trifluoroacetic acid on glass substrates [40]. In our group previously, deposition of gold onto thiol-functionalized organic monolayers using OMCVD was demonstrated. But then it had turned out that thiol-terminated surfaces generate chemically unstable AuNPs which detach when brought in contact with a solvent. This leads to irreversible false sensor signals due to undesired AuNP clustering on the thiolated surface [41]. As a solution to the problem, AuNPs were grown on glass on the polar amine-termination group, which delivered chemically stable, well immobilized AuNPs with excellent sensor response [42]. We first attempted to grow AuNPs on amine-terminated polymers, but this was not successful, possibly due to a low number of amine groups exposed at the surface. Therefore, we utilized the polar oxygen group to serve as the nucleation site for the growth of AuNPs on treated PS using the OMCVD process.

2.4.2 Principle and Reactions involved in OMCVD

The principle of an OMCVD process is to vaporize a metal-containing organic precursor, (an organo-metallic complex), at relatively low temperatures and under reduced pressure and deposit the metal either as a layer or as NPs on a functionalized substrate [42]. Initially, a volatile precursor is transported into a reactor chamber which contains one or more heated substrates to be coated. When the precursor evaporates and touches the functionalized surface, the precursor molecule breaks up and releases the metal atom

from the molecule. Then adsorption and chemical reactions occur on and near the hot surfaces, resulting in the deposition of the metal or a thin film on the surface. This is accompanied by the production of chemical by-products that are subsequently desorbed from the substrate surface and diffused into the low pressure reaction chamber along with unreacted precursor gases. The metal atoms then diffuse to form a stable nucleus, where subsequent growth occurs. The basic steps involved in the chemical vapour deposition are illustrated in Fig 2.5.

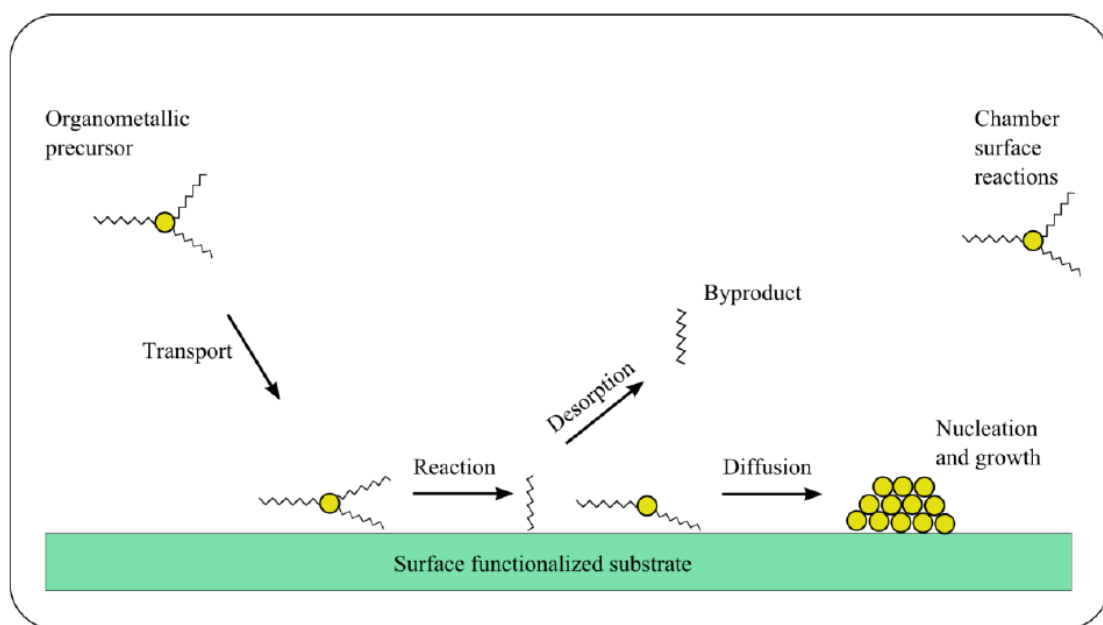
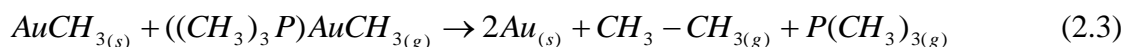
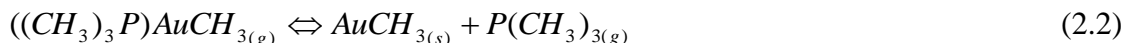


Fig. 2.5 Illustration of steps involved in OMCVD process [19]

There are three different growth mechanisms for the nanoparticles to grow on the substrate depending on the interaction strength between the film atoms and the surface. They are i) island growth (Volmer-Weber), in which the atoms are more strongly bound to each other than to the substrate forming 3-D islands, ii) layer-by-layer growth (Frank-

van der Merwe), where the atoms more strongly bound to the substrate than to each other and iii) mixed growth (Stranski-Krastanov) mechanism, in which both mechanisms occur, initially forming layer-by-layer and then 2D islands. By carefully controlling the functionalization on the substrate, and the deposition parameters, such as the temperature and the reaction period, metallic NPs can be formed at a desired size and density on a surface by the Stranski-Krastanov mechanism [43].

In our research, the volatile organometallic precursor used for OMCVD of gold is trimethylphosphinegoldmethyl ($((\text{CH}_3)_3\text{P})\text{AuCH}_3$), which is known to give pure gold films at low temperatures [42]. When the precursor evaporates and gets in contact with the functionalized surface, the precursor molecule breaks up and releases the gold atom from the molecule. The gold atom attaches to the functionalized substrate surface or another gold atom previously deposited forming AuNPs. The byproducts, trimethylphosphine and the ethane stay in the vapor phase. The reaction mechanism of the precursor to the surface is illustrated in Eq. 2.2 and 2.3 [44].



Using an oven as a heat source for the reactor increases the evaporation of the precursor. However, this method does not create a uniform temperature distribution yielding to high inhomogeneities. Placing the chamber partially in an oil bath provides a

uniform temperature across the chamber, increasing the homogeneity along the sample surface as well as between the samples and increasing reproducibility significantly.

2.4.3 Advantages of OMCVD

When comparing with colloidal particles prepared by wet chemical methods, the OMCVD grown particles do not need any stabilization agents to control particle aggregation [45]. AuNPs tend to be fairly unstable in solution, so special precautions have to be taken to avoid their aggregation or precipitation. This is achieved by adding a citrate layer or a polymer coating to create core-shell structure making them complicated [46]. Further colloidal gold requires additional handling considerations for lab-on-a-chip applications. In contrast, since the metal NPs are covalently bonded to the functionalized surface, these particles are not environmentally challenging unlike in electrostatic bonding between the colloidal particles. Also the particles are free and flexible for further functionalization, since they are not capped and thus more preferable for sensing purposes. Further, since the whole procedure is performed under low pressure and relatively low temperatures, the OMCVD process is a fast, simple and economical method to obtain safe and controlled deposits of high quality metal NPs.

2.5 AuNP functionalized Channel Waveguide

2.5.1 Propagation of Light through Waveguide

Optical channel waveguide sensors utilizing an evanescent field probing scheme have drawn great interests in biosensing due to its high sensitivity and label-free analyte

detection [47]. Optical waveguides are comprised of an optically transparent guiding layer (waveguide core) with a refractive index that is higher than the substrate layer (or the cladding) [48]. When light is coupled into the guiding layer of a waveguide, light is guided over long distances by a process called total internal reflection (Fig. 2.6). Total internal reflection is a phenomenon which occurs when a propagating wave strikes a medium boundary at an incident angle (θ_i) larger than a particular critical angle (angle of incidence above which the total internal reflection occurs) with respect to the normal to the surface [49]. During the total internal reflection, the wave undergoes a lateral displacement (D) due to the displacement (s) along the surface as indicated in Fig. 2.6. This is referred to as the “Goos-Hanchen effect”, resulting from the propagation of an evanescent wave parallel to the interface [50].

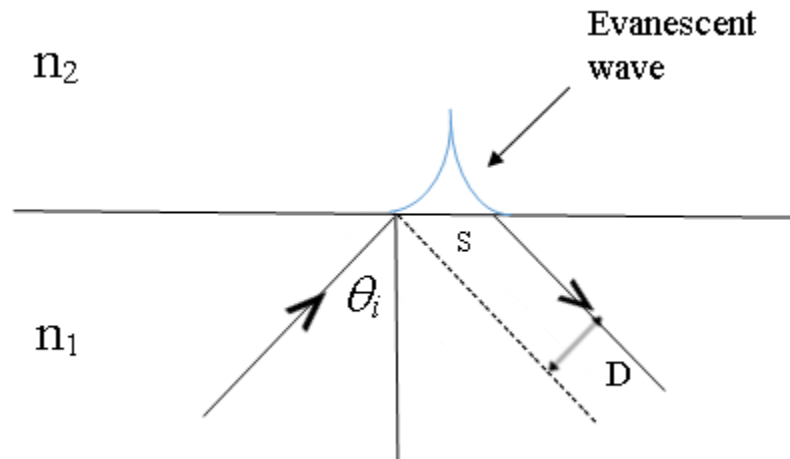


Fig. 2.6 Schematic of total internal reflection at the interface between two media having indices of refraction n_1 and n_2 ($n_1 > n_2$) [50]

As the guided light travels through the waveguide, it produces different modes, which are solutions to the Maxwell's equations, depending on the boundary conditions at the interfaces, and the way the wave is coupled into the waveguide. It can be either transverse electric (polarized light whose electric field is normal to the plane of incidence) such as TE_0 , TE_1 , TE_2 etc. as shown in Fig. 2.7 or transverse magnetic (polarized light with its electric field parallel to the plane of incidence) modes in the waveguide medium, depending on the direction of polarization [51]. A mode in the waveguide is defined as a transverse field pattern whose amplitude and polarization profiles remain constant along the propagation direction and is achieved only when all the reflected waves in the waveguide constructively interfere between them [51].

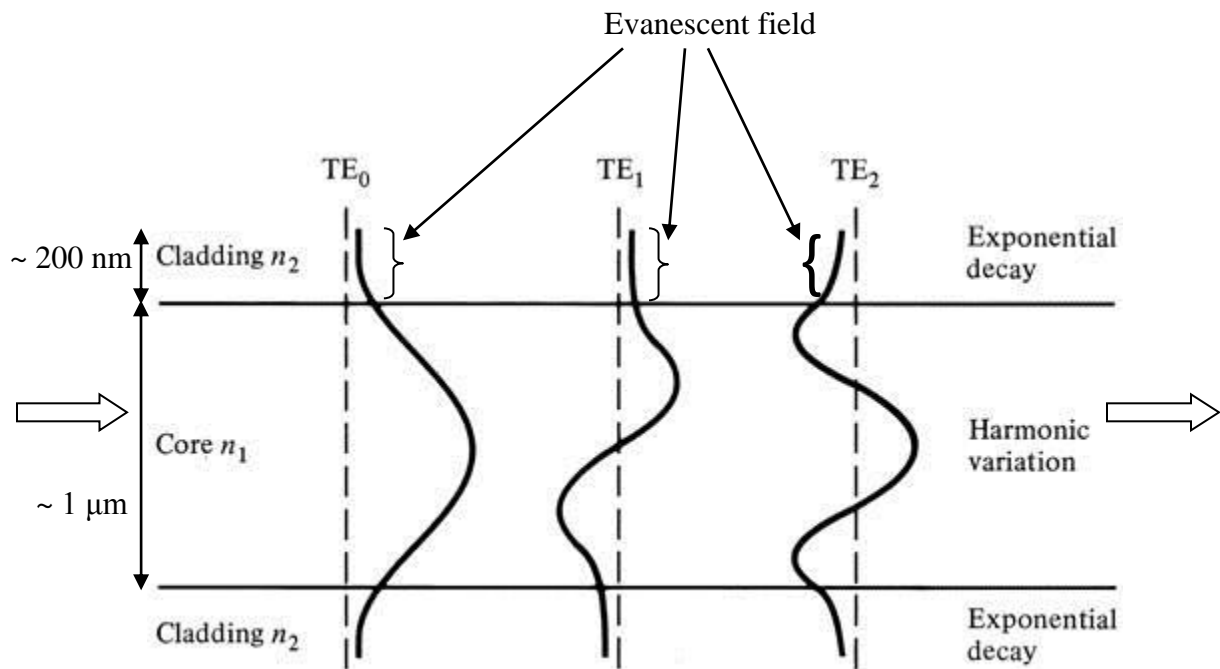


Fig. 2.7 Mode profiles in a waveguide [51]

2.5.2 Types of Channel Waveguides

A channel waveguide is a device, which offers confinement in two dimensions as opposed to the one dimensional confinement offered by planar or slab waveguides. Therefore, these waveguides will provide a high confinement of light. Fig. 2.8 shows cross sections through the most common geometries of channel waveguides such as buried, ridge and strip-loaded [52]. Buried type channel waveguides are made by modifying the properties of the substrate material so that a higher refractive index is obtained locally by diffusion process. The ridge waveguides are usually formed from a planar waveguide that has been patterned and etched to leave the ridges (waveguiding core) using photolithography. A ridge waveguide has strong optical confinement than the buried ones, because it is surrounded on three sides by low-index air (or cladding material) providing a large index difference between the ridge and its surrounding. The third type, strip-loaded channel waveguide is formed by loading a planar waveguide, which already provides optical confinement in the x direction, with a dielectric strip of index $n_3 < n_1$ to facilitate optical confinement in the y direction. Here the n_1 region under the loading strip acts as the waveguiding core region.

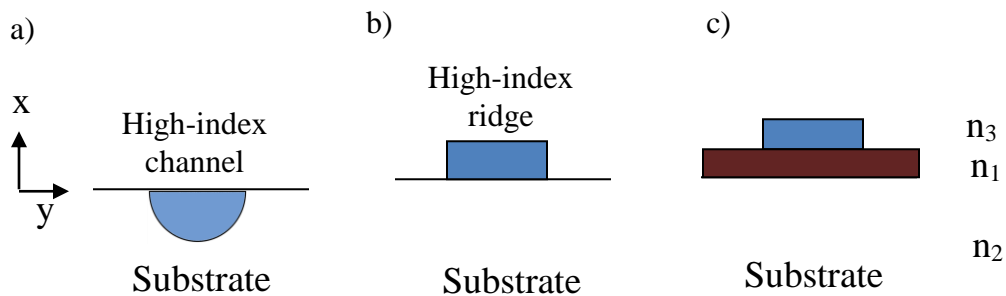


Fig. 2.8 Channel waveguide types a) buried b) ridge c) strip-loaded [53]

2.5.3 Channel Waveguide Coupled LSPR Sensor

In order to increase signal-to-noise ratio and enhance the sensitivity, waveguides can be used as substrates. Although most of the light is confined within the guiding layer, a small portion extends out into the substrate and into the medium (the biological sample), the evanescent field (Fig. 2.7). A waveguide coupled LSPR sensor configuration is where the evanescent field of the waveguide is the illumination source of the sensing particles probing the LSPR spectral position of the AuNPs as shown in Fig. 2.9. When the frequency of the incident light matches the plasmon frequency of the AuNPs, the AuNPs get excited. It should be noted here, that the AuNPs and the binding analytes still lie on the evanescent field of the waveguide as depicted in Fig. 2.9. This setup allows integrating the LSPR absorption signal along an increased interaction length along the waveguide. This will allow greater control over the interaction because of the larger interaction length between sample and probing beam and provide high LSPR absorption signal in comparison to current transmission sensors [53]. This is expected to lead to greater sensitivity. Detailed description on coupling a laser light through the channel waveguide and analysis on the sensitivity of the channel waveguide carrying AuNPs sensor are discussed in the final chapter.

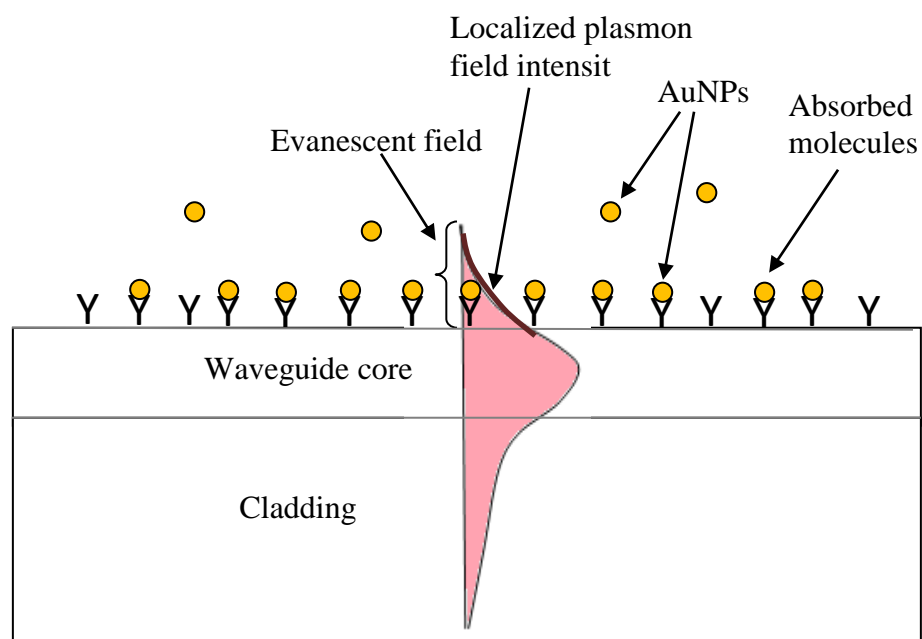


Fig. 2.9 Waveguide coupled LSPR sensor

Chapter 3

3.0 Materials and Methods

3.1 Overview

In this chapter, the materials, apparatus and methods used to grow AuNPs using OMCVD process on PS are described. Initially, a brief description of some unsuccessful experiments performed to grow AuNPs on few transparent polymers and then successful methods used to grow AuNPs on PS will be followed.

3.2 Materials

The following materials with the given chemical structures and specifications were used without further purification for the growth and characterization of AuNPs on polymers.

3.2.1 Gold Precursor (trimethylphospinegoldmethyl)

Trimethylphosphinegoldmethyl ($[(\text{CH}_3)_3\text{P}]\text{AuCH}_3$) is an organometallic precursor (Fig. 3.1) which has a very low vapor pressure. Therefore, it evaporates easily and delivers pure thin films of gold at relatively low temperatures [54]. This gold precursor was synthesized by Joseph A. Paquette, supervised by Joe B. Gilroy from Department of Chemistry, University of Western Ontario according to the literature [14].

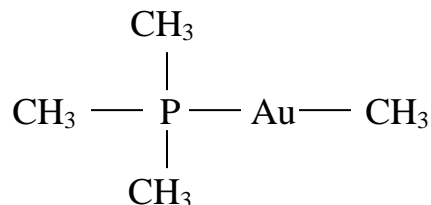


Fig. 3.1 Chemical structure of trimethylphospinegoldmethyl ($[(\text{CH}_3)_3\text{P}]\text{AuCH}_3$)

3.2.2 Trogamid ®

Trogamid ® is a transparent, amorphous polyamide with a refractive index of 1.516 at $\lambda = 589$ nm. It has a molecular structure as shown in Fig. 3.2. The polymer is amorphous and results in low molding shrinkage and low tendency to bent or twist out of shape. Trogamid exhibits high mechanical stability, high thermo stability and good chemical resistance compared to other plastics [55].

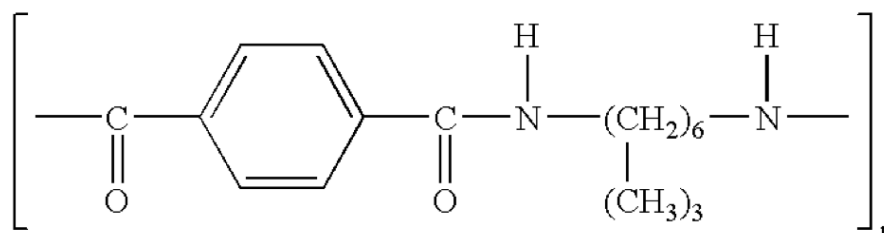


Fig. 3.2 Molecular structure of Trogamid®

3.2.3 Nylon 6, 10

Nylon 6, 10 is a semicrystalline polyamide with a molecular structure as given in Fig. 3.3. It also has a high refractive index of 1.565 at $\lambda = 532$ nm. Nylon 6/10 has lower moisture absorption than nylon 6 or nylon 6/12. It is stronger than nylon 11, nylon 12, and nylon 6/12. Nylon 6/10 retains its room temperature toughness at low temperatures better than

nylon 6 or nylon 6/6. Due to these properties, it's one of the most widely used engineering thermoplastics [56].

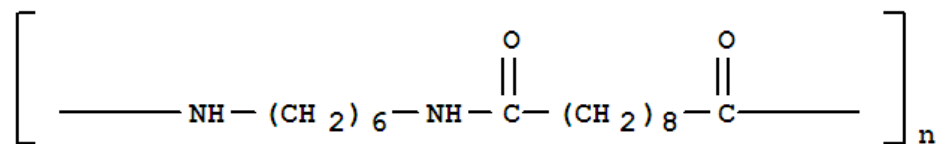


Fig. 3.3 Molecular structure of nylon 6, 10

3.2.4 Polyacrylamide

Polyacrylamide (Fig. 3.4) is a non-ionic water soluble polymer which is formed from acrylamide subunits. Through the highly reactive amide (NH₂) group, the polymer can be chemically modified to produce a positively charged cationic polymer or a negatively charged anionic polymer. It has a refractive index of 1.452 at $\lambda = 546 \text{ nm}$ [57].

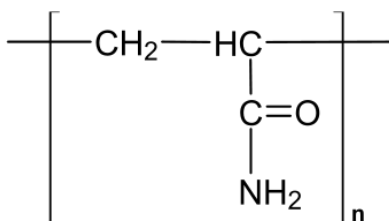


Fig. 3.4 Molecular structure of polyacrylamide

3.2.5 Polystyrene (PS)

Polystyrene is a synthetic aromatic polymer made from the monomer styrene. It's a long chain hydrocarbon, wherein alternating carbon centers are attached to phenyl groups as depicted in Fig. 3.5. Due to its unique optical properties such as high transparency in the visible region, high refractive index 1.59 at $\lambda = 584$ nm and in-expensiveness, it's widely used in waveguide optics [58]. Also PS is used in packaging, appliances, consumer electronics and disposable medical applications [59].

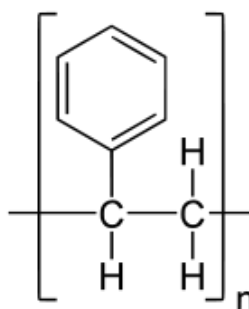


Fig. 3.5 Molecular structure of polystyrene

3.2.6 Octadecyltrichlorosilane (OTS)

Octadecyltrichlorosilane (Fig. 3.6) is an organometallic chemical consisting of a long-chain alkyl group ($C_{18}H_{37}-$) and a polar head group ($SiCl_3-$), which forms self assembled monolayers (SAMs) on various oxidic substrates. Therefore, OTS can be used to form a monolayer with CH_3 terminated groups on a surface, making the surface hydrophobic (described in section 3.4.5). It's flammable and sensitive to water and air [60].

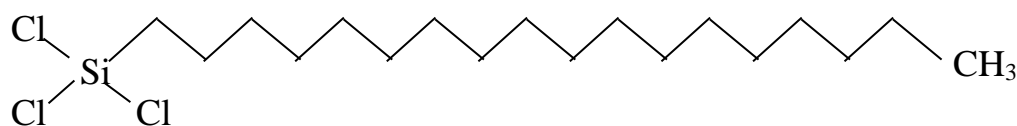


Fig. 3.6 Molecular structure of octadecyltrichlorosilane (OTS)

3.2.7 Biotinylated Thiol

Fig. 3.7 shows the molecular structure of a biotinylated thiol, which can be immobilized on noble metals for binding streptavidin and/or its conjugates onto the formed SAMs. These thiols can be used to prepare highly ordered architectures ideal for subsequent analytical studies in protein sensing [61].

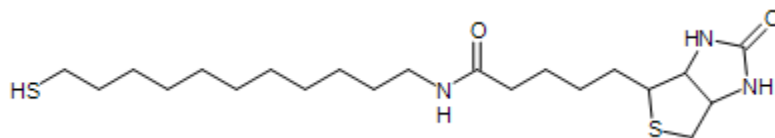


Fig. 3.7 Molecular structure of biotinylated thiol

3.2.8 -OH Terminated Thiol (11-mercaptoundecanol)

11-mercaptoundecanol (Fig. 3.8) can be widely used for material modifications to improve hydrophilicity of the surface due to its -OH terminal group. Since it has a -SH group at the other end, it can be used to prepare a highly oriented SAM on a gold surface. This would prevent non-specific binding and provide a better surface to develop biomaterial sensors or DNA/ protein microarrays [62].

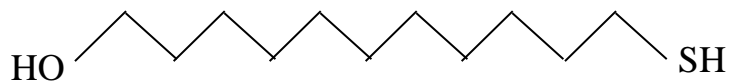


Fig. 3.8 Molecular structure of -OH terminated thiol

3.2.9 Solvents

Table 3.1 shows the specifications and the suppliers of the solvents used in the research.

Table 3.1 Chemical necessary to grow and characterize AuNPs

Solvent	Specifications	Supplier
m-cresol	Assay - 99 %	Sigma Aldrich, Canada
Chlorobenzene	Assay - 99.8%	Sigma Aldrich, Canada
Ethanol	Reagent grade, anhydrous - 95.4%	J.T. Baker, PA, USA
Methanol	Reagent grade, anhydrous - 99.8%	Bio Shop, Canada
Isopropanol	Anhydrous - 99.5%	Sigma Aldrich, Canada
Dimethylsulfoxide	Assay - 99.9%	Sigma Aldrich, Canada
Hydrogen peroxide	Assay – 29 % – 32 %	Caledon Laboratories Ltd., Ontario, Canada
Sulphuric acid	Assay – 95 % – 98 %	Caledon Laboratories Ltd., Canada
Toluene	Assay \geq 99.5 %	Caledon Laboratories Ltd., Canada

3.3 Methods

3.3.1 Attempt to Grow AuNPs on Amine-Bearing Polymers Directly using OMCVD

As mentioned in chapter 2, previously Ertorer et al. had grown surface-immobilized AuNPs on amine-terminated glass surfaces using the simple OMCVD procedure [11, 41]. They implemented the sparsely available, polar-NH groups of a monolayer of hexamethyldisilazane (HMDS) which is covalently attached to glass substrates for nucleation and growth of stable AuNPs with the trimethylphospinegoldmethyl ($[(\text{CH}_3)_3\text{P}]\text{AuCH}_3$) precursor (Fig. 3.1).

Therefore, initially we chose transparent polymers Trogamid (Evonik Industries, Germany), Nylon 6, 10 (Polysciences, Inc., PA, USA) and polyacrylamide (MW = 5,000,000, Sigma Aldrich, Canada) which exhibit polar $-\text{NH}$ or $-\text{NH}_2$ groups for AuNP growth. The molecular structures of these polymers are shown in Fig. 3.2.2 - 3.2.4. Specially, transparent polymers with high refractive indices were chosen, since these materials can be used as the core material of waveguides for the future purposes of building an all-optical-all-polymer-lab-on-a-chip implementing integrated optics, which will be described in Chapter 5. Trogamid and Nylon 6, 10 were dissolved in a solvent, m-cresol, and polyacrylamide was dissolved in DI water. These solutions were spin coated on the cleaned glass substrates and the OMCVD was performed using the gold precursor inside the silanized OMCVD glass chamber. Afterwards, the UV-Vis absorption spectra were obtained. However, the OMCVD process on these amine-bearing polymers was

unsuccessful. No LSPR signals from AuNPs could be detected. We concluded that no AuNPs were deposited onto these spin coated polymer surfaces. There are several reasons for the failure: The available amine groups were not exposed to the surface. The number of amine (NH_2) groups was too low, or simply, the amine groups do not nucleate the Au from the precursor.

3.3.2 AuNP Decorated PS Films

In a new strategy, we utilized an alternative polar group: the hydroxyl ($-\text{OH}$) group. The $-\text{OH}$ group is a good candidate for a polar nucleation site for the AuNPs. In order to test this, glass slides were oxygen plasma-treated to create $-\text{OH}$ groups at the surface, and AuNP were grown via OMCVD. This worked excellently, as demonstrated by strong LSPR peaks; AuNPs grew with the polar, free $-\text{OH}$ groups serving as the nucleation sites. Therefore, the transparent polymer polystyrene (PS) with a MW of 50,000 (Fig.3.5) was spin-coated on glass substrates and exposed to oxygen plasma or UV ozone to create $-\text{OH}$ groups for nucleation. The OMCVD process was performed on these substrates, and absorption spectra of the AuNP grown samples were obtained. Scanning Electron Microscopy (SEM) images of the AuNPs were obtained as well. Further, the chemical stability, bulk-sensing and bio-sensing capabilities of the OMCVD grown NPs were tested. The effects of the oxygen plasma and UV ozone treatments duration on the PS surface chemistry were investigated using X-ray Photoelectron Spectroscopy (XPS). The steps involved to attach surface immobilized AuNPs on functionalized PS film are following.

3.3.2.1 Cleaning the Glass Substrates

Fisher brand microscope glass slides of size 0.8 cm x 1.5 cm were cut with a diamond glass cutter and cleaned initially by 10 min ultra sonication in acetone, since acetone is a good solvent for removing greasy or oily material from the surface. Then the slides were rinsed with de-ionized (DI) water removing any ionic debris. Afterwards the substrates were ultra sonicated in isopropanol for 10 min and rinsed thoroughly with DI water. Isopropanol dissolves a wide range of non-polar compounds and evaporates quickly, leaving nearly zero oil traces. Finally, the samples were blown dry with nitrogen. To make the surfaces hydrophilic for spin coating purposes, the samples were placed for 20 min in an STS Reactive Ion Etch system (STS RIE 320 PC, Surface Technology Systems, Newport, UK; 90W) operating under oxygen gas. This further removes surface contaminants and forms a dense –OH functionalization on the surface. The increased hydrophilicity of glass slide surfaces makes them more suitable for spin-coating photoresist or other polymers [63].

3.3.2.2 Spin Coating

Spin coating is one of the most common techniques used for depositing uniform thin films from a few nanometers to a few micrometers in thickness on flat substrates [64]. The simplicity and relative ease with which a process can be set up delivering thin and uniform coating are the main factors for spin coating to be widely used for production of thin films. Usually a small amount of solution is distributed across the surface of the substrate, which is tightly held to the chuck (where the sample is kept on), by a vacuum. Then the substrate is rotated at high speed (typically around 3000 rpm) in order to spread

the solution by centrifugal force combined with the surface tension of the solution. During this time, excess amount of solvent is spinned off leaving the desired material to form an even thin film on the surface. Fig. 3.6 schematically shows the spin coating technique.

The final film thickness will depend on the nature of the solution (viscosity, drying rate, percent solids, surface tension, etc.), spin speed and acceleration of the spin process. Out of these parameters, spin speed is one of the most important factors which affect the thickness of the spin coating. With increasing spin speed, the film thickness decreases exponentially.

In order to prepare a thin film of PS, initially the PS solution was prepared by dissolving 5 g of PS granulates (Nominal Granule Size 3.5 mm, Goodfellow) in 15 mL chlorobenzene (anhydrous 99.8%, Sigma Aldrich) and allowing the solution to be stirred for several days with a magnetic stirrer. This assured the complete dissolution of the PS granulates in the chlorobenzene. Then the PS solution was pipetted on the plasma-treated glass slides and spun at 3000 rpm for 1 min in a spin coater (Headway Research, Inc.). This was followed by baking the spin-coated samples in an oven for 2 h at 90 °C under atmospheric conditions to eliminate residual solvent.

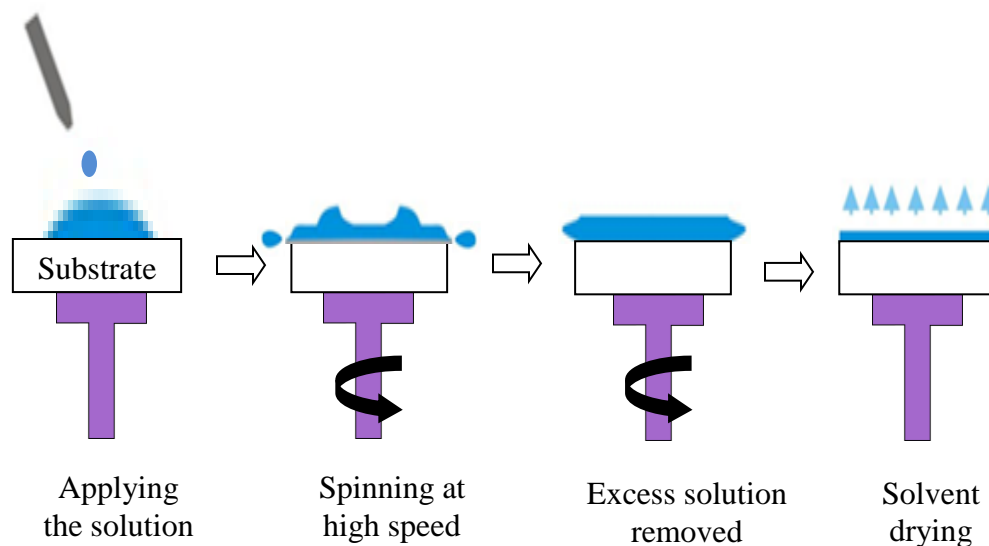


Fig. 3.9 Scheme of spin coating technique [65]

3.3.2.3 Creating –OH Groups on PS

The bulk properties of many polymers make them ideal for a wide range of structural and functional applications. However, their low surface energy in the natural state, limits their use, and pre-treatments are frequently applied to improve polymer characteristics such as adhesion and wettability [66]. PS is a polymer with a carbon backbone, which has naturally low surface energy, making the surface hydrophobic or non-wetting. Because of its hydrophobicity, surface treatments are required to introduce hydrophilic groups such as –OH groups on its surface [67]. Plasma surface treatment and UV ozone treatments are well known processes to introduce hydrophilic -OH groups on the PS surface. These processes modify the polymer surface by introducing chemically bound oxygen into the upper most atomic layers of the surface using active oxygen radicals. This results in a considerable increase in the number of functional polar groups on the substrate surface, increasing the surface energy and making the surface hydrophilic. Not only the surfaces

become more hydrophilic, the abundant polar oxygen groups will promote the AuNPs nucleation via OMCVD. Therefore, reactive ion etching and UV ozone cleaning were used to create -OH groups on PS spin coated surfaces.

Reactive Ion Etching (RIE)

In a RIE machine, plasma is initiated by applying a strong radio frequency (13.56 MHz) electromagnetic field around hundred Watt, between the two planar electrodes in a vacuum system (Fig. 3.10). The oscillating electric field ionizes a variety of source gas molecules, creating a plasma. The plasma is a partially ionised gas which contains ions, free radicals and by-products. These ions react chemically with the materials on the surface of the wafer to either make them leave or create required functional groups [68].

The PS spin coated samples were manually loaded into the process chamber of a RIE (320 PC, Surface Technology Systems, Newport, UK), operating at 90 W under oxygen gas. These substrates were subjected to the oxygen plasma at room temperature for various times (2, 5, 10, 30 and 45 min). Their hydrophilic nature (wettability) was investigated by contact angle measurements with purified water. The treatment times were varied to find the optimum time, which would create a high concentration of -OH functionalities without altering the optical quality of the PS sample.

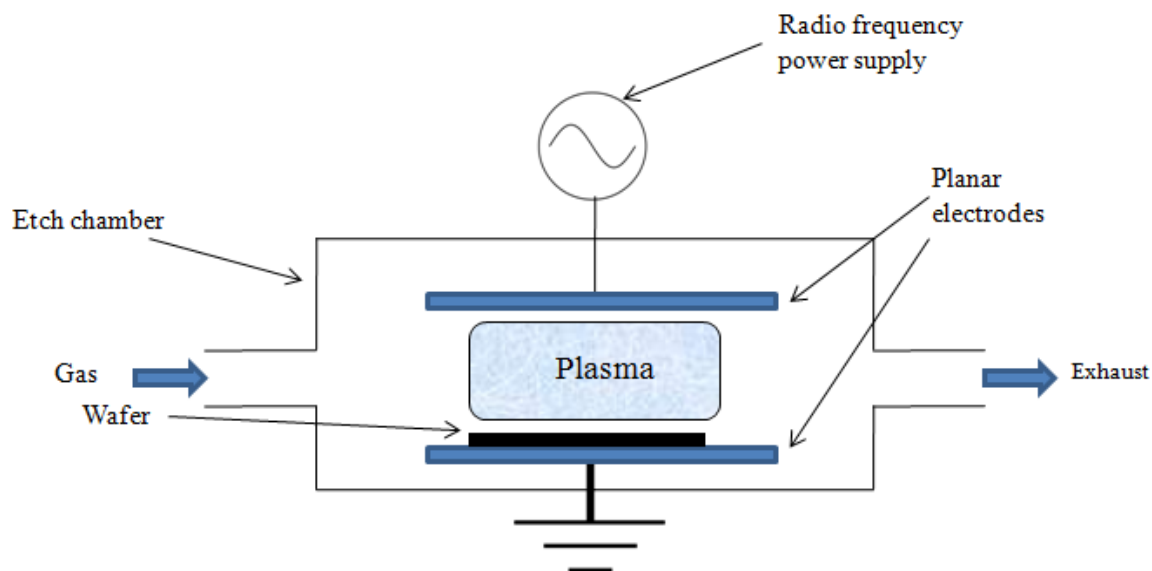


Fig. 3.10 Schematic diagram of reactive ion etch system [69]

Ultra-Violet Ozone (UVO) Cleaner

UVO treatments, not only can be used to clean surfaces, it can be also used to modify the surface chemistry and improve the wetting characteristics of natural and synthetic polymers [70]. A principal advantage of the UV ozone method is that it can be applied under ambient conditions without the need of a vacuum system, with a very high degree of control, reducing the maintenance cost dramatically. The UVO treatment relies upon the combined effects of UV light and ozone, produced in situ from a gas-phase photo-dissociation of molecular oxygen. The system contains a mercury vapour lamp which emits UV light of major wavelengths 184.9 nm and 253.7 nm [71]. When the atmospheric molecular oxygen (O_2) is exposed to 184.9 nm UV light, oxygen absorbs the ultraviolet rays to form ozone (O_3) and atomic oxygen (O^*) as given in Eq. 3.1. Since atomic oxygen is highly reactive, it breaks the polymer chains by insertion of oxygen containing

functional groups on the polymer surface. In comparison to the plasma systems, UVO cleaners are easy to operate and are relatively in-expensive.



The PS spin coated substrates were exposed to UV ozone treatment in the UV ozone cleaner (Samco UV-1, SAMCO Inc., Kyoto, Japan) at room temperature for 2, 5, 10, 30 and 45 min. Also since the treatment time can be finely tuned, samples were exposed for much shorter durations at 2, 5, 10, 20 and 60 s as well.

3.3.2.4 Contact Angle Measurements

The investigation of the contact angle of water with a surface is one of the common ways to measure the wettability (hydrophilicity) of the surface. The contact angle formed between a droplet and a solid surface is a result of the equilibrium between three surface tensions: solid-vapor (γ_{SV}), liquid-vapor (γ_{LV}) and solid-liquid (γ_{SL}) as illustrated in Fig. 3.11a. The equilibrium contact angle (θ) is given by the Young Dupre equation (Eq. 3.2):

$$\cos\theta = \frac{\gamma_{SV} - \gamma_{SL}}{\gamma_{LV}} \quad \text{.....Eq. 3.2}$$

If the surface is hydrophilic (wetting), the water will spread out on the surface, reducing the contact angle. As illustrated in Fig. 3.7, contact angle between 0° and 90° means that the surface is wettable and above 90° means it is not wettable [72].

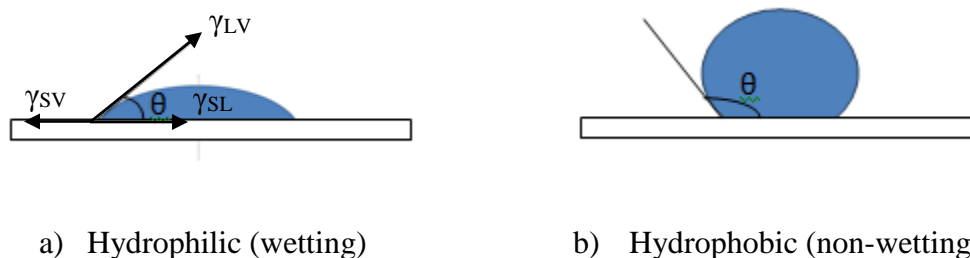


Fig. 3.11 Illustration of contact angles of a) hydrophilic and b) hydrophobic surface

A contact angle goniometer is an instrument, which can be used to measure the contact angle formed between the solid and the liquid drop. The equipment consists of a horizontal stage to mount a solid or liquid sample, a micrometer pipette to form a liquid drop, an illumination source, and a telescope equipped with a protractor eyepiece as shown in Fig. 3. 12. Samples were placed on the horizontal stage of the Rame-Hart, Model 200 Goniometer (Rame-Hart Co. NJ, USA) and a drop of DI water was pipetted on the surface using the micro syringe above it. Then the sample was illuminated, the optimum brightness adjusted, the telescope and the camera were used to magnify and capture the image of the drop. Next, the contact angle measurement was performed by simply aligning the tangent of the water drop profile at the contact point with the surface by hand and the contact angle was analysed by using the software. Three measurements at different locations on the surfaces were recorded to confirm the uniformity of each sample. Therefore, the surface modification due to the oxygen plasma or UV ozone treatment can be investigated systematically by contact angle measurements.

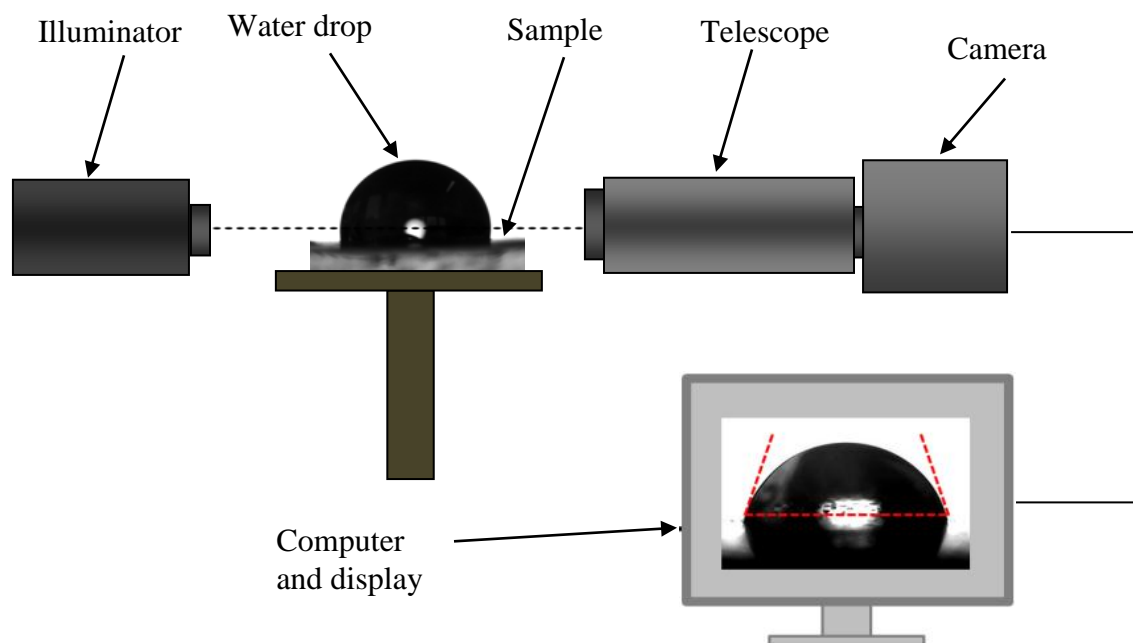


Fig. 3.12 Schematic of an experimental setup capturing the image of the drop [73]

3.3.2.5 Octadecyltrichlorosilane (OTS) Silanization of the Chamber

In order to carry out the OMCVD process as economically as possible – the precursor is expensive to synthesize - it is necessary to make sure that the AuNPs nucleate on the samples only and do not grow on the inner walls of the OMCVD reaction chamber. If the nucleation and growth is not chemically hindered on the inner walls, less gold precursor only will be available for the substrates, yielding fewer NPs on the samples or necessitate enhanced growth times and enhanced amounts of precursor. In order to keep the OMCVD process as efficient as possible the inner walls of the reaction chamber must be non-growth surfaces for the precursor. This can be achieved by creating $-\text{CH}_3$ terminated groups on the inner surface of the chamber, using octadecyltrichlorosilane (OTS, Fig.3.9) [74]. OTS is a molecule which forms a silane network on $-\text{OH}$ terminated surfaces and exposes $-\text{CH}_3$ groups, converting the surface to hydrophobic. Although the nature of the interaction of OTS with hydroxylic substrates remains unclear, a three-step process given

in Fig. 3.13 is a commonly accepted mechanism [75, 76]. Initially the hydrolysis of the chloro moieties of OTS at the hydroxylic (-OH functionalized) substrate surface occurs to generate a silanetriol. Then the silanetriol physisorbs onto the functionalized substrate via covalent bonding with the removal of water molecule and ultimately forms both $\text{Si}_{\text{substrate}}\text{-O-Si}_{\text{silane}}$ and $\text{Si}_{\text{silane}}\text{-O-Si}_{\text{silane}}$ cross-linking types of covalent bonds.

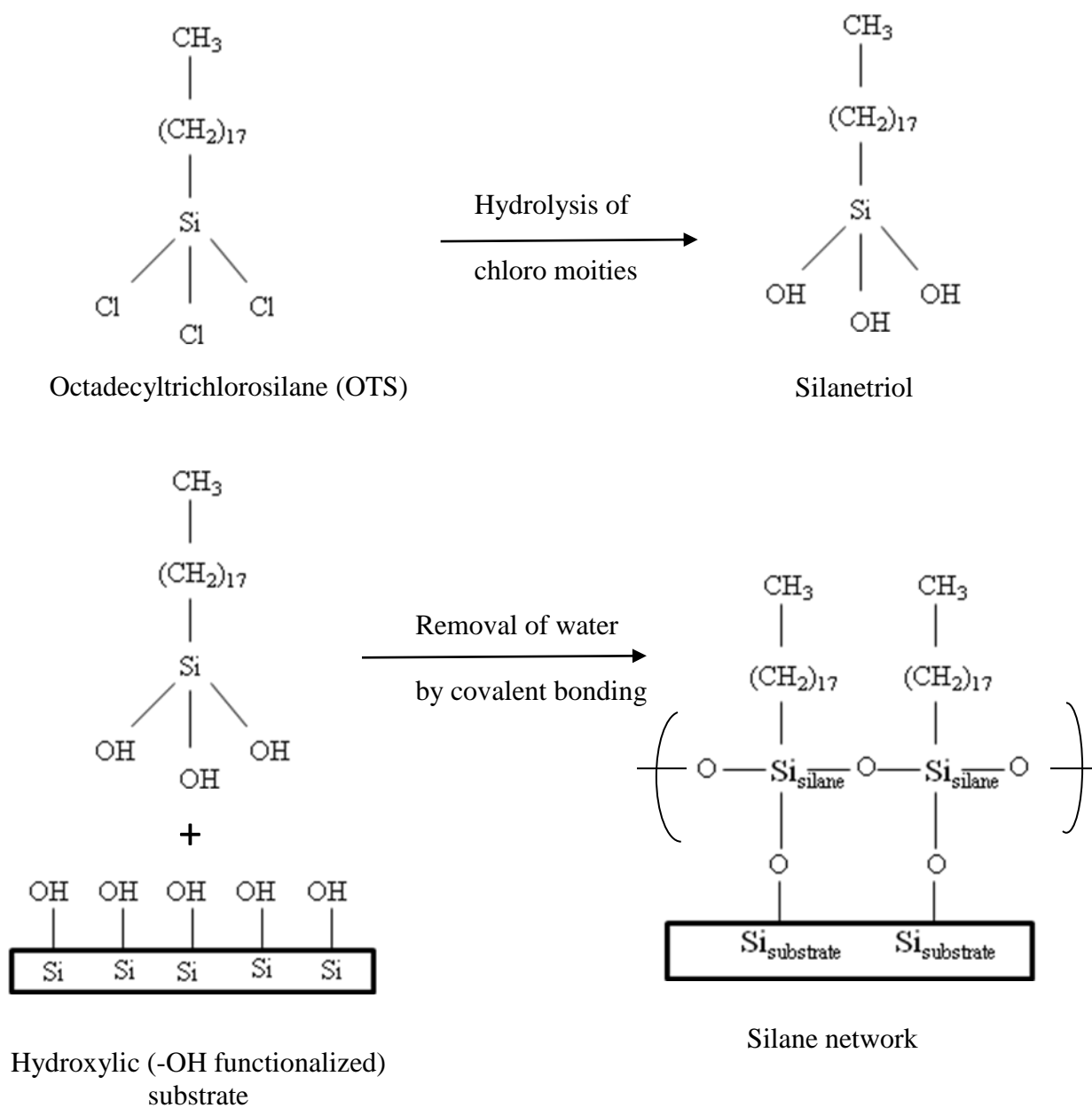


Fig. 3.13 Silanization of silicon substrates with octadecyltrichlorosilane (OTS)

Therefore, the inner surface of the OMCVD glass reactor (Fig. 3.14) was functionalized wet chemically with OTS by using the procedure described below.

In order to produce $-OH$ groups on the inner glass surface of the OMCVD chamber, it was filled with freshly prepared piranha solution (1:3 v:v $H_2O_2:H_2SO_4$) and kept for three hours. After piranha treatment, the chamber was rinsed with abundant amounts of DI water and then dried in an oven. Then, the reactor was filled with 1:500 (v/v) OTS (Sigma Aldrich, assay $\geq 90\%$): toluene (Caledon Laboratories Ltd., Ontario, Canada, assay $\geq 99.5\%$) solution in a nitrogen environment inside a glove box overnight [77]. The nitrogen environment is crucial to avoid polymerization of the silanes when oxygen and/or water are present. Following the OTS functionalization, the reactor was rinsed with toluene and placed in a vacuum oven for 20 min to expel toluene from the reactor surface.

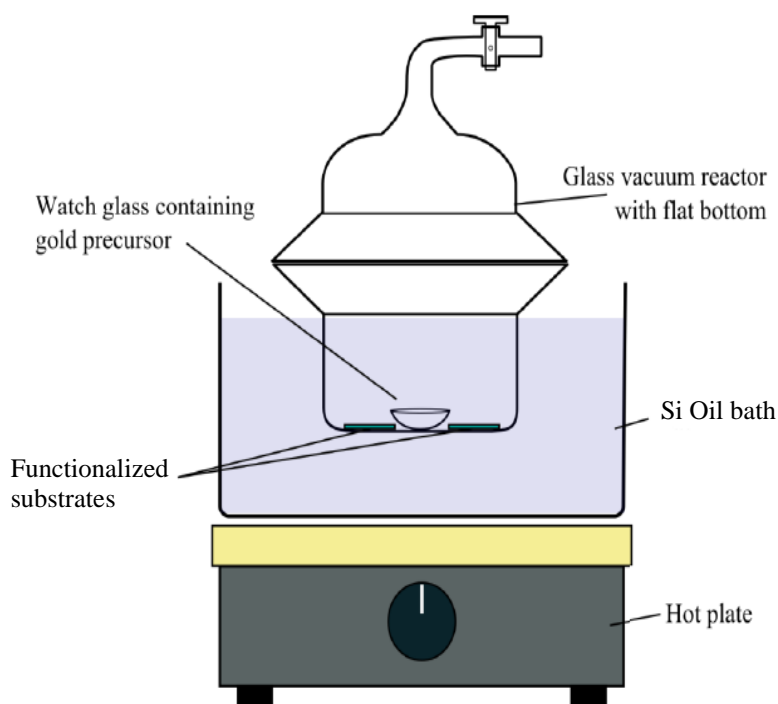


Fig. 3.14 Scheme of the OMCVD setup (Erden et.al, Chem. Vap. Deposition 2013, 19, 338 – 346)

3.3.2.6 OMCVD Process

Initially, the non-active side of the samples were covered with Scotch tape (3M, Canada) to avoid physisorption or chemisorption of AuNPs to this surface. For the OMCVD process, the OH-functionalized PS samples and 20 mg of the gold precursor in a watch glass were placed on the flat bottom inside the chamber and the chamber was sealed tightly. Then the chamber was evacuated to 6 Pa using a vacuum pump, the valve closed, the pump removed and was then positioned in a silicone oil (Sigma Aldrich, Canada) bath kept at 77° C for 17 min. The silicone oil helps to reach the desired temperature in the OMCVD chamber and to maintain this temperature uniformly across the flat chamber bottom where the samples are located. It's essential to keep the chamber as horizontal as possible within the oil bath, so that the bottom flat surface of the chamber and the samples inside get evenly heated providing a homogeneous AuNP growth. The low vacuum and heating allows the precursor to decompose, and the Au to nucleate. After nucleation, AuNP growth starts and continues until the precursor is used up. After AuNP growth, the reactor was allowed to cool and then was immediately vented with air. Finally, the samples were removed from the chamber and were characterized with a UV-Vis absorption spectrometer and a scanning electron microscope as described in Chapter 4.

Chapter 4

4.0 Characterization

4.1 Overview

The details of the methods used to find the optimum duration of creating -OH groups on PS using XPS analysis, characterizing and observing the morphology of the OMCVD grown AuNPs using UV-Vis absorption spectroscopy and scanning electron microscopy (SEM) respectively are discussed. It will be followed by sensing experiments on the grown AuNPs.

4.2 X-Ray Photoelectron Spectroscopy (XPS)

4.2.1 Principles

X-ray photoelectron spectroscopy (XPS) is an analytical surface-sensitive technique that measures the elemental composition, chemical state and empirical formula of a material. The phenomenon is based on the photoelectric effect outlined by Einstein in 1905, which is the ejection of electrons from a surface of a material when light (photon) shines upon it. XPS involves irradiating a sample with X-rays of a characteristic energy and simultaneously measuring the kinetic energy and flux of electrons that escape from the surface (1 – 10 nm) of the material being analyzed. These electrons are ejected from the

core levels ($1s$, $2s$, $2p$ etc.) of an atom as illustrated in the scheme of photoemission process in Fig. 4.1

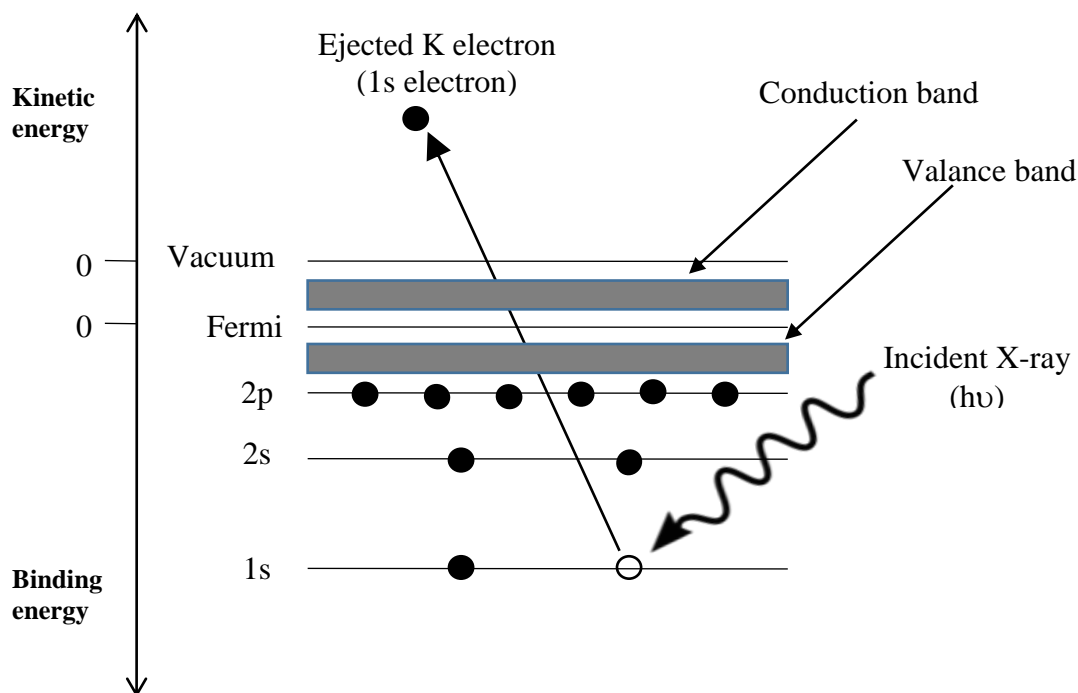


Fig 4.1 Scheme of photoemission process at a sample surface in XPS surface analysis.

The energy difference between the two zeroes in the figure represents the work function of the sample.

When a solid absorbs a photon (X-ray) with energy in excess of the binding energy of an electron, a photoelectron is emitted. The kinetic energy of the emitted photoelectron (K.E.) is related to the binding energy (B.E.) of the electron referenced to the vacuum level by the Einstein equation [78] given in Eq. 4.1:

$$K.E. = h\nu - B.E. \quad (4.1)$$

Where, $h\nu$ is the photon (X-ray) energy.

The binding energy of an electron, is the energy required to remove the electron from the surface and which is equal to the difference in energies between the atom with 'n' electrons (initial state) and the ion with '(n - 1)' electrons (final state) as shown in Eq. 4.2:

$$B.E.(k) = E_f(n-1) - E_i(n) \quad (4.2)$$

The kinetic energy of these photo emitted core electrons is a function of its binding energy and is characteristic of the electronic structure (1s, 2s, 2p etc.) of atoms from which the photo generation was emitted. Therefore, by measuring the kinetic energy of the emitted electrons, it is possible to determine the energy distribution of electronic states of the atomic elements present in the solid surface.

4.2.2 Instrumentation

The sample is placed in an ultrahigh vacuum environment and exposed to a low-energy, monochromatic X-ray source such as Al K α (1486.6 eV) or Mg K α (1253.6 eV). These incident X-rays cause the ejection of core-level electrons from sample atoms. Once the photoelectrons are ejected from the sample, they are collected by a series of focusing lenses, and then separated according to their kinetic energy in a hemispherical analyzer.

A survey spectrum is recorded by counting the number of ejected electrons over a range of electron kinetic energies detected. That is, it gives the variation between the intensity (number of electrons) with the kinetic energy of the detected electrons. Since XPS is a quantitative technique, the number of detected electrons in each of the

characteristic peaks is directly related to the amount of element within the sampling volume and represents the atomic concentrations. Each element produces a characteristic set of XPS peaks at characteristic binding (kinetic) energy that directly identify each element that exists on the surface of the material being analyzed. These characteristic spectral peaks correspond to distribution of electrons within the atoms or core level orbitals.

4.2.3 Data Analysis

In order to test the hypothesis on increasing numbers of -OH nucleation sites on the PS surface with increasing the oxygen and UV ozone treatment time and to find the optimum duration of the treatment time, XPS (Kratos AXIS Ultra spectrometer with a monochromatic Al K α X-ray operating at 140 W) analysis was performed. For all samples, a survey run with a pass energy of 192 eV, from 0 to 1000 eV on the binding energy scale in steps of 700 meV was performed for a duration of 5 min. The PS spin coated samples were treated with both oxygen plasma and UV ozone for the same durations (0, 2, 5, 10, 30 and 45 min) and the oxygen concentrations of these samples were compared using the survey spectra. Since the UV ozone treatment time can be tuned finely, XPS data were obtained within the first 1 min at 2, 5, 10, 20 and 60 s as well. To monitor the oxide composition, high-resolution XPS was employed on the C 1s and O 1s regions. This gives the information on the chemical state and bonding of those elements which were not resolved in the survey spectrum. In a high resolution XPS analysis, an x-ray energy distribution with reduced energy width is used which improves the chemical selectivity by narrowing the spectral peaks and increasing the sensitivity. These

measurements and the data fitting were performed by Mark C. Biesinger, Surface Science Western, University of Western Ontario [79].

4.3 UV-Visible Spectrometer

4.3.1 Principles

UV-visible absorption spectroscopy is a technique used to measure the light that is absorbed due to its interaction with a sample, as a function of frequency or wavelength [80]. In its simplest form, a sample is placed between a light source and a photo detector, and the intensity of light that passes through the sample (I) is detected and compared to the intensity of light before it passes through the sample (I_0) by a photomultiplier or a photodiode. The spectrometer is configured to measure the transmittance (T) usually in percentage (%) or absorbance (A) which is given by equations 4.4 and 4.5 respectively:

$$T = \frac{I}{I_0} \quad (4.4)$$

$$A = -\log_{10}(I/I_0) \quad \text{Or} \quad A = -\log(T) \quad (4.5)$$

4.3.2 Instrumentation

The basic parts of a UV-Vis spectrometer are a light source, a holder for the sample, a diffraction grating in a monochromator (optical device that transmits a mechanically selectable narrow band of wavelengths of light from a wider range of wavelengths available at the input) and a detector. These spectrometers usually contain deuterium and

tungsten lamps to illuminate the sample across the ultraviolet, visible and near infrared regions of the electromagnetic spectrum. A beam of light from a visible and/or UV light source is separated into its component wavelengths by a diffraction grating in the monochromator. Fig. 4.2 illustrates a scheme of double-beam spectrometer, where the incoming beam of light is split into two equal intensity beams by a beam splitter before it reaches the sample. Here, one beam is used as the reference and the other beam passes through the sample and then the intensities of these light beams are measured by detectors and compared. Ultimately a spectrum of the absorption intensity (either as absorbance or transmittance) as a function of wavelength is obtained.

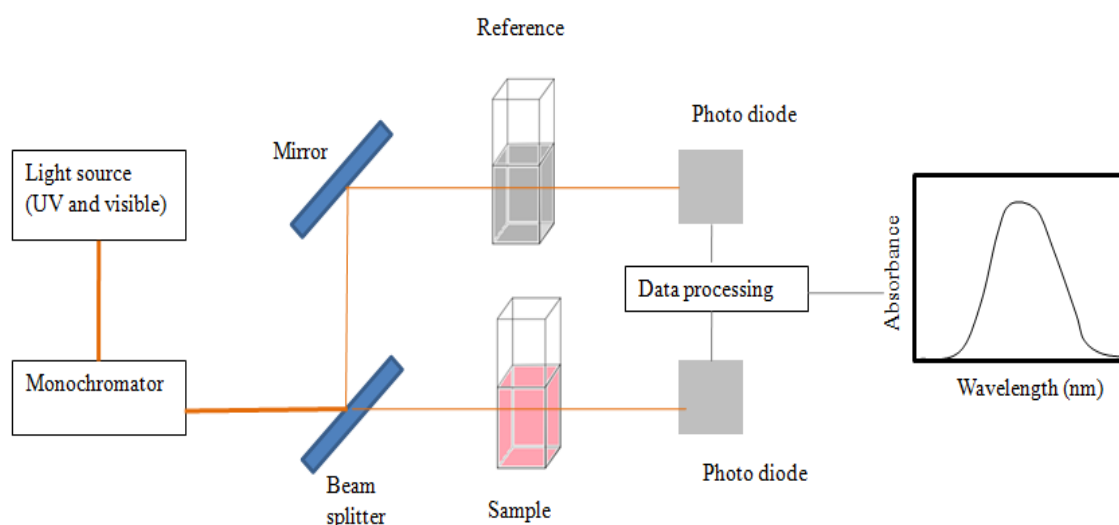


Fig. 4.2 Schematic of double beam UV- visible spectrophotometer

(Modified from: https://upload.wikimedia.org/wikipedia/commons/9/95/Schematic_of_UV-visible_spectrophotometer.png)

4.3.3 Data Analysis

In order to obtain the absorption spectra of the OMCVD grown AuNPs, first the Scotch tape at the back side which was used to prevent nanoparticle growth on the non active (back) side of the sample was removed and then the adhesive glue at this backside was wiped off with an ethanol soaked cloth. Baseline correction was performed before scanning the samples. Next the sample was placed in the sample mount of the Lambda 850 UV-Vis spectrophotometer (Perkin Elmer, CA, USA). Then the sample was scanned between 500 – 800 nm in steps of 2 nm, with a plain PS spin coated glass sample as its reference, placed in the reference mount. The absorption spectra of OMCVD grown samples functionalized with different treatment times were obtained to check the shifts in the peak wavelength with treatment time.

Also, since the sensitivity of the AuNPs depends on the width of the absorption spectra, the full width at half maximum (FWHM) of each absorption spectrum of the grown AuNPs was calculated. Further, to ensure that the AuNPs are strongly attached to the surface and to make the process reproducible, the OMCVD grown samples were repeatedly rinsed in anhydrous ethanol and the absorption spectra were obtained afterwards.

4.4 Scanning Electron Microscope (SEM)

4.4.1 Introduction

A SEM produces images of a surface of a sample by scanning with a focused beam of electrons instead of a beam of light. Since electrons have a much smaller wavelength than visible light, SEM provides images with a much higher resolution than optical microscopes. Although electrons provide highly resolved images, they cannot freely travel through air because there are enough molecules in air to easily absorb these electrons. Therefore, the path in which the electrons will travel should be kept under vacuum, making the instrument expensive.

4.4.2 Instrumentation

The basic principle is that a beam of concentrated electrons is generated by an electron gun located at the top of the device and accelerated through a high voltage as depicted in Fig. 4.3. The speed of the electrons emitted from this gun can be controlled by the potential (accelerating voltage) applied. The electrons from the gun come out in almost a spray pattern, so a series of lenses within a vacuum chamber is necessary to control the flow of electrons and to direct the electrons towards the specimen. The lenses are made with ferromagnetic materials and windings of copper wire. Therefore, they can produce a focal length, which can be changed by varying the current through the coil. The electrons will bend due to the magnetic field and follow a helical path, spiraling down the column. Finally, these electrons interact with atoms in the sample and emit backscattered electrons or secondary electrons. When the high energy incident electron beam knocks out an

electron from the sample atom's shell, it undergoes additional scattering events while traveling through the specimen. Therefore, it loses its energy and has much less energy and therefore it's called a secondary electron. Also, since the electron beam is composed of highly energized electrons, it can collide with a nucleus of the sample atom and bounce back out of the sample. This is called a backscattered electron. These electrons produce various signals that contain information about the sample's surface topography and composition. Mostly SEM uses secondary electrons to image, where the secondary electrons are emitted from very close to the specimen surface leading to high resolution (~ 1 nm) images of sample surfaces.

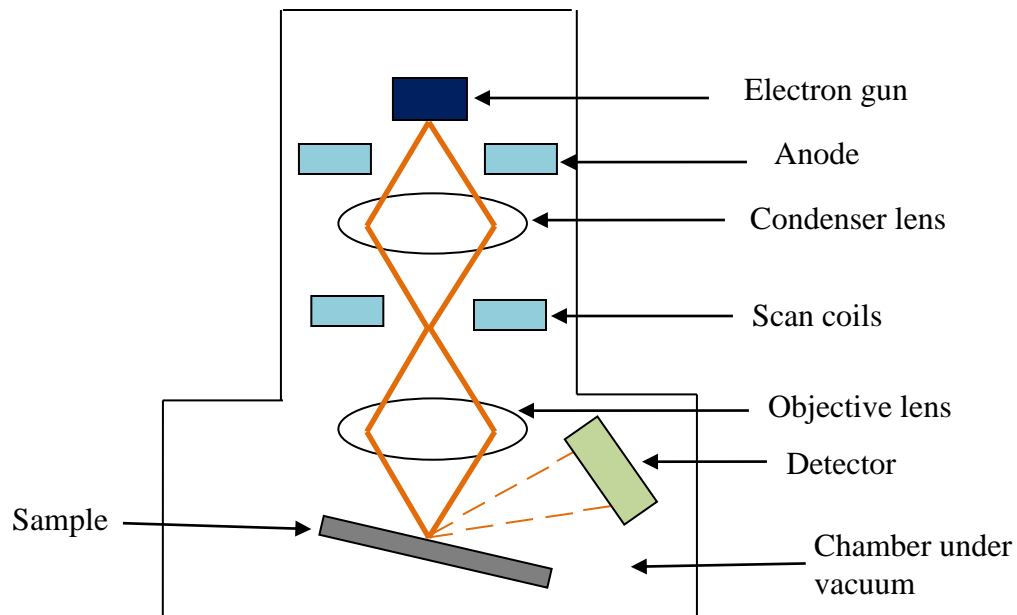


Fig. 4.3 Schematic of scanning electron microscope

4.4.3 Imaging

The morphology of the 17 min OMCVD (6 Pa and at 77 °C) grown AuNPs on 2 min UV ozone treated PS sample was visualized by Scanning Electron Microscopy (LEO 1540XB Electron Microscope, Zeiss, Germany). Since the sample must be conductive at the surface to avoid negative charging of the sample and a buildup of Coulomb repulsion during microscopy, an ultrathin coating of around 1 nm of osmium was deposited onto the sample, prior to imaging.

4.5 Sensing Experiments

Before performing any sensing experiments, it is critical to ensure the stability of the particles used in biosensor applications, to eliminate false positive signals. Therefore, each step in the sample preparation should be performed carefully to ensure the quality of the self-assembly with chemisorption between the substrate and AuNPs. If they are not strongly attached to the substrate by chemical bonding, they can aggregate on the surface or detach from the surface when solution is present.

The stability of the AuNPs was tested by repeatedly rinsing the samples in anhydrous ethanol and obtaining absorption spectra afterwards. Then the bulk-sensing and bio-sensing experiments were performed for the ethanol rinsed stable AuNP samples.

4.5.1 Bulk-Sensing

The bulk AuNP sensitivity can be determined by systematically changing the refractive index of the environment, for example, by changing the ambient solvent. Immersing the sample in organic solvents with different refractive indices changes the LSPR frequency. Therefore, a 20 min OMCVD grown AuNPs on 2 min UV ozone treated PS sample was first immersed in a cuvette (transparent cell made of high quality fused silica or quartz glass to allow UV, visible and near infrared region light to pass) which was filled with methanol of refractive index 1.3284 and the absorption spectra was obtained by using a PS spin coated sample immersed in an identical cuvette containing the same solvent (methanol) as a reference. Then the same procedure was followed by immersing the same sample in isopropanol, and then in dimethylsulfoxide with refractive indices 1.3772 and 1.4793, respectively and analyzing the resonance shifts in peak wavelength of the absorption spectra. It should be noted that the sample should be immersed in solvents with refractive indices in the increasing manner. Then the graph of peak spectral position versus refractive index of the solvents was plotted to obtain the sensitivity or which is called as the figure of merit (FoM) of these nanoparticles from the slope of the graph.

4.5.2 Bio-Sensing

Although bulk-sensing gives an overall idea of sensing abilities of the AuNPs, a more precise way to evaluate the bio-sensing ability is necessary. Therefore, a well-known biological guest-host binding system with a very large binding constant can be used to evaluate the sensitivity. The biotin-streptavidin system was implemented detecting the binding of the protein to the immobilized biotin for judging on the sensing capabilities of

a sensor. Binding of biotin to streptavidin is one of the strongest, stable and irreversible non-covalent interactions known in nature. Streptavidin is a large protein (50,000 Dalton) which has four binding sites for biotin. Biotin is relatively small (244.3 Daltons), and conjugates to one of the four binding sites of streptavidin shown schematically in Fig. 4.4.

Due to the geometrical structure of streptavidin, we need to functionalize the AuNP surfaces by mixed, diluted thiolated biotin solution, ensuring that in the resulting SAM, the biotin is exposed above the surface of the SAM to allow streptavidin to bind to it. This was ensured by diluting the biotin solution with hydroxyl terminated thiols which also avoid unspecific binding [81]. 200 μ l of 0.05 mM 11-mercaptoundecanol (Assay – 97 %, Sigma-Aldrich, Ontario, Canada) and 200 μ l of 0.05 mM of biotinylated thiol (MW – 646.95, NanoScience Chemicals, Phoenix, AZ, USA) solutions were separately prepared in ethanol anhydrous solution. Then the hydroxyl terminated and biotinylated thiols were mixed to form a combined solution with a concentration of 9:1. A 20 min OMCVD grown AuNP sample was immersed in this solution for two hours to form a SAM with biotin moieties [82]. This biotin modified sample was repeatedly washed with ethanol to remove unbound molecules and blown dry with nitrogen. Different concentrations of streptavidin (Rockland antibodies and assays, Limerick, PA, USA) from 0.00001 mg/ml to 0.1 mg/ml in Dulbecco's Phosphate Buffered Saline - DPBS (without calcium chloride and magnesium chloride and with a pH between 7.0 – 7.3) were prepared. A buffer is a solution which consists of a mixture of weak acid and its conjugate and maintains the pH of the solution even upon addition of acidic or basic components. After that, the samples were immersed in PBS buffer and then in increasing concentrations of streptavidin. The absorption spectra of the AuNP sample at each

streptavidin concentration were obtained with the sample being exposed to the respective solution. Here, a PS sample which was immersed in a cuvette filled with PBS solution, was used as the reference at each measurement. To check the sensing ability of the grown AuNPs, the variation of peak wavelength versus streptavidin concentration was plotted.

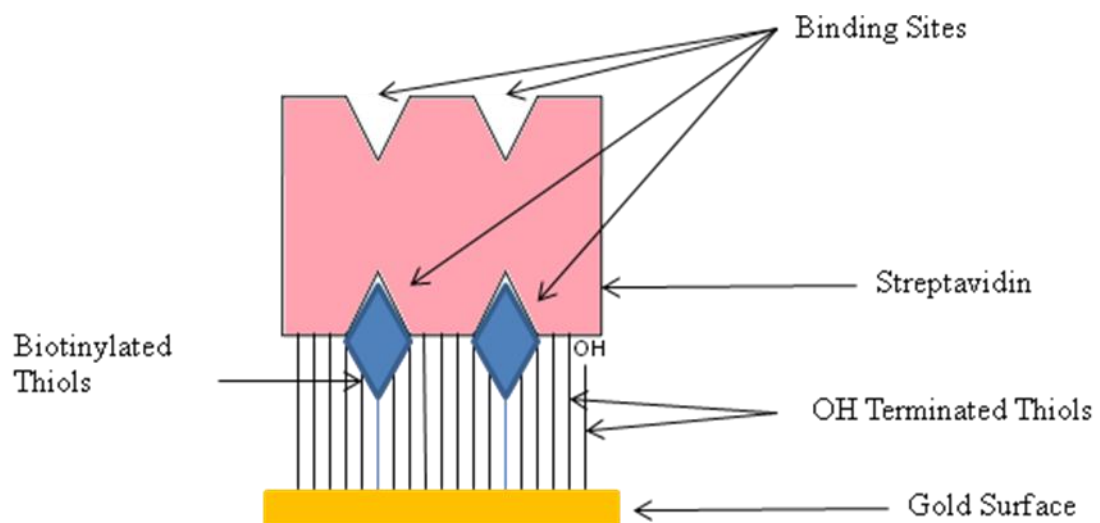


Fig. 4.4 Scheme of the final assembly of streptavidin on a biotinylated SAM

Chapter 5

5.0 Experimental Results and Discussion

5.1 Overview

In this chapter the results obtained using the procedures described in chapter 3 to grow AuNPs on different polymers are presented. Initially the results of attempts on the growth of AuNPs on few transparent polymers bearing amino groups are discussed. Then, the absorption spectra (LSPR spectra) of the OMCVD AuNPs on surface-oxygen enhanced PS, variation of the peak wavelengths and FWHM with treatment times are discussed. Also, scanning electron microscopy (SEM) results of the grown AuNPs are depicted. Further, XPS data on the oxygen concentration of the PS spin coated surfaces are analyzed. It will be followed by the outcomes on bulk-sensing and bio-sensing abilities of these nanoparticles.

5.2 OMCVD Directly on Amine-Bearing Polymers

The results of the attempts to grow AuNPs directly using OMCVD process on transparent polymers Trogamid®, nylon 6, 10 and polyacrylamide which contain amine groups are discussed in this section.

5.2.1 Trogamid®

The absorption spectra for the wavelength range from 500 to 800 nm for Trogamid® spin coated on cleaned glass substrates with different spin speeds is given in Fig. 5.1a. The spectra after the OMCVD process on these spin coated samples for 17 min at 77 °C and 6 Pa are depicted in Fig. 5.1b.

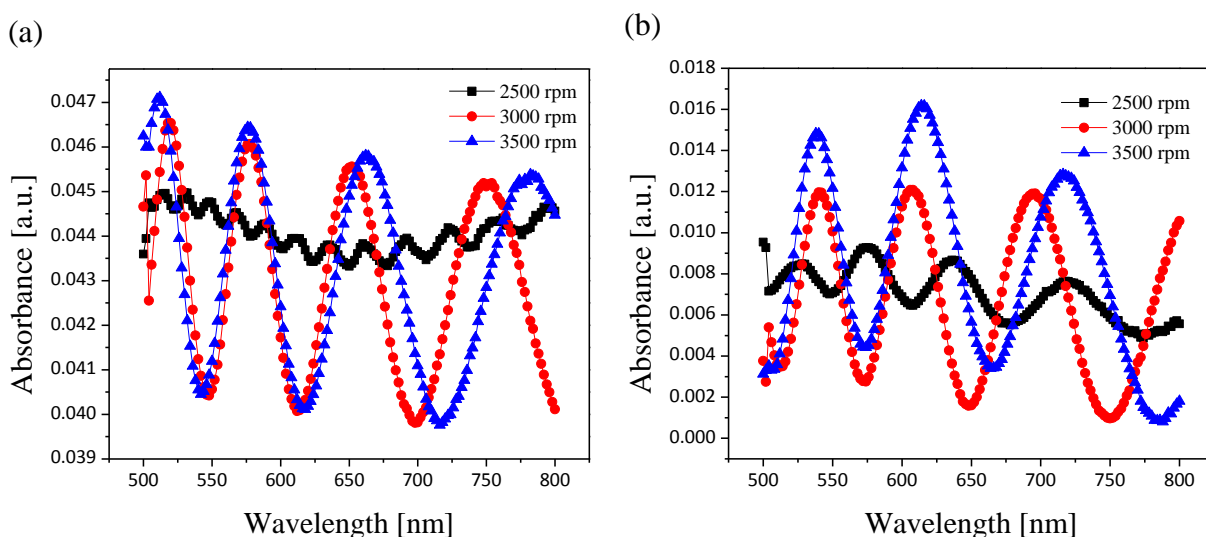


Fig. 5.1 Absorption spectra of Trogamid®: a) as spin coated and b) after OMCVD (17 min, 77 °C, 6 Pa)

There was no appearance of an LSPR peak after the OMCVD process as shown in Fig 5.1a and 5.1b, indicating that no AuNPs were formed on Trogamid®. Only thin film interference pattern was observed. Thin film interference occurs when light is reflected from two parallel surfaces, that is, by the upper and lower boundaries of a thin film, interfere constructively and destructively. The resulting absorption spectrum then has a sinusoidal pattern of interference as shown in Fig. 5.1a and 5.1b.

The height of these interference fringes are almost ten times smaller when compared to an expected signal from gold [83]. When the speed of the spin coating is increased, the thickness of the film reduces. Since the interference pattern depends on the thickness of the films, a slight shift and a small difference in the heights of the patterns (which should be the same) in the absorbance spectra were visible, might be due to the change in the optical path length.

5.2.2 Nylon 6, 10

Fig. 5.2a and 5.2b show the absorption spectra of nylon 6, 10 spin coated on glass substrates at different spin speeds and after the OMCVD process on these spin coated substrates for 17 minutes at 77 °C and 6 Pa, respectively.

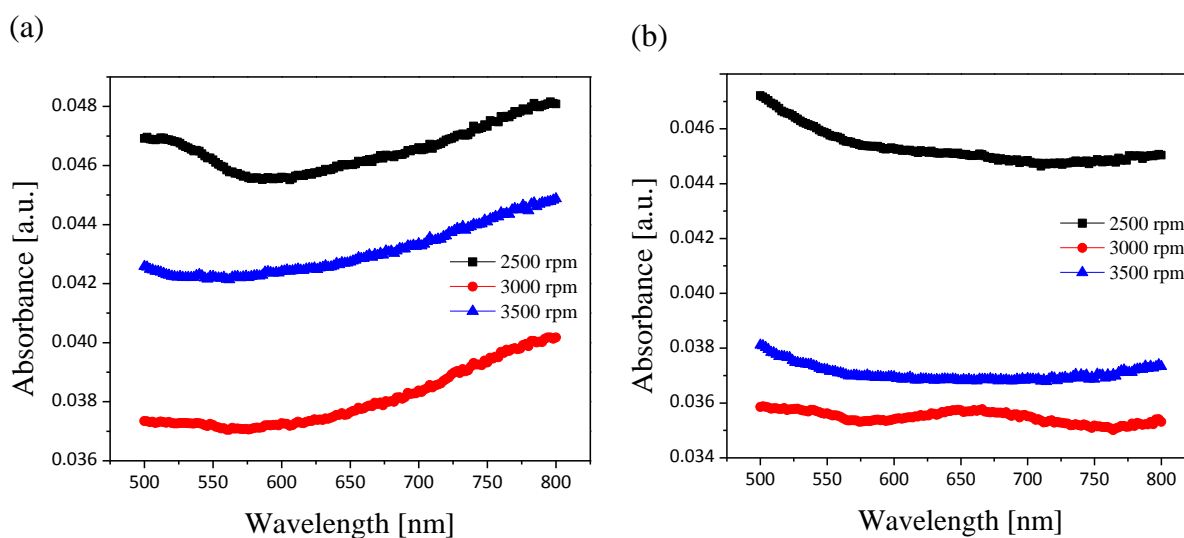


Fig. 5.2 Absorption spectra of nylon 6, 10: a) as spin coated, and b) after OMCVD (17 min, 77 °C, 6 Pa)

There was no LSPR peaks observed in the Fig 5.2b when compared with Fig. 5.2a. Therefore, no AuNPs were deposited on the spin coated nylon 6, 10 surfaces. Also interference fringes were not observed for the Nylon 6, 10 spin coated sample. This might be due to the fact that the film was not smooth or uniform enough in thickness to yield clear interference fringes. In which case moving to another location on the film could have potentially improved the spectrum. The height of the spectra should be almost the same, but since the scale is really small, a minor difference in the heights of the absorption spectra is seen.

5.2.3 Polyacrylamide

Fig. 5.3a and 5.3b show the absorption spectra of polyacrylamide spin coated on glass substrates at different spin speeds and after the OMCVD process on these spin coated substrates for the same parameters as described in section 5.2.2.

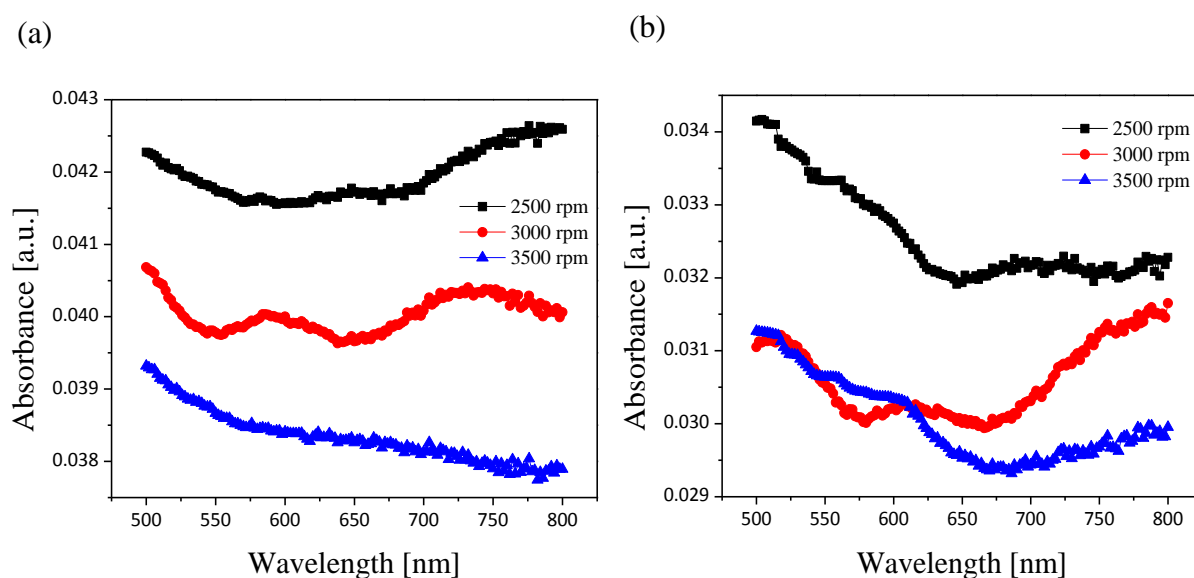


Fig. 5.3 Absorption spectra of polyacrylamide: a) as spin coated, and b) after OMCVD (17 min, 77 °C, 6 Pa)

Similar results as observed for Trogamid® and nylon 6, 10 were obtained for polyacrylamide as well. As mentioned for Trogamid® and Nylon 6, 10 a small variation in the height of the absorbance spectra were obtained which might be due to the noise of the instrument as well.

No LSPR peaks were obtained in either of these amine-bearing polymers. Therefore, the OMCVD process on these amine-containing polymers was unsuccessful. This might be due to the fact that the amine (NH₂) density in these polymers is too low and not exposed to the surface. Also, the nitrogen polar group in the amine groups might not have nucleated the Au from the precursor. Therefore, Au was attempted to grow on an alternative polar group, -OH (hydroxyl group), and the results are described in section 5.3.

5.3 OMCVD on Oxygen Plasma Treated Plain Glass

Fig. 5.4a shows the absorption spectrum of a plain glass substrate within the wavelength regime from 500 to 800 nm. Fig. 5.4b depicts the absorption spectrum of the sample after the OMCVD process (17 min, 77 °C, 6 Pa) performed on the -OH functions prepared by oxygen plasma treatment on the plain glass substrates.

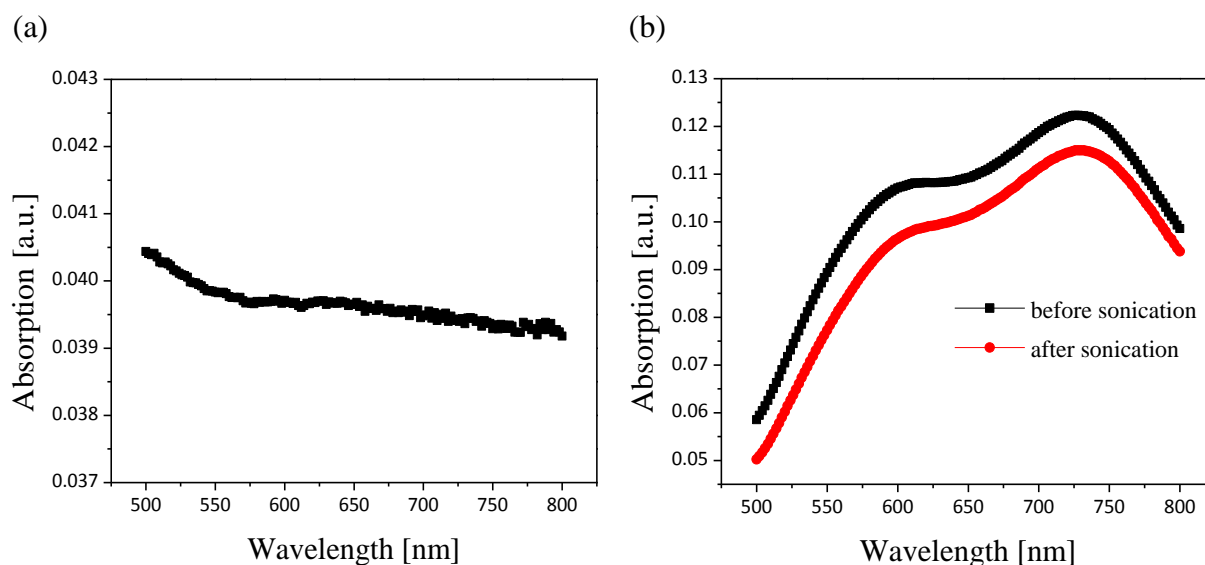


Fig. 5.4 Absorption spectra of a) plain glass, and b) after OMCVD (17 min, 77 °C, 6 Pa) on –OH functionalized glass

Fig. 5.4b shows that a LSPR double peak with $\lambda_{\max,1}$ at ~ 590 nm (single NP LSPR) and $\lambda_{\max,2} \sim 730$ nm (clustered NP LSPR) indicating that AuNPs are formed and starting to cluster to larger aggregates of NPs on the oxygen plasma treated glass surfaces. These peaks remained stable even after sonicating the OMCVD grown AuNP sample for 1 min in ethanol, indicating that the particles are firmly immobilized on the substrate. The second peak at higher wavelength is due to the “cross talk”, which is a result of the overlap of evanescent fields of two or more neighboring NPs when they are closely-spaced [84]. The oxygen plasma had introduced a large number of –OH groups on the glass surface and the polar oxygen group had served as nucleation centers for the growth of AuNPs from the precursor. Because the AuNPs are densely packed, they form clusters resulting in the additional red-shifted peak. Since the growth of AuNPs on –OH groups

was successful, the transparent polymer PS was functionalized with $-OH$ groups and the results of the OMCVD performed on these surfaces are discussed in section 5.4

5.4 AuNP Decorated PS Films

5.4.1 LSPR Spectra of AuNPs

Fig. 5.5 shows the absorption spectra of ethanol-rinsed, OMCVD grown AuNP samples on PS treated at various oxygen plasma treatment times. Here the oxygen plasma treatment was performed on the PS before NP deposition, while the ethanol rinse was done after NP deposition. The OMCVD process was performed identically on all samples at $77\text{ }^{\circ}\text{C}$ and under 6 Pa for 20 min using the procedure described in chapter 3.

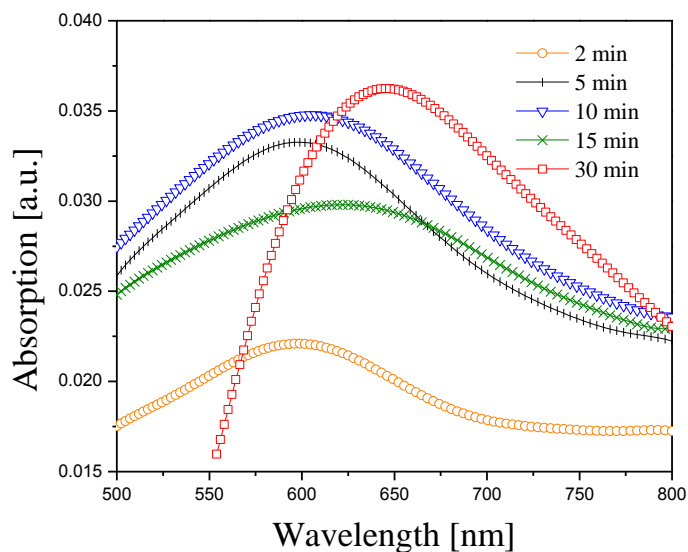


Fig. 5.5 UV-Vis absorption spectra of ethanol-rinsed AuNPs fabricated via 20 min OMCVD ($77\text{ }^{\circ}\text{C}$, 6 Pa) on PS treated over various oxygen plasma times

Clearly broad LSPR peaks were found with λ_{\max} , increasing from 570 to 650 nm (Fig. 5.5). This confirms that the AuNPs are grown on the oxygen plasma treated PS samples when OMCVD process is performed.

Fig. 5.6 depicts the variation of the LSPR peak position λ_{\max} , of the OMCVD grown samples before and after rinsing with ethanol. The raw data of the as grown AuNPs are omitted.

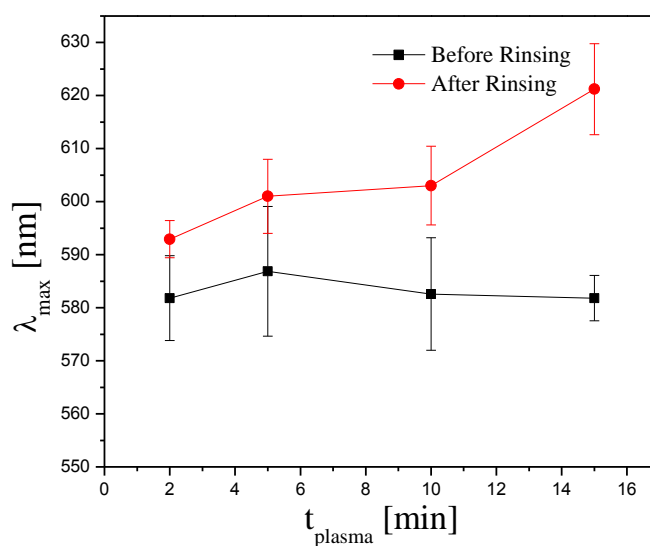


Fig. 5.6 UV-Vis absorption peak position (λ_{\max}) of AuNPs on PS versus oxygen plasma treatment time

The LSPR peaks shifted from ~ 590 to 620 nm (λ_{\max}) with increasing oxygen plasma time from 2 to 15 min for the ethanol rinsed samples (Fig. 5.6). It showed a clear peak shift to higher wavelength, a red-shift, with increasing plasma treatment time. But, the as-prepared samples (before rinsing) show a “stable” peak position at 585 ± 10 nm. We were not able to explain why the as-prepared samples size did not increase with time.

The peak shift of the rinsed samples indicated an increase in the average size of the chemically stable AuNPs with increasing plasma time [85].

Not only is the peak position important in sensing, but also the precision with which the peak position can be determined. This precision is directly related to the peak width, (FWHM). Figure 5.7 shows the FWHM of the LSPR peaks versus plasma treatment duration for 2 to 15 min.

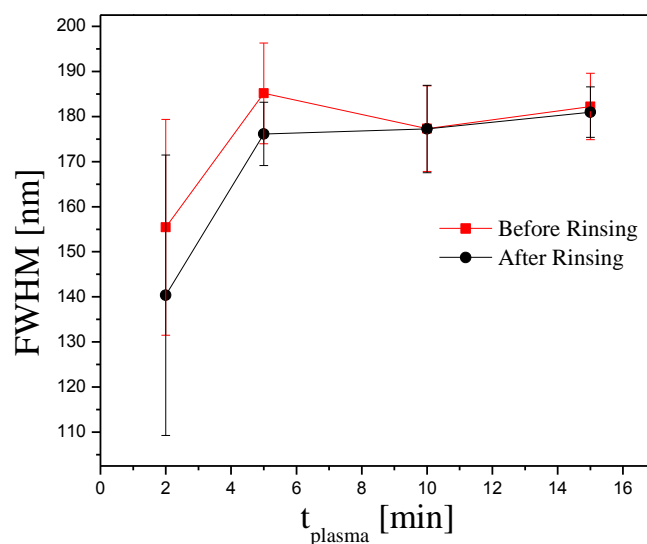


Fig. 5.7 FWHM of LSPR peaks of rinsed and non-rinsed AuNPs on PS versus oxygen plasma time

Within the first 5 min, the FWHM increased with plasma time for both sample sets from 140 ± 31 nm, and 155 ± 24 nm to 185 ± 11 nm, for the before and after rinsing, respectively and then stabilized at 185 ± 7 nm. This shows that as the treatment time increases, the LSPR peak broadens diminishing the high sensitivity of the method.

The position of the LSPR and the FWHM delivered a consistent picture; as the plasma treatment time is increased, existing NPs grew larger and aggregated, increasing the FWHM and shifting the peak position. In addition, newly grown NPs contributed to the peak position at small wavelength and therefore to the width. Rinsing removed loose particles of all kinds; small newly nucleated, larger particles and some NP clusters. The hypothesis is that, with increasing oxygen plasma times, the amount of nucleation sites on the polymer surface increases, allowing for more NPs to grow and also forming larger nanoparticles [86].

Since small FWHM will allow a more precisely LSPR peak position, low plasma treatment durations of the order of 2 min would be suitable to grow AuNPs. Then this should be followed by an extensive rinsing with ethanol to construct a reproducible, strongly attached AuNPs to the substrate and precise sensor platform for biosensing purposes. The same experiments were carried out with UV ozone-treated PS samples. The results were comparable to the oxygen plasma-treated samples.

5.4.2 Scanning Electron Microscopy (SEM)

Fig. 5.8 depicts a SEM image of OMCVD grown AuNPs on 2 min oxygen plasma treated PS to confirm the absorption data on the presence of AuNPs. This image was obtained at a magnification of 50,000 and at a voltage of 20 kV.

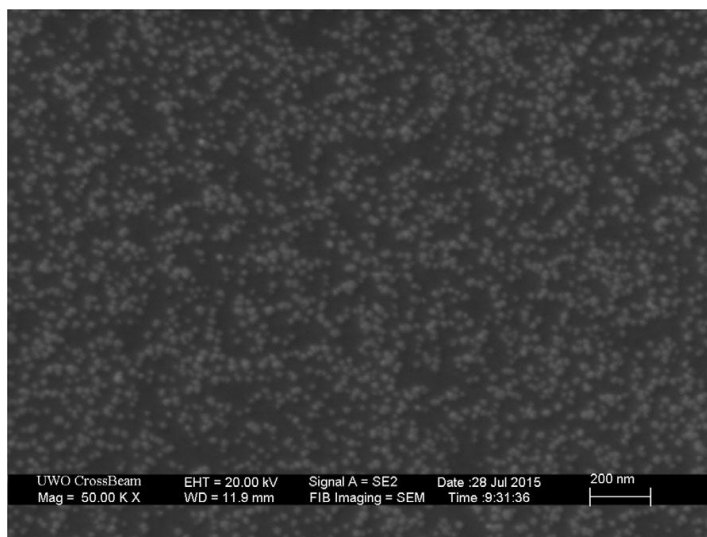


Fig. 5.8 SEM image of AuNPs OMCVD grown on PS (2 min oxygen plasma)

From The SEM image, it was observed that the particles were mostly separated individual round particles. No additional SEM images of the AuNPs with varying OMCVD times were taken, since already detailed description on the shapes and sizes of these particles with increasing OMCVD growth times are found elsewhere [19].

5.4.3 Contact angle measurements

Contact angle measurements are a relatively easy, economical and versatile method for determining the chemical modification undergoing on a solid surface [87]. Therefore, the contact angles of the untreated, oxygen plasma and UV ozone treated PS spin coated samples were measured using the goniometer in which DI water was used as the probe liquid. The contact angle found for the untreated samples was at $\theta = 93.5^\circ \pm 0.9^\circ$, showing the hydrophobic nature of the unmodified PS spin coated sample. But, the contact angle of water for the 2 min plasma-treated and UV ozone-treated samples

dropped below 10° , which is much less than 90° , confirming the hydrophilic nature of 2 min treated samples. After a short exposure to the oxygen plasma or UV ozone, the surface chemistry of PS was significantly altered.

5.4.4 Image of Oxygen Plasma Treated PS Spin Coated Samples

In order to check the optical quality of the PS spin coated samples with varying oxygen plasma treatment duration and to see how the treatment alters the PS surface, optical images of the samples were obtained using a digital camera. Fig. 5.9 shows the PS spin-coated samples treated with increasing oxygen plasma time, from left to right: 0, 5, 10, 30, 45 min which were obtained against a black background.

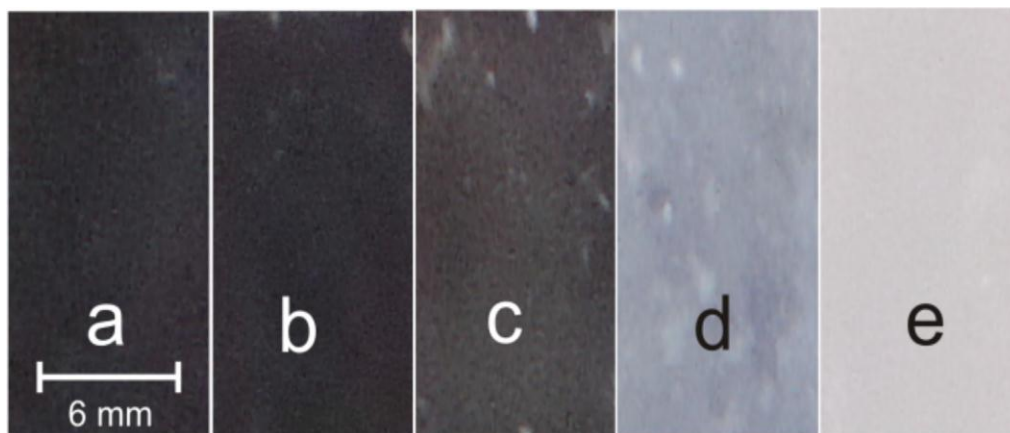


Fig. 5.9 Images of PS spin-coated samples treated with increasing oxygen plasma time against a black background. From left to right: 0, 5, 10, 30, 45 min

The oxygen plasma treatment for longer duration ($t > 30$ min) substantially alters the transparency of the PS thin films. The transparent spin-coated films turn into a milky white coating (Fig. 5.9) which will not be suitable for an absorption spectrum-based bio-

sensing device. Therefore, a plasma treatment of shorter periods less than 5 min only will be suitable for device optical reasons.

Similarly, the ozone plasma treated samples turned to a slightly yellowish color over longer treatment times, which would lead to undesired additional absorption and scattering features in the absorption spectra.

5.4.5 XPS-Results: Oxygen Concentration on Polystyrene Surface

The survey spectrum of XPS shows all the elements present on the sample surface and is usually the starting point of most XPS analysis. This allows to setup subsequent high-resolution XPS spectra acquisition in spectral regimes of interest. Here it will permit to test the hypothesis on an increased number of -OH nucleation sites on the polymer surface with increased oxygen and UV ozone treatment time.

Therefore, the surface composition and functionality of the PS samples before and after oxygen and UV ozone treatments were investigated using XPS survey spectra. Fig. 5.10 shows XPS survey spectra of an untreated PS sample (Fig. 5.10a) and after 2 min of oxygen plasma treatment (Fig. 5.10b) at the same scale. The inset shows a quantification table indicating all elements observed, their binding energies, and their atomic percentages.

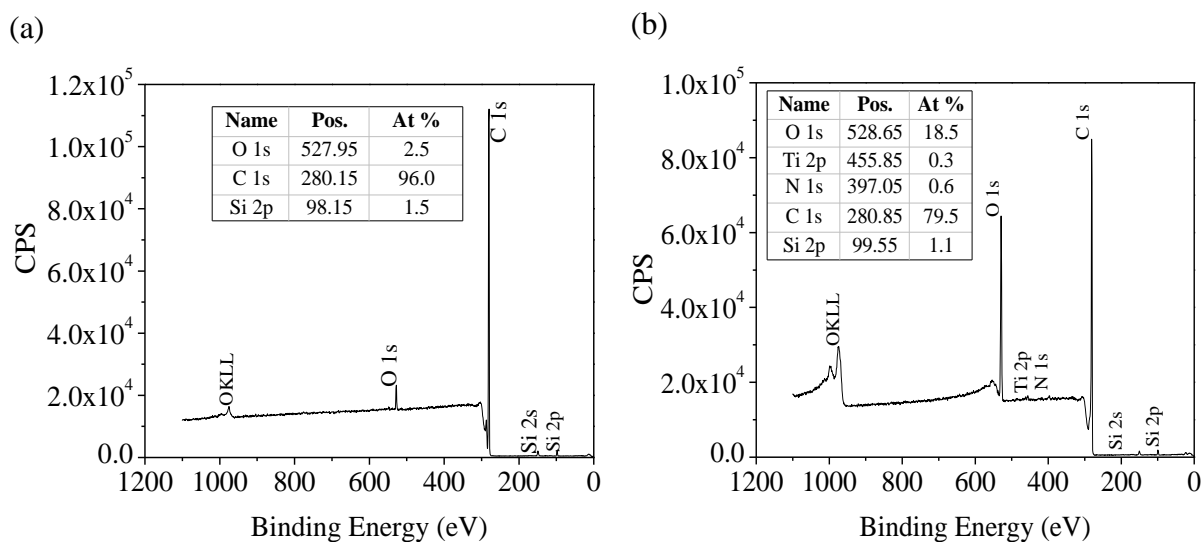


Fig. 5.10 XPS survey spectra of PS spin-coated films; a) untreated, and b) treated at 2 min oxygen plasma

The surface consists primarily of carbon as represented by the tall peak in Fig. 5.10a and b. The elements present at the polymer surface are carbon at 285 eV binding energy and oxygen in both cases, while the small silicon contribution arises from the glass substrate. Also an Auger peak (following core ionization by photoelectron emission an outer shell electron can fill the created vacancy and the energy released can result in the emission of an Auger electron resulting in an Auger peak) is observed at the binding energy of 971.5 eV which is labeled by OKLL in both spectra [88]. The untreated PS exhibit 2.5 at % of oxygen at the surface despite the fact that polystyrene only consists of aromatic (benzene ring) and aliphatic (C-H or H-C-H) carbon as well as hydrogen (which is not detectable by XPS). Impurities are the most probable explanation for the present oxygen contribution on the untreated PS surface. As the corresponding spectrum after oxygen plasma treatment in Fig. 5.10b illustrates, the concentration of oxygen at the

surface increased to 18.5 at %. Exposure to the oxygen plasma has led to the incorporation of oxygen into the PS surface within the first 2 min of plasma treatment and enriching the surface with oxygen.

Fig. 5.11 shows the O 1s peak height versus plasma treatment time for PS samples which were exposed to 0, 2, 5, 10, 30 and 45 min, for both oxygen and UV ozone treatments. Since the UV ozone plasma treatment time can be finely tuned, XPS data were also obtained from 0 - 2 min. These data are depicted in the inset of Fig. 5.11.

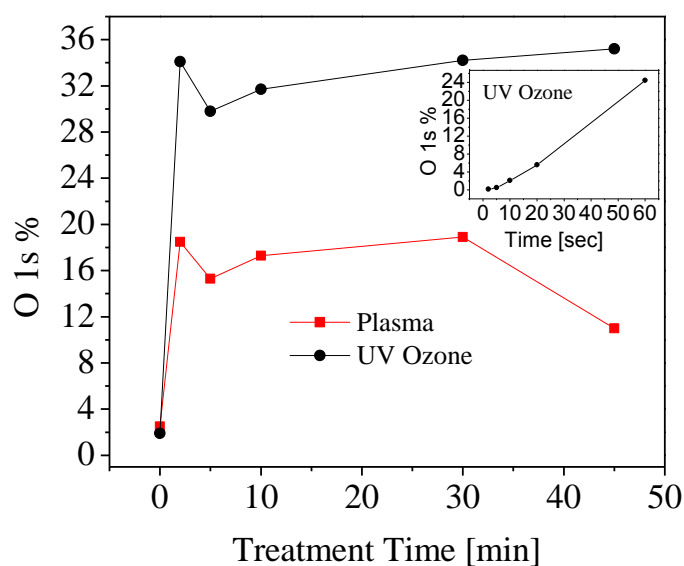


Fig. 5.11 O 1s peak height versus oxygen and UV ozone plasma time. The inset shows the first 60 s for the UV ozone treatment

The amount of oxygen on the PS surface increases rapidly within the first 2 min of plasma treatment for both kinds of plasma, but saturates, depending on the plasma, at ~ 16% for oxygen and at ~ 32% for the ozone plasma (Fig. 5.11). For longer treatment times (45 min), the oxygen level decreased for oxygen plasma treatment. This might be

because the nature of the polymer is being altered, as evident from the optical images of these samples after longer treatment time as well. It was evident that the ozone plasma treatment yielded higher oxygen concentrations than the oxygen plasma treatment for PS spin-coated samples at a given treatment time and therefore providing more nucleation sites for AuNPs to grow. In addition, the timing of the plasma treatment is easier to adjust and therefore the ozone-plasma treatment is the more suitable process to create -OH groups in a controllable fashion on the PS sample for the fabrication of AuNPs.

In order to find out more about the type of the oxygen functional groups presented on the surface of PS and to monitor the oxide composition before and after plasma treatment, high-resolution XPS was employed on the C 1s and O 1s regions.

Fig. 5.12 shows XPS C 1s high-resolution spectrum for untreated and 2 min oxygen plasma-treated PS sample.

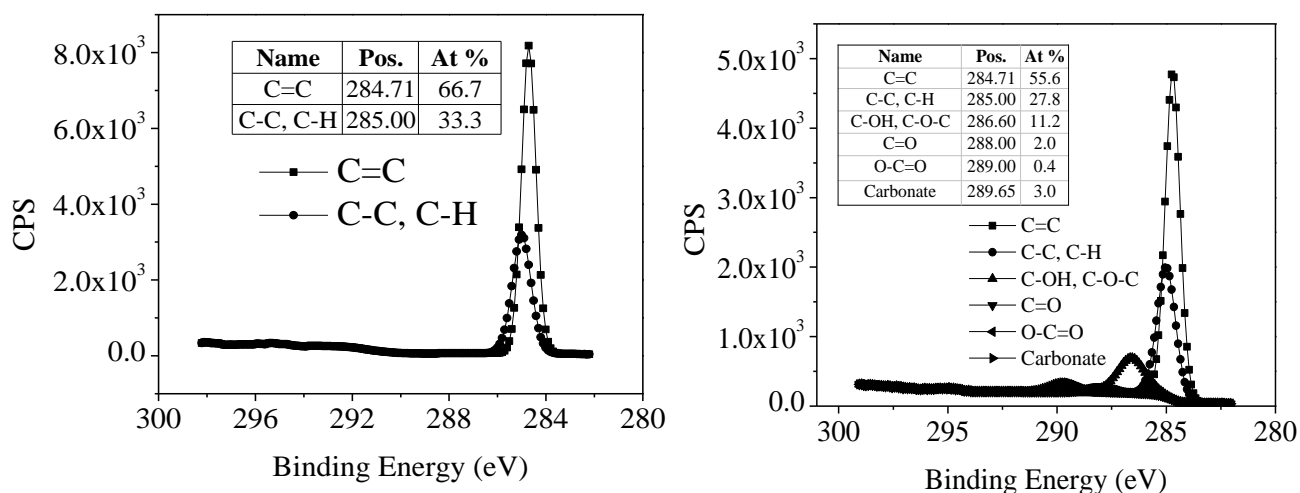


Fig. 5.12 High resolution XPS C 1s spectrum of PS a) before and b) after 2 min exposure to oxygen plasma treatment

Comparing both C 1s spectra presented in Fig.5.12, it reveals that the increased oxidation from the treatment resulted in a wide range of functionalities such as C-O groups at 286.0 eV, carbonyl (C=O) groups at 288.0 eV, ester (O-C=O) groups at 289.0 eV and O-CO=O (carbonate) groups at 289.65 eV [8]. The line fitting of the C 1s showed that almost 68 % of the oxygen was introduced in the form of C-O-H groups.

Figure 5.13 displays XPS O 1s high-resolution spectrum for 2 min oxygen plasma-treated PS sample. The O1s peak is separated into two peaks at binding energies of 532.87 eV and 533.84 eV which can be attributed to C=O, C-O-C and O-C-O, O*-(C=O)-O groups, respectively [89]. Here, since the chemical energy shift between two of the states is sufficiently small, they are been represented by the same binding energy in the O 1s spectra. Therefore, the plasma-treated sample confirms the presence of oxygen in the form of carbonyl, ether and carbonate groups as well. In overall, the XPS technique revealed that there was an appreciable increase in oxygen bearing groups on the PS by the plasma treatment process. However, whether it is the -OH group alone which serves as a nucleation site cannot be proven.

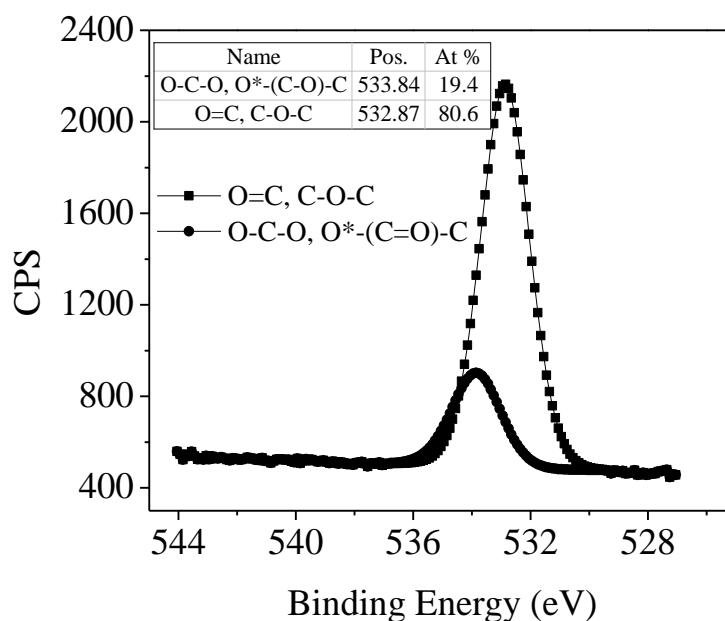


Fig. 5.13 High resolution XPS O 1s spectrum of PS after 2 min exposure to oxygen plasma treatment

In summary, the XPS investigation showed that, with increasing plasma treatment time, beyond 2 min, no additional nucleation sites were created. The LSPR position of the non-rinsed, as grown AuNPs confirmed this behavior. The eradication of the weakly bound Au, however, leads to AuNP populations with increasing diameters as the LSPR shifts to higher wavelength. The hypothesis is indirectly confirmed. A plasma treatment time around 2 min was found to be the optimum to grow OMCVD AuNPs with respect to FWHM and PS “optical quality”.

5.4.6 Bulk Sensing and Figure of Merit

The bulk sensitivity of the immobilized AuNPs to the change in refractive index of the dielectric medium surrounding the AuNPs was monitored by immersing the sample in different solvents. The refractive indices of the solvents marked in Fig. 5.14 are for $\lambda = 589 \text{ nm}$ [90, 91]. The solvents were chosen to ensure that they are bad solvents for PS in order to guarantee no dissolution of the polymer. Fig. 5.14 illustrates the LSPR spectra of the bulk-sensing experiment to determine the Figure of Merit (FoM) for bulk sensing using 2 min of oxygen plasma treated and a 20 min OMCVD grown PS sample.

The OMCVD grown samples can be stored in an airtight container for almost a year. Before sensing experiments are performed on these samples, the absorption spectra of the samples are obtained and compared with the original spectra which were obtained just after the initial preparation of these samples to confirm the presence and stability of these particles.

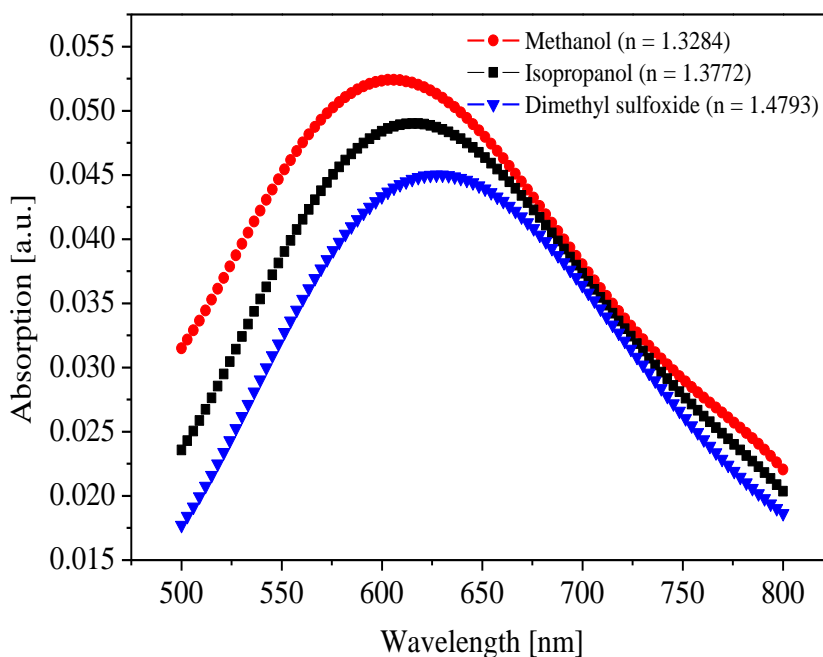


Fig. 5.14 UV-Vis absorption spectra of AuNPs on PS (oxygen plasma time: 2 min) immersed in various solvents exhibiting different refractive indices

The spectral position of the AuNP LSPR peaks (λ_{\max}) immersed in methanol ($n = 1.3284$), isopropanol ($n = 1.3772$), and dimethylsulfoxide ($n = 1.4793$) after curve fitting with a polynomial function were 606.06 nm, 615.15 nm, and 627.27 nm, respectively. The λ_{\max} systematically shifted to longer wavelengths due to change in the dielectric properties with increasing solvent refractive index (RIU) in a linear fashion (Fig.5.15) in this refractive index regime. Particularly this variation is due to change in the refractive index of the surrounding medium around the AuNPs, which changes the resonance condition and the location of LSPR peaks. Once the AuNP substrate is immersed in a high refractive index solution, it polarizes the medium quickly and thus less energy is needed to resonate the AuNPs [92]. Therefore, the LSPR peak red shifts to higher wavelengths as mentioned in chapter 2 (Section 2.2.4).

In order to determine the FoM of the AuNPs fabricated on PS, a graph of LSPR peak wavelength was plotted as a function of the refractive index. Fig. 5.15 illustrates the variation of peak wavelength (λ_{\max}) with refractive index of the immersion solvent. The slope of the linear fit delivers the FoM, which reveals the NP sensitivity (m). This linear relationship is described as $\Delta\lambda_{\max} = mn$, where $\Delta\lambda_{\max}$ is the shift in the LSPR peak position and 'n' is the refractive index of the surrounding medium [93].

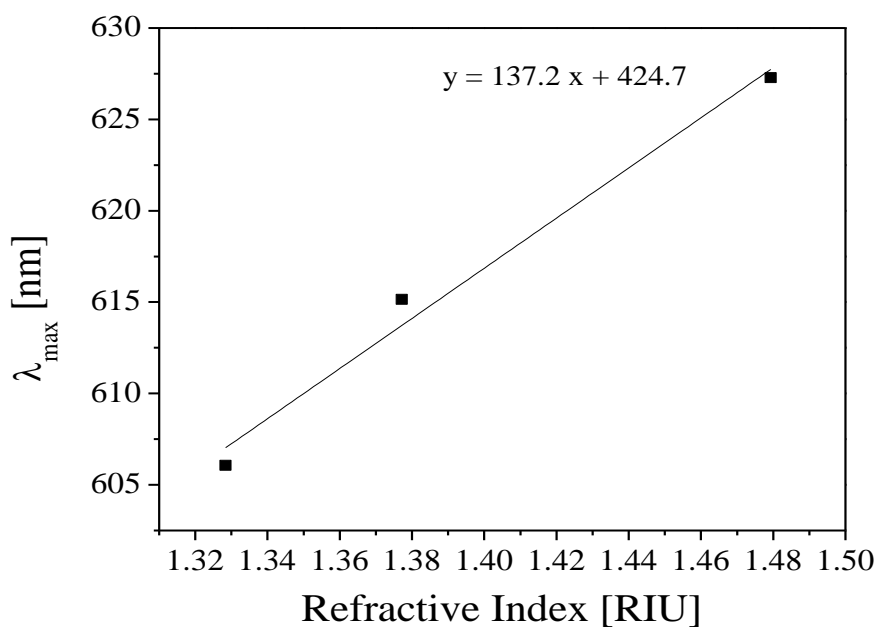


Fig. 5.15 LSPR peak spectral position versus refractive index of the solvents. The slope delivers the FOM for bulk sensing

The FOM for the 20 min OMCVD-grown AuNPs for 2 min oxygen plasma-treated PS substrates was $\sim 137.2 \pm 16.4$ nm per RIU as shown in Fig. 5.15. Here, the error value is the statistical error due to standard deviation. This FOM is almost 40% higher than the previously reported value of OMCVD grown AuNPs on -NH functionalized glass substrates [94].

5.4.7 Bio Sensing

In the design of a bio-affinity sensor to detect proteins or cancer markers (biomarker found in blood, urine, or body tissues that can be elevated by the presence of one or more types of cancer), the LSPR peaks should be sensitive to the change of the dielectric

environment very close to the surface of the AuNPs. So, the preliminary step is to see whether the sensor is sensitive to the high affinity biotin streptavidin system.

Fig. 5.16 shows the sensor response of the 2 min UV ozone treated and 20 min OMCVD grown AuNPs sample to the biotin-streptavidin system. It shows the variation of the LSPR peaks with streptavidin (SA) concentrations between 10^{-5} to 10^{-1} mg/ml. When obtaining the absorption spectra of the AuNPs while increasing the streptavidin concentrations, the sample containing the AuNPs should not be exposed to air, it should remain in the cuvette which contains the solution. Since the shifts with the concentrations is really small and critical, if the nanoparticles are exposed to air, variation or contamination from the atmosphere will affect the vicinity of the particles and result in false blue shifts. The concentration was varied by removing only half of the SA solution from the cuvette and adding the solution with new concentration, assuring that the sample is still immersed in the solution. Then the combined solution was mixed smoothly with a pipette avoiding air bubbles formation inside the cuvette.

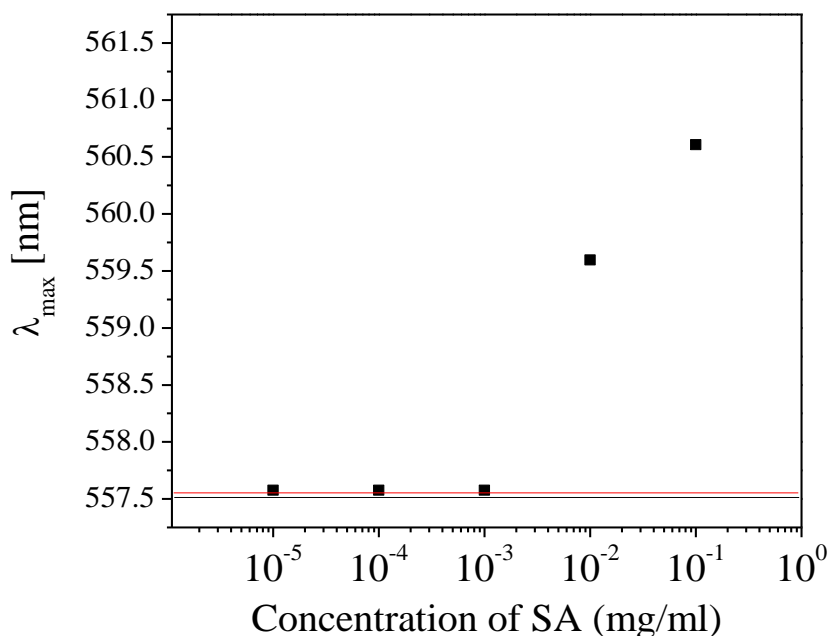


Fig. 5.16 LSPR peak position versus streptavidin concentration on a biotinylated OMCVD AuNP on PS. The black line represents the base line and red line the base line plus three times the detection uncertainty

Fig. 5.16 shows that there was no LSPR shifts observed from the AuNPs for the three lowest SA concentrations tested (10^{-5} , 10^{-4} and 10^{-3} mg/ml). A clear LSPR shift of ~ 2 nm was detected at a streptavidin concentration of 10^{-2} mg/ml (from 557.58 nm to 559.59 nm). A small shift of around 1 nm was observed for the 10-fold SA concentration of 10^{-1} mg/ml, which shows that the sensing signal is moving towards a saturation plateau when the concentration is further increased. Upon binding of molecules to the AuNP surface, the LSPR peak will red-shift by a few nanometers due to an increase in the local refractive index at the AuNPs surface [95]. As the concentration of the SA increases, the surface coverage of SA on the biotin labels on the NPs increases enhancing the overall refractive index leading to the red shift in the LSPR peak. There was a small shift

observed when the sample's immersion solvent was changed from the PBS buffer solution to the initial lowest SA concentration. Afterwards, initial lower concentrations of SA were not adequate to deliver a detectable shift in the LSPR peak position of the AuNPs. This might be because, the concentration of AuNPs grown on PS is smaller than the concentration of AuNPs on glass (due to the lower number of nucleating $-OH$ groups on treated PS surface compared to glass) providing insufficient change in the refractive index of the surrounding of the NPs. But, as the concentration of SA increased further, clear shifts in the peaks were observed. These results demonstrate the ability of the LSPR sensor to detect and quantify SA over a range of 3 orders of magnitude with a limit of detection (LOD) of ~ 10 ng/ml determined by the 3σ method [96].

Although this detection limit is in an acceptable range, it's much lower when compared to some of the currently existing values in literature as given by the following examples. A LOD of 0.42 ng/ml was obtained for the SA binding to biotin, by Barbillon et al., for 100 nm Au cylinders with 50 nm height and 200 nm interspacing fabricated by electron beam lithography [97]. Also a LOD of ~ 0.5 ng/ml was achieved by Karl Schenström using 50 nm AuNPs incubated on three different types of polyelectrolytes (poly(ethylenimine), poly(allylamine hydrochloride) and poly(sodium 4-styrenesulfonate)) functionalized with PEG-biotin, which is almost 20 times larger than our LOD [98]. Even a higher sensitive LSPR biosensor was fabricated by Dong et al., using Au-incorporated nanocomplexes, with silver-nanoparticles as the core material and thin gold-shells (Ag@AuNPs) on a transparent indium tin oxide (ITO) coated glass surface. The strong plasmon and refractive indexes of AgNPs combined with the high chemical stability and low toxicity of AuNPs, conjugated with biotin, was able to quantify various

lower concentrations of SA in a detection range from 1 pM ($\sim 5 \times 10^{-8}$ mg/ml) to 10 nM ($\sim 5 \times 10^{-4}$ mg/ml) with a lower detection limit of $\sim 5 \times 10^{-8}$ mg/ml [99].

Our detection sensitivity is unable to reach the clinical threshold of many protein biomarkers especially in the early stages of the diseases, when their concentrations in clinical samples are generally in the range of fg/ml (10^{-12} mg/ml) to pg/ml (10^{-9} mg/ml) [100]. It is therefore extremely important to develop a sensor with ultrahigh sensitivity. In order to increase the sensitivity of the sensor, we need to build a polymer waveguide carrying AuNPs, which will allow a higher interaction between the probing beam and the sample analyte than the current transmission based sensing which is probed only through a spot size. The details on the fabrication of polymer waveguide with immobilized AuNPs will be discussed in the next chapter.

Chapter 6

6.0 Conclusion and Future Work

6.1 Conclusion

OMCVD is a simple and inexpensive method of fabricating chemically stable, immobilized AuNPs with an acceptable size distribution, delivering a LSPR with an acceptable FWHM of 140 ± 25 nm. It is now possible to reproducibly grow chemically stable AuNPs on oxygen plasma and UV ozone-treated PS. Surface-immobilized AuNPs are not environmentally challenging, since they are covalently bonded to the substrate, allowing for uncomplicated waste management. Sensors made from polymers are easy to handle, less expensive to manufacture, and mass producible. XPS data and the FWHM of the LSPR peaks revealed that the optimum UV-ozone or oxygen plasma treatment time is 2 min. An ethanol-rinsing procedure was necessary to remove loose and unbound AuNPs. The detailed reaction mechanism of Au nucleation onto the polar -OH groups is not within the scope of this work, however Ertorer et al. [42] have assumed a mechanism for polar -NH groups which might be similar to the -OH case. A higher FoM for bulk sensing was achieved in comparison to previously reported values on OMCVD-grown AuNPs on glass. Further bio-sensing experiments with biotin and SA was performed and shifts in the peak wavelengths due to the increase in the SA concentrations were obtained, however only at higher concentrations.

6.2.1 Fabricate Immobilized AuNPs on Alternative Transparent Polymers using OMCVD and Test the Bulk Sensing Ability

In order to see whether AuNPs can be grown on oxygen plasma or UV ozone treated alternative transparent polymers, the proposed procedure is described below. Dissolve the transparent polymers such as Trogamid®, Nylon 6, 10, polyacrylamide etc. with their respective solvents and spin coat over the glass substrates. Find the optimum UV ozone treatment time by systematically varying it to create -OH functionalities with the help of contact angle measurements and XPS analysis. Using this optimum time, follow the same procedure described in chapter 3 to grow AuNPs on these treated polymers using the OMCVD process. Then immerse the AuNP grown sample on different solvents, obtain the peak shifts to find the FoM. Once the AuNPs can be grown on these polymers, the glass substrate should be substituted by PMMA. Then the spin coating should be done over the PMMA substrate, treat the thin film surface by UV ozone and perform OMCVD to grow AuNPs on the polymer. This substitution will be helpful to build an AuNPs carrying polymer channel waveguide for sensing purposes in future.

6.2.2 Fabricate a Polymer Channel Waveguide with the Aid of a Mask

In order to fabricate a polymer channel waveguide, a photo mask should be initially designed, and then the fabrication will be done by photolithography with the aid of this mask. Finally, the fabricated channel waveguide should be characterized to find their thickness, effective refractive indices and optical loss to optimize the waveguide performance [102].

6.2.2.1 Design a Photo Mask

Design a mask onto a quartz glass substrate of size 1 cm x 1cm such that it has patterns of two sets of sizes 10, 20, 50, 100 and 200 μm with interspacing of 0.75 mm as shown in Fig. 6.2. Pair of widths should be chosen, as one for reference and the other for signal channel. Also, the interspacing gap should be chosen so that there will not be any cross-talk between the channels and/or the reference channel. In addition, proper spacing is necessary for alignment purposes. Further, different sizes of widths will have to be chosen, to check the feasibility of confining the channels for end-fire coupling and to provide different size options. The coupling of incoming light into guided modes of waveguide samples (that are end-polished with an optically smooth finish) by transverse excitation using objective lens is known as end-fire coupling [103]. Finally, the mask should be designed by software in the nanofab.

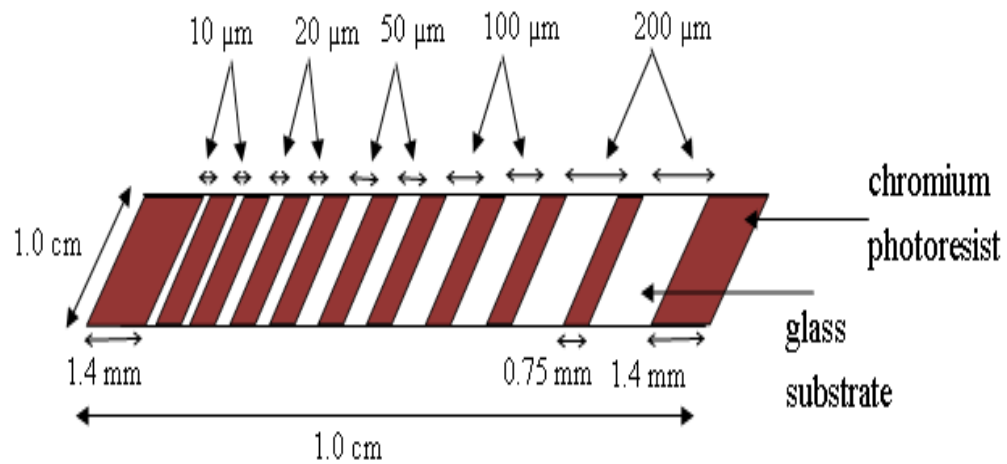


Fig. 6.2 Possible mask design

6.2.2.2 Fabricating a Channel Waveguide using PS and PMMA

Initially the PMMA substrate should be cleaned and the PS should be spin coated over PMMA to deliver a thickness of $\sim 1 \mu\text{m}$. A thickness versus spinning speed plot needs to be created. The sample with the appropriate thickness should be pre-baked at 90°C to remove excess solvent. Align the photo mask (designed in section 6.1.2.1) on top of the spin coated PS film and expose it with UV light (450 W medium pressure Hg lamp) for 20 min [104]. Exposing PS to UV light crosslinks the exposed areas, since PS is a negative resist [105]. Develop using 1-chloropentane as the solvent (doesn't dissolve PMMA) for 90 s which dissolves unexposed areas of PS (crosslinked polystyrene is insoluble to 1-chloropentane) [106]. This procedure is shown in Fig. 6.3. The final structure will provide a channel waveguide with channel widths of 10, 20, 50, 100 or 200 μm with interspacing of $\sim 1 \text{ mm}$ and thickness of $\sim 1 \mu\text{m}$ as shown in Fig. 6.4.

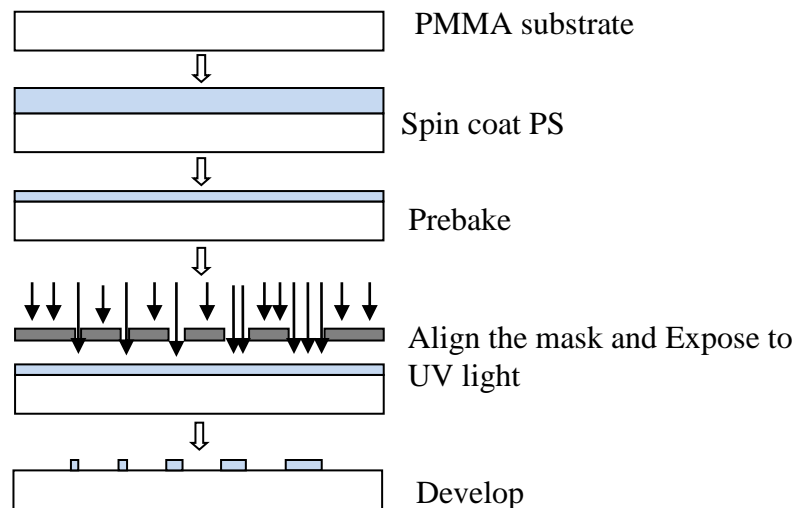


Fig. 6.3 Fabrication of channel waveguide using PS and PMMA

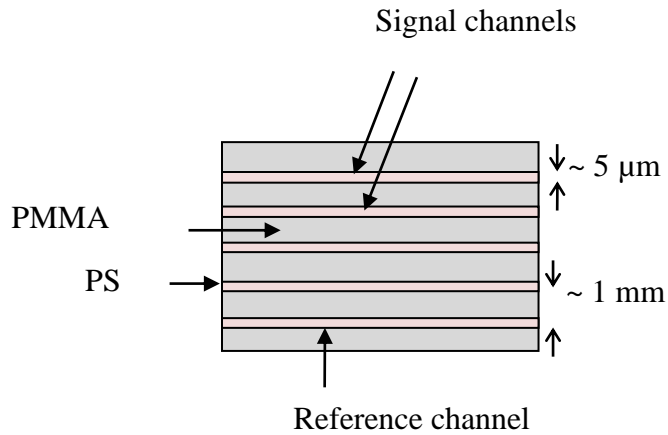


Fig. 6.4 Top view of the fabricated channel waveguide

6.2.3 Characterizing the Fabricated Channel Waveguide

The waveguides need to be characterized with respect to their thickness (t), effective refractive indices (N_{eff}) and the losses. The effective refractive index is one of the most important properties of an optical waveguide. It is needed to calculate waveguide properties like the intensity distribution of the modes themselves. An optical mode in a waveguide is defined as a wave solution to Maxwell's equations with all boundary conditions satisfied, for which the transverse spatial profile of the fields and the polarization remain unchanged during propagation [107]. One can modify the refractive index to minimize losses and to optimize the mode profile.

For the determination of thickness and the effective refractive index of the thin film, a prism coupling technique can be used. In this method, a prism with a very high refractive index should be carefully pressed onto a slab waveguide (before forming the channels) to allow to couple a laser beam into the waveguide by exciting a guided wave through phase matching between the incident wave and guided mode. The entire assembly is then rotated about a vertical axis until a guided mode is launched into the film

as indicated in Fig. 6.5a. Output light should be collected by a photodiode at the end of the waveguide and the mode spectrum (output intensity versus incident angle) should be obtained by turning the waveguide with the prism about a vertical axis with respect to the incoming laser beam. Each sharp peak in the mode spectrum indicates a mode in the slab waveguide (Fig. 6.5b).

The output intensity shows peaks in the case of s-polarization (polarized light whose electric field is normal to the plane of incidence), TE_0 , TE_1 etc. and for the p-polarization (polarized light with its electric field parallel to the plane of incidence), TM_0 , TM_1 etc. The angle positions of these modes are used to calculate the effective refractive indices of each mode and with these the waveguide thickness and the refractive index of the waveguide material can be calculated using the waveguide characterization software. The losses are measured by taking a photo with a digital camera of each propagating mode. The intensity decay along the propagation direction delivers the loss in dB/cm.

The final channel waveguides need to show no intrinsic absorption features. Therefore, light from a white light source should be coupled to the channel waveguide via end-fire coupling into the channel waveguide [108]. At the end, the light should be collected with a second microscope objective and guided with an optical fiber bundle to a monochromator which is operated in the range of 400 – 800 nm. The absorption spectrum obtained from this should not show any absorption peaks within this wavelength range.

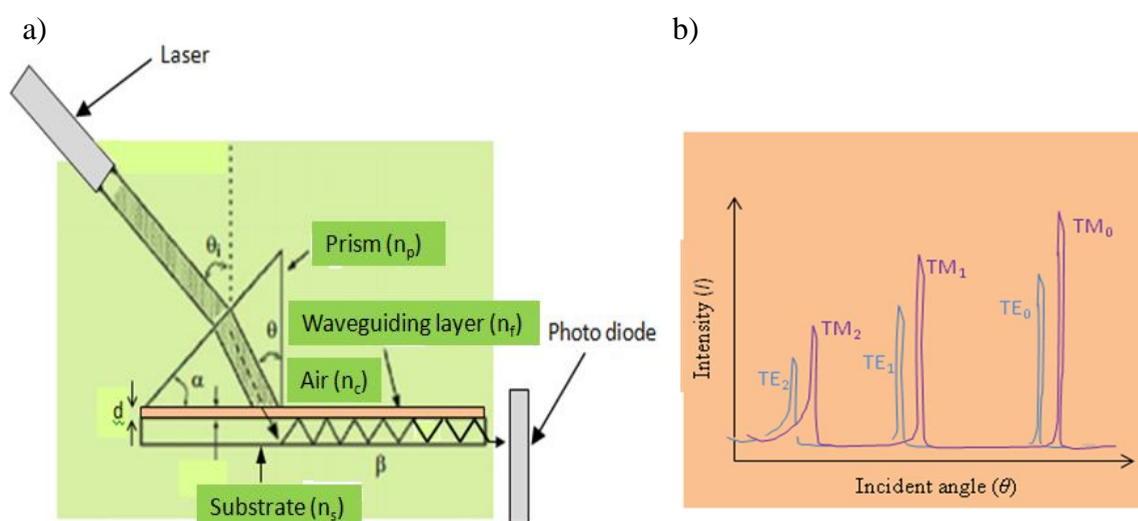


Fig. 6.5 Waveguide characterization setup: a) prism coupling setup b) mode spectrum [109]

6.2.4 Fabricate Immobilized AuNPs on Polymer Channel Waveguides using OMCVD and Test the Bulk Sensing Ability

Grow AuNPs on the channels by using OMCVD. Integrate a transparent flow cell or cuvette to the fabricated sensor to conveniently allow chemical solutions into the sensor as shown in Fig. 6.6. Then immerse the AuNPs in solvents with different refractive indices using the cuvettes, transmit white light through the waveguide and observe the resonance shifts in the absorption spectra from the spectrometer and calculate the FoM.

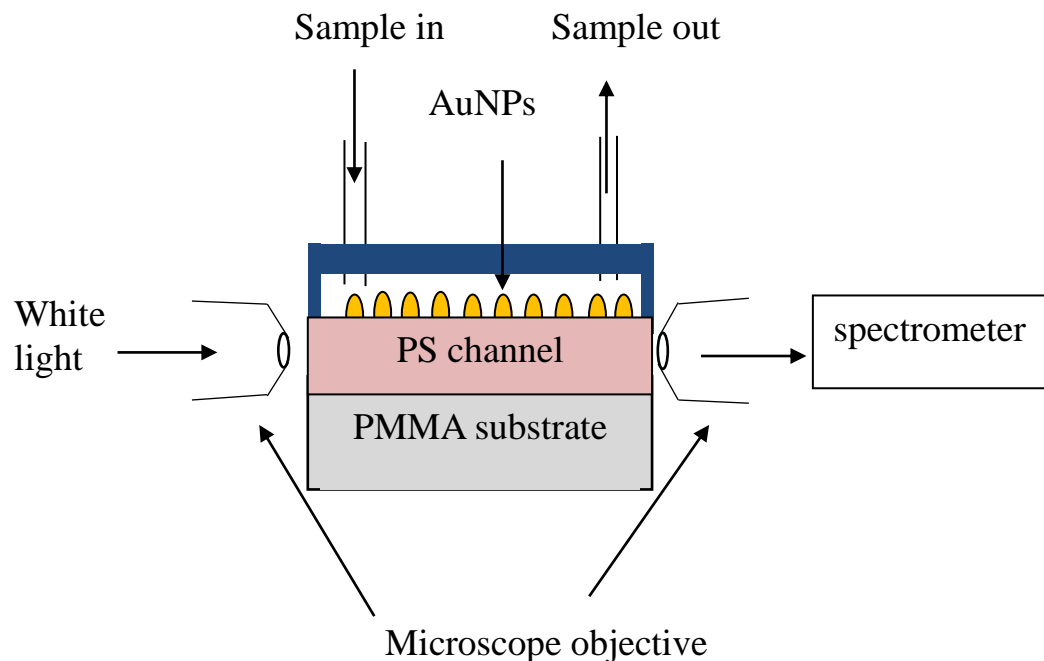


Fig 6.6 Side view of the proposed sensor device

6.2.5 Investigate the Real-Life Biosensing Capabilities using Cancer Surface Marker Protein Epidermal Growth Factor Receptor (EGFR)

Before testing the sensor with the cancer surface marker protein, the bio-sensing ability of the OMCVD grown NPs should be checked by the biotin-streptavidin system using the method mentioned in section 4.5.2. Once the sensor shows the bio-sensing capabilities, it can be used to investigate real-life biosensing capabilities with cancer surface marker protein using the procedure given below.

Initially leave the AuNPs to be immersed in a solution of antibody (anti-EGFR) fragment and PBS buffer for two hours by allowing the solution to pass through the flow cell to the signal channel. Then in order to test nonspecific binding, the reference channel should be immersed in a solution of control antibody fragments for the same duration. Then immerse the channels in PBS buffer and obtain the absorption spectra once the white light is coupled through the waveguide. Finally introduce EGFR antigen (Fig. 6.7) and let them bind for 5 minutes and obtain their absorption spectra [19].

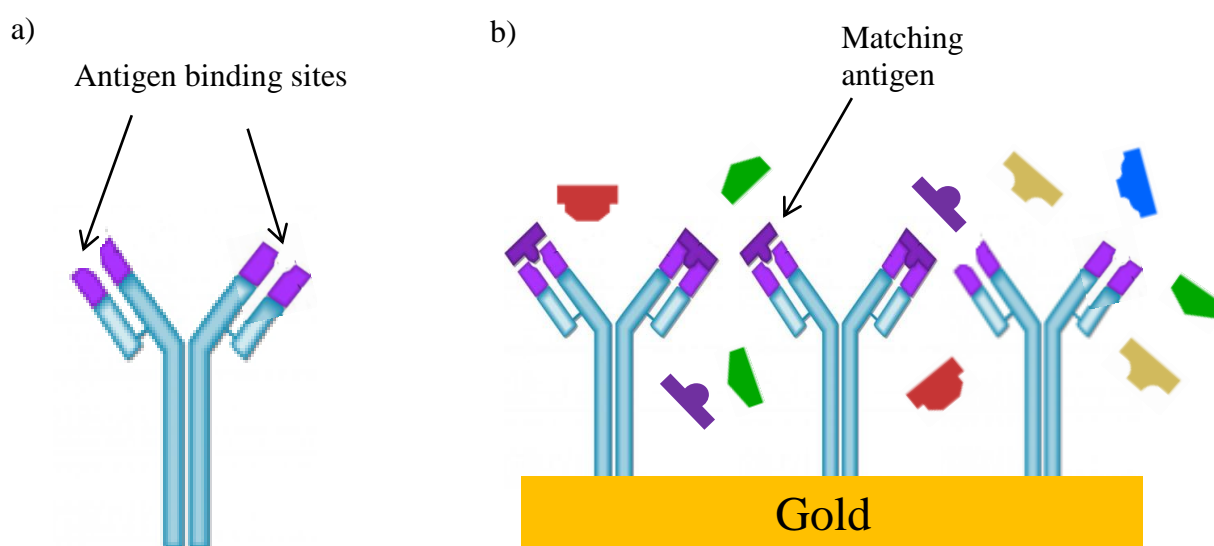


Fig. 6.7 Illustration of antibody fragment and selective recognition of EGFR cancer surface marker (antigen) on its specific antibody, functionalized on gold surface: a) structure of the antibody b) EGFR binding mechanism

Therefore, by fabricating a polymer channel waveguide with AuNPs, a higher interaction between the evanescent fields of the waveguide and the NPs will be obtained due to the increase in the interaction length, compared to the transmission based sensing

done presently, where probing is performed only through a spot size. This will provide more signals and enhance the output intensity and sensitivity, allowing detecting a much lower analyte (sample) concentration. Ertorer et al. were able to get a maximum shift of ~ 2 nm for a concentration of 200 ng/ml of EGFR antigen for the transmission based experiment [19]. When we compare the sensitivities of both sensors, currently the sensing is done only through an area of approximately 9×7 mm² on glass, whereas building a polymer waveguide with a final chip size of 1×1 cm² will increase the sensing area and enhance the sensitivity by almost 100 times. In future, by fabricating a polymer channel waveguide carrying AuNPs and sensing along the entire interaction length, a higher sensitive and cost effective sensor than the currently existing ones can be obtained. Although the results presented in this work are far from conclusive, the advantages of LSPR-based sensors using AuNPs, fabricated on polymer, open the possibilities of further developments in a wide range of medical applications, especially to detect cancer in early stages.

References

- 1) F. Sanchez, K. Sobolev. Nanotechnology in concrete: A review, *Construction and Building Materials*, **2010**, 24, 2060 – 2071.
- 2) J. C. Love, L. A. Estroff, J. K. Kriebel, R. G. Nuzzo, G. M. Whitesides. Self-Assembled Monolayers of Thiolates on Metals as a Form of Nanotechnology, *Chem. Rev.*, **2005**, 105, 1103 - 1169.
- 3) H. Gleiter. Nanostructured materials: basic concepts and microstructure, *Acta mater*, **2000**, 48, 1 - 29.
- 4) A. Turner, I. Karube, G. S. Wilson. *Biosensors: Fundamentals and Applications*, Oxford University Press, **1987**.
- 5) A. Touhami. *Biosensors and Nanobiosensors: Design and Applications*, *Nanomedicine*, **2014**, 374 - 403.
- 6) Y. Hong, Y. Huh, D. S. Yoon, J. Yang. Nanobiosensors Based on Localized Surface Plasmon Resonance for Biomarker Detection, *Journal of Nanomaterials*, **2012**, 2012, 13 pages.
- 7) K. M. Mayer, J. H. Hafner. Localized Surface Plasmon Resonance Sensors; *Chemical Reviews, Plasmonics*, **2011**, 111, 3828 - 3857.
- 8) M. Daniel, D. Astruc. Gold Nanoparticles: Assembly, Supramolecular Chemistry, Quantum-Size-Related Properties, and Applications toward Biology, Catalysis, and Nanotechnology, *Chem. Rev.*, **2004**, 104 (1), 293 – 346.
- 9) A. Rezaee, L. C. Pavelka, S. Mittler. Binary Mixtures of SH- and CH₃-Terminated Self-Assembled Monolayers to Control the Average Spacing Between Aligned Gold Nanoparticles, *Nanoscale Res. Lett.*, **2009**, 4, 1319–1323.

- 10) V. Gedi, Y. Kim. Detection and Characterization of Cancer Cells and Pathogenic Bacteria Using Aptamer-Based Nano-Conjugates, *Sensors*, **2014**, 14, 18302 - 18327, doi:10.3390/s141018302.
- 11) A. K. A. Aliganga, I. Lieberwith, G. Glasser, A. Duwez, Y. Sun, S. Mittler. Fabrication of equally oriented pancake shaped gold nanoparticles by SAM-templated OMCVD and their optical response, *Organic Electronics*, **2007**, 8 (2 – 3), 161–174.
- 12) S. A. LeBlanc. M.Sc thesis: Immobilization of gold nanoparticles for colourimetric detection of biofilms on surfaces, **2015**.
- 13) I. D. Block, L. L. Chan, B. T. Cunningham, “Photonic crystal optical biosensor incorporating structured low-index porous dielectric”, *Sensors and Actuators B*, **2006**, 120, 187–193.
- 14) S. Kandeepan, J. A. Paquette, J. B. Gilroy, S. Mittler. OMCVD Gold Nanoparticles Covalently Attached to Polystyrene for Biosensing Applications, *Chem. Vap. Deposition*, **2015**, 21, 275 – 280.
- 15) H. Becker, U. Heim. Hot embossing as a method for the fabrication of polymer high aspect ratio structures, *Sensors and Actuators A: Physical*, **2000**, 83 (1-3), 130 - 135.
- 16) H. Becker, C. Gartner. Polymer microfabrication methods for microfluidic analytical applications, *Electrophoresis*, **2000**, 21 (1), 12 – 26.
- 17) J. Homola, S.Y. Sinclair, G. Gauglitz. *Sens. Actuators B*, **1999**, 54, 3.
- 18) S. Unser, I. Bruzas, J. He, L. Sagle. Localized Surface Plasmon Resonance Biosensing: Current Challenges and Approaches, *Sensors*, **2015**, 15, 15684 – 15716.

- 19) Ertorer, Erden, "Fabricating Cost-Effective Nanostructures for Biomedical Applications" (2013). *Electronic Thesis and Dissertation Repository*, Paper 1706, <http://ir.lib.uwo.ca/etd/1706>.
- 20) R. K. Darsanaki, A. Azizzadeh, M. Nourbakhsh, G. Raeisi, M. A. Aliabadi. Review Article Biosensors: Functions and Applications, *Journal of Biology and Today's World*, **2013**, 2 (1), 53 - 61.
- 21) P. Rooney, S. Xu, A. Rezaee, T. Manifar, A. Hassanzadeh, G. Podoprygorina, V. Böhmer, C. Rangan, S. Mittler. *Phys. Rev. B*, **2008**, 77, 235446.
- 22) P. John, S. J. Moss, A. Ledwith. In *The Chemistry of the Semiconductor Industry*, Chapman and Hall: New York, **1987**.
- 23) U. Weckenmann et al. *Chem. Mater.*, **2004**, 16, 621.
- 24) M. Brus et al. *J. Chem. Soc., Chem. Commun.*, **1995**, 16, 1655.
- 25) K. A. Willets, R. P. Van Duyne. Localized Surface Plasmon Resonance Spectroscopy and Sensing, *Annu. Rev. Phys. Chem.* **2007**, 58, 267– 297.
- 26) C. Caro, P. M. Castillo, R. Klippstein, D. Pozo, A. P. Zaderenko. Silver Nanoparticles: Sensing and Imaging Applications, *Silver Nanoparticles*, David Pozo Perez (Ed.), InTech, 2010, DOI: 10.5772/8513.
- 27) S. Zeng, K. Yong, I. Roy, X. Dinh, X. Yu, F. Luan. *Plasmonics*, **2011**, 6, 491.
- 28) K. A. Redgrove, R. J. Aitken, B. Nixon. More than a simple lock and key mechanism: unraveling the intricacies of sperm-zona pellucida binding. In: Abdelmohsen K, editor. *Binding Protein*. Rijeka, In. Tech., **2012**, 73 – 122.
- 29) J. G. Ortega-Mendoza, A. Padilla-Vivanco, C. Toxqui-Quitl, P. Zaca-Morán, D. Villegas-Hernández, F. Chávez. Optical Fiber Sensor Based on Localized Surface

- Plasmon Resonance Using Silver Nanoparticles Photo deposited on the Optical Fiber End., *Sensors (Basel, Switzerland)*, **2014**, 14 (10), 18701 - 18710.
- 30) K. Schenström. Biofunctionalization of a Fiber Optics-Based LSPR Sensor, M.Sc thesis, **2015**.
- 31) A. P. F. Turner. Biosensors: sense and sensibility, *Chem. Soc. Rev.*, **2013**, 42, 3184 – 3196.
- 32) J. C. Love, L. A. Estroff, J. K. Kriebel, R. G. Nuzzo, G. M. Whitesides. Self-Assembled Monolayers of Thiolates on Metals as a Form of Nanotechnology. *Chemical Reviews*, **2005**, 105 (4), 1105.
- 33) D. Prashar. Self Assembled Monolayers - A Review, *Int. J. Chem. Tech. Res.*, **2012**, 4 (1), 258 -265.
- 34) A. Ulman. Formation and Structure of Self-Assembled Monolayers, *Chemical Reviews*, **1996**, 96 (4), 1533 – 1554.
- 35) G. M. Whitesides, J. K. Kriebel, B. T. Mayers. Chapter 9: Self-Assembly and Nanostructured Materials, *Nanostructure Science and Technology*, **2005**, 217 - 239.
- 36) C. B. Gorman, Y. He, R. L. Carroll. The Influence of Headgroup on the Structure of Self-Assembled Monolayers As Viewed by Scanning Tunneling Microscopy, *Langmuir*, **2001**, 17, 5324 - 5328.
- 37) D. Trovo, E. Ertorer, R. Huang, T. Cheng, C. Rangan, S. Mittler, in *Modern Aspects of Electrochemistry*, **2013**, 104.
- 38) R. G. Palgrave, I. P. Parkin. *Chem. Mater.* **2007**, 19, 4639.

- 39) J. Wu, W. Shi, N. Chopra. Plasma Oxidation Kinetics of Gold Nanoparticles and Their Encapsulation in Graphene Shells by Chemical Vapor Deposition Growth, *The Journal of Physical Chemistry*, **2012**, 116 (23), 12861 - 12874.
- 40) P. Kiri , M. E. A. Warwick, I. Ridley, R. Binions. Fluorine doped vanadium dioxide thin films for smart windows, *Thin Solid Films*, **2011**, 520, 1363 – 1366.
- 41) E. Ertorer, J. C. Avery, L. C. Pavelka, S. Mittler. Surface-immobilized Gold Nanoparticles by Organometallic CVD on Amine-terminated Glass Surfaces, *Chem. Vap. Deposition*, **2013**, 19, 338.
- 42) M. J. Hampden-smith, T. T. Kodas. *Chem. Vap. Deposition*, **1995**, 1, 8.
- 43) C. Ratscha, J. A. Venables. Nucleation theory and the early stages of thin film growth, *J. Vac. Sci. Technol. A*, **2003**, 21 (5), S96 – S 109.
- 44) A. Aliganga. Fabrication of metal nanoparticles and nanoparticle aggregates onto self-assembled monolayers via organometallic chemical vapour deposition, **2004**, thesis Mainz.
- 45) M. Brust, J. Fink, D. Bethell, D.J. Kiely. *J. Chem. Soc., Chem. Commun.*, **1995**, 1655.
- 46) M. Daniel, D. Astruc. Gold nanoparticles: assembly, supramolecular chemistry, quantum-size-related properties, and applications toward biology, catalysis, and nanotechnology. *Chem Rev.*, **2004**, 104, 293 – 346.
- 47) Y. Hong, Y. Huh, D. S.Yoon, J. Yang. Nanobiosensors Based on Localized Surface Plasmon Resonance for Biomarker Detection, *Journal of Nanomaterials*, **2012**, 1 – 13.
- 48) J. M. Liu, *Photonic devices*. Cambridge: Cambridge University Press, **2005**, 58.

- 49) N. I. Zanoon. The Phenomenon of Total Internal Reflection and Acceleration of Light in Fiber Optics, *International Journal of Computer Applications*, **2014**, 107 (2), 19 – 24.
- 50) G. Oh, D. G. Kim, Y. Choi. The characterization of GH shifts of surface plasmon resonance in a waveguide using the FDTD method, *Opt. Express*, **2009**, 17 (23), 20714 - 20720.
- 51) M. D. Himel, T. C. Kimble. Determination of volume and surface contributions to the total attenuation in ZnS waveguides, *Appl. Opt.*, **1993**, 32, 3306 – 3311.
- 52) R. R. A. Syms, J. R. Cozens. Channel waveguide integrated optics, *Optical Guided Waves and Devices*, **1992**.
- 53) S. Mittler. Gold nanoparticles on waveguides for and toward sensing application, *Springer series on chemical sensors and biosensors*, **2010**.
- 54) M. J. Hampden-Smith, T. T. Kodas. Chemical vapor deposition of metals: Part 1. An overview of CVD processes, *Chem Vapor Deposition*, **1995**, 1 (1), 8 – 23.
- 55) Trogamid T Physical Property Publication Dynamit Nobel Chemicals, **1979**, (technical datasheet).
- 56) D. J. O'Brien, B. E. Parquette. Refractive Index Measurement of Fibers Through Fizeau Interferometry, U.S. Army Research Laboratory, Aberdeen Proving Ground, **2013**.
- 57) J. Stejskal, J. Horská, Refractive index increments of polyacrylamide and comments on the light scattering from its solutions. *Makromol. Chem.*, **1982**, 183, 2527 – 2535. doi: 10.1002/macp.1982.021831022.

- 58) V. I. Silin, G. A. Balchytis, J. J. Kulys. The application of polystyrene waveguides to protein adsorption investigations, *Journal of Biochemical and Biophysical Methods*, **1993**, 26, 71 - 79.
- 59) L. W. McKeen. Chapter 3: Plastics Used in Medical Devices, *Handbook of Polymer Applications in Medicine and Medical Devices*, **2014**, DOI: <http://dx.doi.org/10.1016/B978-0-323-22805-3.00003-7>.
- 60) G. Zhang, L. Wei, M. Wang, K. Zhao. Effects of water concentration in the coating solution on the wall relaxation rate of octadecyltrichlorosilane coated rubidium vapor cells, *Journal of Applied Physics*, **2015**, 117, 043106.
- 61) E. Prats-Alfonso, F. Garcia-Martin, N. Bayo, L. J. Cruz, M. Pla-Roca, J. Samitier, A. Errachidb, F. Albericioa. Facile solid-phase synthesis of biotinylated alkyl thiols, *Tetrahedron*, **2006**, 62, 6876 – 6881.
- 62) C. D. Bain, H. A. Biebuyck, G. M. Whiteside. Comparison of Self-Assembled Monolayers on Gold: adsorption of Thiols and Disulfides, *Langmuir*, **1989**, 5 (3), 723 - 727.
- 63) L. Tang, R. Zhang, X. Zhou, M. Pan, M. Chen, X. Yang, P. Zhou, Z. Chen. *Bio Res.*, **2012**, 7, 3327.
- 64) T. Ohara, Y. Matsumoto, H. Ohashi. The film formation dynamics in spin coating, *Phys. Fluids A*, **1989**, 1 (12), 1849 – 1959.
- 65) S. A. Kandjani, S. Mirershadi, A. Nikniaz. Inorganic–Organic Perovskite Solar Cells, *Solar Cells - New Approaches and Reviews*, Prof. Leonid A. Kosyachenko (Ed.), InTech, **2015**, DOI: 10.5772/58970.
www.intechopen.com/books/solar-cells-new-approaches-and-reviews/inorganic-organic-perovskite-solar-cells.

- 66) D. O. H. Teare, C. Ton-That, R. H. Bradley. Surface characterization and ageing of ultraviolet–ozone-treated polymers using atomic force microscopy and x-ray photoelectron spectroscopy, *Surf. Interface Anal.*, **2000**, 29, 276 – 283.
- 67) A. S. G. Curtis, J. V. Forrester, C. McInnes, F. Lawrie. *J. Cell Biol.*, **1983**, 97, 1500.
- 68) H. Jansen, H. Gardeniers, M. De Boor, M. Elwenspoek, J. Fluitman. A survey on the reactive ion etching of silicon in microtechnology, *J. Micromech. Microeng.*, **1996**, 6, 14 – 28.
- 69) Illustration from TRIZ journal, Article: Dynamization evolution of Dry Etch Tools in Semiconductor Device Fabrication, Dec 02, 2015
- 70) M. R. Davidson, S. A. Mitchell, R. H. Bradley. Surface studies of low molecular weight photolysis products from UV-ozone oxidized polystyrene, *Surface Science*, **2005**, 581, 169 – 177.
- 71) Y. Fu, H. Qui, K. Liao, S. J. Lue, C. Hu, K. Lee, J. Lai. Effect of UV-ozone treatment on poly(dimethylsiloxane) membranes: Surface characterization and gas separation performance, *Langmuir*, **2010**, 26 (6), 4392 - 4399.
- 72) Y. Yuan, T. R. Lee. *Contact Angle and Wetting Properties*, Springer Series in Surface Sciences, **2013**, 51, 3 - 34.
- 73) A. Moldovan, M. Enachescu. *Wetting Properties at Nanometer Scale*, *Wetting and Wettability*, Dr. Mahmood Aliofkhaeaei (Ed.), InTech, **2015**, DOI: 10.5772/60886. Available from: <http://www.intechopen.com/books/wetting-and-wettability/wetting-properties-at-nanometer-scale>.
- 74) T. Manifar, A. Rezaee, M. Sheikhzadeh, S. Mittler. Formation of uniform self-assembly monolayers by choosing the right solvent: OTS on silicon wafer, a case study. *Applied Surface Science*, **2008**, 254, 4611 – 4619.

- 75) M. E. McGovern, K. M. R. Kallury, M. Thompson. Role of Solvent on the Silanization of Glass with Octadecyltrichlorosilane, *Langmuir*, **1994**, 10, 3607 - 3614.
- 76) K. M. R. Kallury, M. Thompson. Interaction of Silicon Surfaces Silanized with Octadecylchlorosilanes with Octadecanoic Acid and Octadecanamine Studied by Ellipsometry, X-ray Photoelectron Spectroscopy, and Reflectance Fourier Transform Infrared Spectroscopy. *Langmuir*, **1992**, 8, 947 - 954.
- 77) A. Rezaee, K. K. H. Wong, T. Manifar, S. Mittler. Octadecyltrichlorosilane (OTS): a resist for OMCVD gold nanoparticle growth. *Surf. Interface Anal.*, **2009**, 41, 615 – 623.
- 78) K. W. Kolasinski, *Foundations of catalysis and nanoscience*, 2nd edition, chapter 2, **2008**, 91 - 103.
- 79) G. Beamson, D. Briggs, *High Resolution XPS of Organic Polymers - The Scienta ESCA300 Database*, Wiley Interscience, **1992**.
- 80) S. Behera, S. Ghanty, F. Ahmad, S. Santra, S. Banerjee. UV-Visible Spectrophotometric Method Development and Validation of Assay of Paracetamol Tablet Formulation, *J. Anal. Bioanal. Techniques*, **2012**, 3(6), 3 - 6.
- 81) D.A. Travo et al. Experimental and Theoretical Issues of Nanoplasmonics in Medicine, *Modern Aspects of Electrochemistry* 56, Springer Science+Business Media New York, **2013**, DOI 10.1007/978-1-4614-6148-7_9.
- 82) J. Spinke, M. Liley, F.J. Schmitt, H.J. Guder, L. Angermaier, W. Knoll. Molecular recognition at self-assembled monolayers: optimization of surface functionalization, *J Chem Phys.*, **1993**, 99 (9), 7012 – 7019.

- 83) M. Alsawafta, S. Badilescu, A. Paneri, V. Truong, M. Packirisamy. Gold-Poly(methyl methacrylate) Nanocomposite Films for Plasmonic Biosensing Applications, *Polymers*, **2011**, 3 (4), 1833 – 1848.
- 84) S. M. H. Rafsanjani, T. Cheng, S. Mittler, C. Rangan. Theoretical proposal for a biosensing approach based on a linear array of immobilized gold nanoparticles, *Applied Physics*, **2010**, 107, 094303.
- 85) S. Link, M. A. El-Sayed. Shape and size dependence of radiative, non-radiative and photothermal properties of gold nanocrystals, *Int. Reviews in Physical Chemistry*, **2000**, 19 (3), 409-453.
- 86) C. P. Burrows, W. L. Barnes. Large spectral extinction due to overlap of dipolar and quadrupolar plasmonic modes of metallic nanoparticles in arrays, *Opt. Express*, **2010**, 18, 3187 - 3198.
- 87) C. Canal, R. Molina, E. Bertran, P. Erra. Wettability ageing and recovery process of plasma-treated polyamide 6, *J. Adhesion Sci. Technol.*, **2004**, 18 (9), 1077 – 1089.
- 88) L. Wegewitz, A. Prowald, J. Meuthen, S. Dahle, O. Hofft, F. Endres, W. Maus-Friedrichs. Plasma chemical and chemical functionalization of polystyrene colloidal crystals, *Phys. Sham. Chem. Phys.*, **2014**, 18261 – 18267.
- 89) Z. A. Lewicka, A. Bahloul, W. W. Yu, V. L. Colvin. A facile fabrication process for polystyrene nanoring arrays, *Nanoscale*, **2013**, 5, 11071 - 11078. DOI: 10.1039/C3NR03345G.
- 90) T. G. Kooten, H. T. Spijker, H. J. Busscher. Plasma-treated polystyrene surfaces: model surfaces for studying cell–biomaterial interactions, *Biomaterials*, **2004**, 25, 1735 – 1747.
- 91) K. A. Akmarov, S. N. Lapshov, A. S. Sherstobitova, A. D. Yas'kov. Optical

- Properties of Aqueous Solutions of Dimethyl Sulfoxide and Application of Refractometry for Monitoring Their Composition, *Journal of Applied Spectroscopy*, **2013**, 80 (4), 610 – 614.
- 92) C. Kim, C. B Su. Measurement of the refractive index of liquids at 1.3 and 1.5 micron using a fibre optic Fresnel ratio meter, *Meas. Sci. Technol.*, **2004**, 15, 1683 – 1686.
- 93) D. B. Pedersen, E. J. S. Duncan, Surface Plasmon Resonance Spectroscopy of Gold Nanoparticle - Coated Substrates, Technical Report DRDC Suffield TR **2005**, 109.
- 94) J. G. Ortega-Mendoza, A. Padilla-Vivanco, C. T. P. Z. D. Villegas- Hernandez, F. Chavez. Optical Fiber Sensor Based on Localized Surface Plasmon Resonance Using Silver Nanoparticles Photo deposited on the Optical Fiber End, *Sensors*, **2014**, 14, 18701.
- 95) J. Z. James, D. Lucas, C. P. Koshland. Gold nanoparticle films as sensitive and reusable elemental mercury sensors, *Environmental science & technology*, **2012**, 46 (17), 9557 - 9562, doi:10.1021/es3005656.
- 96) J. Dostálek, C.J. Huang, W. Knoll. *Surface Design: Applications in Bioscience and Nanotechnology*, Wiley-VCH Verlag GmbH & Co. KGaA, **2009**, 29.
- 97) G. Barbillon, J. Bijeon, J. Plain, M. Chapelle, P. Adam, P. Royer. Biological and chemical gold nanosensors based on localised surface Plasmon resonance, *Gold Bulletin*, **2007**, 40 (3), 240 - 244.
- 98) K. Schenström. M.Sc thesis: Biofunctionalization of a Fiber Optics-Based LSPR Sensor, Department of Physics, Chemistry and Biology, Linköping University, **2015**.

- 99) P. Dong, Y. Lin, J. Deng, J. Di. Ultrathin Gold-Shell Coated Silver Nanoparticles onto a Glass Platform for Improvement of Plasmonic Sensors, *ACS Appl. Mater. Interfaces*, **2013**, 5, 2392 – 2399.
- 100) D. Liu, J. Yang, H-F Wang, et al. Glucose Oxidase-Catalyzed Growth of Gold Nanoparticles Enables Quantitative Detection of Attomolar Cancer Biomarkers. *Analytical Chemistry*. **2014**, 86 (12), 5800 - 5806. doi:10.1021/ac500478g.
- 101) N. Tanio, T. Nakanishi. Physical Aging and Refractive Index of Poly(methyl methacrylate) Glass, *Polymer Journal*, **2006**, 38 (8), 814 – 818.
- 102) F. Chen, X. Wang, K. Wang. Ion-implanted Nd:YVO₄ planar waveguide: refractive-index characterization and propagation mode reduction, *Optics Letters*, **2002**, 27 (13), 1111 – 1113.
- 103) R. R. A. Syms, J. R. Cozens. *Optical Guided Waves and Devices*, Chapter 9: Channel Waveguide Integrated Optics, **1992**.
- 104) D. Knudsen, B. Harnish, R. Toth, M. Yan. Creating Microstructures on Silicon Wafers Using UV-Crosslinked Polystyrene Thin Films, *Polymer Engineering and Science*, **2009**, 945 – 948.
- 105) S. Ma, C. Con, M. Yavuz, B.Cui. Polystyrene negative resist for high-resolution electron beam lithography, *Nanoscale Research Letters*, **2011**, 6, 446.
- 106) D. Ennis, H. Betz, H. Ade. Direct Spin casting of Polystyrene Thin Films onto Poly(methyl methacrylate), *Journal of Polymer Science: Part B: Polymer Physics*, **2006**, 44, 3234 – 3244.
- 107) B. E. A. Saleh, M. C. Teich, *Fundamentals of Photonics*, chapter 8: Fiber Optics, **1991**, 272 – 309.

- 108) H. Gordillo, I. Suárez, R. Abargues, P. Rodríguez-Cant'ó, S. Albert, J. P. Martínez-Pastor, "Review Article: Polymer/QDs Nanocomposites for Waveguiding Applications", *Journal of Nanomaterials*, **2012**, 1 – 9, Article ID 960201.
- 109) X. C. Tong, *Advanced Materials for Integrated Optical Waveguides*, Springer Series in Advanced Microelectronics 46, **2014**, DOI 10.1007/978-3-319-01550-7_2.

Appendices

Appendix A: Copyright Permission for Fig. 3.15

JOHN WILEY AND SONS LICENSE TERMS AND CONDITIONS

Jun 27, 2016

This Agreement between Sivayini Kandeepan ("You") and John Wiley and Sons ("John Wiley and Sons") consists of your license details and the terms and conditions provided by John Wiley and Sons and Copyright Clearance Center.

License Number	3864431069388
License date	May 08, 2016
Licensed Content Publisher	John Wiley and Sons
Licensed Content Publication	Chemical Vapor Deposition
Licensed Content Title	Surface-immobilized Gold Nanoparticles by Organometallic CVD on Amine-terminated Glass Surfaces
Licensed Content Author	Erden Ertorer, Jessica C. Avery, Laura C. Pavelka, Silvia Mittler
Licensed Content Date	Nov 6, 2013
Licensed Content Pages	9
Type of use	Dissertation/Thesis
Requestor type	University/Academic
Format	Electronic
Portion	Figure/table
Number of figures/tables	1
Original Wiley figure/table number(s)	one figure
Will you be translating?	No
Title of your thesis /	Organometallic Chemical Vapour Deposition of Gold

dissertation	Nanoparticles on Polystyrene for Biosensing
Expected completion date	Jul 2016
Expected size (number of pages)	100
Requestor Location	Sivayini Kandeepan 1151 Richmond St London, ON N6A 3K7 Canada Attn: Sivayini Kandeepan
Publisher Tax ID	EU826007151
Billing Type	Invoice
Billing Address	Sivayini Kandeepan 1151 Richmond St London, ON N6A 3K7 Canada Attn: Sivayini Kandeepan
Total	0.00 CAD

Appendix B: Copyright Permission for Chapter 5

JOHN WILEY AND SONS LICENSE TERMS AND CONDITIONS

Jun 27, 2016

This Agreement between Sivayini Kandeepan ("You") and John Wiley and Sons ("John Wiley and Sons") consists of your license details and the terms and conditions provided by John Wiley and Sons and Copyright Clearance Center.

License Number	3878200921958
License date	May 29, 2016
Licensed Content Publisher	John Wiley and Sons
Licensed Content Publication	Chemical Vapor Deposition
Licensed Content Title	OMCVD Gold Nanoparticles Covalently Attached to Polystyrene for Biosensing Applications
Licensed Content Author	Sivayini Kandeepan, Joseph A. Paquette, Joe B. Gilroy, Silvia Mittler
Licensed Content Date	Nov 17, 2015
Licensed Content Pages	6
Type of use	Dissertation/Thesis
Requestor type	Author of this Wiley article
Format	Print and electronic
Portion	Full article
Will you be translating?	No
Title of your thesis / dissertation	Organometallic Chemical Vapour Deposition of Gold Nanoparticles on Polystyrene for Biosensing
Expected completion date	Jul 2016
Expected size (number of pages)	100
Requestor Location	Sivayini Kandeepan 1151 Richmond St

	London, ON N6A 3K7 Canada Attn: Sivayini Kandeepan
Publisher Tax ID	EU826007151
Billing Type	Invoice
Billing Address	Sivayini Kandeepan 1151 Richmond St
	London, ON N6A 3K7 Canada Attn: Sivayini Kandeepan
Total	0.00 CAD

Curriculum Vitae

Name	Sivayini Kandeepan
Post-secondary Education	Postgraduate Institute of Science, University of Peradeniya, Sri Lanka M.Sc. in Nanoscience and Nanotechnology (2010 – 2013) University of Peradeniya, Sri Lanka B.Sc. Special Degree in Physics (2004 – 2008)
Honours and Awards	Lillian Margaret & Walter David Jackson Scholarship in Physics 2014, Department of Physics and Astronomy, University of Western Ontario Western Graduate Research Scholarship (2013 – 2016) University Prize for Academic Excellence 2007/2008, University of Peradeniya
Related Work Experience	Graduate Research Assistant and Teaching Assistant University of Western Ontario (2013 – 2016) Lecturer (Probationary) Dept. of Physics, University of Sri Jayewardenepura (2011 – 2013)
Publications	S. Kandeepan, J. A. Paquette, J. B. Gilroy, S.Mittler, “OMCVD Gold Nanoparticles Covalently Attached to Polystyrene for Biosensing Applications,” Chem. Vap. Deposition, 2015 , 21, 275 – 280.